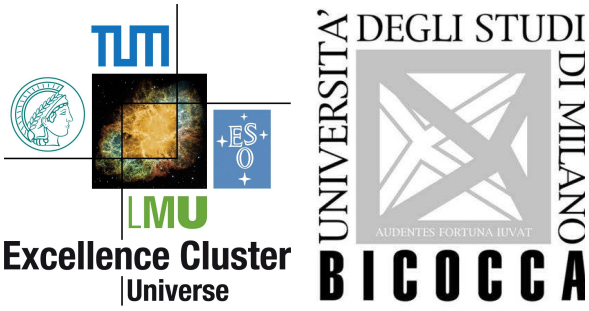

Excellence Cluster Universe

University of Milano-Bicocca

Faculty of Mathematical, Physical and Natural sciences

Department of Physics

Stability studies on triple-GEM detectors

for the GEM upgrade of the ALICE TPC

Master thesis by

Jacopo Margutti

Supervisor: Prof. Luigi Moroni, University of Milano-Bicocca

Assistant supervisor: Prof. Laura Fabbietti, Excellence Cluster Universe

24-Mar-2014

Milan, Italy

Stability studies on triple-GEM detectors for the GEM upgrade of the ALICE TPC

Master thesis by Jacopo Margutti

Supervisor: Prof. Luigi Moroni, University of Milano-Bicocca
Assistant supervisor: Prof. Laura Fabbietti, Excellence Cluster Universe

Summary

The ALICE experiment at CERN is planning a major upgrade of its main central tracking device, the Time Projection Chamber (TPC), for the upcoming RUN 3 at LHC, beyond 2019. The present TPC uses gated Multi-Wire Proportional Chambers (MWPCs) with pad readout to amplify and read out the signal. The gate consist of a grid of wires that collects the ions produced in the amplification process, to prevent them from drifting back in the drift volume, which would eventually lead to deviations of the electrons trajectories and thus to distortions of the reconstructed tracks (*space-charge effect*). The gating grid also blocks the electrons from the ionization tracks, which in turn involves a dead time in the TPC corresponding to the collection time of the ions. Due to their low velocity ($v_{\text{ion}} \sim 10^{-3}\, v_{\text{electron}}$), the maximum read-out rate of the TPC is currently ~ 300 Hz [1] in Pb-Pb collisions, much lower than the maximum collision rate envisaged for RUN 3 (50 kHz).

To fully exploit the capabilities of LHC, it has been planned to substitute the MWPCs with *Gas Electron Multiplier* (GEM) detectors [2], which combine a comparable spatial and momentum resolution with an intrinsic suppression of the back-drifting ions, allowing to operate in a continuous, trigger-less readout mode. A first prototype of a GEM-based TPC Inner Read-Out Chamber (IROC) has been built and commissioned at the Technische Universität München. One of the most problematic requirements associated to the LHC environment, especially in the high-multiplicity scenario of Pb-Pb collisions, is the stability against sparks, that are thought to be triggered by high charge-densities on the GEM-foils.

A dedicated test of the GEM IROC's stability was performed at the Maier-Leibnitz-Laboratorium (MLL) with a beam of low energy, highly-ionizing protons. According to a detailed Geant4 simulation of the experiment, it was possible to reproduce and even overtake the LHC RUN 3 conditions in terms of ionization density across the detector and, conversely, current density flowing across the GEM-foils, which is thought to be the crucial quantity determining sparks. A dedicated read-out was developed to measure sparks in the detector and correlate them to the beam conditions, allowing a precise study of its stability. The results allowed to set safety margins both in detector's gain and particle rate, which indicates that the LHC stability requirements would be satisfied.

Further investigations were carried out around the causes of spark formation in GEM detectors, which are a still not completely understood. A dedicated R&D project was started with a small triple-GEM prototype, to study the effects of different detector parameters on stability. The first one to be studied was the gas choice. The results showed a strong effect of the quenching gases used in the gas mixture: small differences in their amounts can improve the performances of the detector by orders of magnitude. To understand the effects of the gas proprieties on discharges, a Geant4-based Monte Carlo simulation of the experiment was carried out, to compute the primary ionization density expected on the GEM-foils. A new model is proposed to correlate the dependency of the discharge probability on the detector's gain with the primary charge density in the GEM-holes. This allowed to estimate a limit of the absolute primary charge densities sustainable by a triple-GEM detector. The overall agreement with the data suggests that this model could be successfully adopted to estimate the detector's stability also in different scenarios, including the LHC one.

This works investigates as well the influence of the voltage settings of the different GEM-foils on stability. The occurrence of sparks was observed to strongly depend on the order of amplification between GEMs and the transfer fields. To explain these effects, a dedicated Garfield/Magboltz simulation of a GEM detector was developed, focusing on the study of different proprieties of the amplification process as a function of the voltages across the GEMs and the electric fields. Different explanations of the measurements are proposed, based, again, on the assumption that high charge densities in the GEM-holes are responsible for the occurrence of discharges.

Table of Contents

Chapter 1

Introduction

1.1 Quark-gluon plasma

In the standard model of particle physics, quantum chromodynamics (QCD) is the theory that describes the strong force, responsible for the interactions of quarks via massless bosons, the gluons, according to an extra charge, the color, which can have 3 values (and 3 corresponding negative values). QCD explains the binding energy that confines the quarks into composite particles, the hadrons. Hadrons can thus be classified according to the valence quarks of which they are composed: mesons, made of a quark-antiquark pair, and baryons, made of three quarks. The most familiar baryons, protons and neutrons, are again bound together via the strong force in atoms, which make up most of the visible matter of the Universe.

The strong force has a peculiar dependence on the energy scale at which it operates. The strength of the bond between two coupled quarks is, loosely speaking, determined by the coupling constant of the strong force α_s. Renormalization of the quantum field theory introduces a dependence on the energy μ of the process in which α_s is probed:

$$\alpha_s(\mu) = \frac{4\pi}{\beta_0 \log(\mu^2/\Lambda^2_{QCD})} \,, \tag{1.1}$$

where $\beta_0 = 11 - 2N_f/3$, with N_f flavours, and Λ_{QCD}, the QCD scale, is a free parameter of the theory, experimentally determined to be ≈ 200 MeV. The low-energy divergence (below Λ_{QCD}) is responsible for the so-called "color confinement": when pulling two quarks apart, it is energetically more favourable to produce new quark-antiquark pairs instead of free quarks, which have indeed never been observed.

On the other side, there's the so called "asymptotic freedom": α_s becomes asymptotically smaller at high energies and short distances (below the typical hadrons size, ~ 1 fm). Under these conditions, a system of weakly interacting quarks and gluons is thought to be formed: the "quark-gluon plasma" (QGP). Perturbation theory, which - because of the strong color confinement - doesn't hold in standard conditions, can now be applied, allowing precise predictions of key quantities (cross sections, angular distributions, etc.) and thus a solid benchmark for QCD itself. QGP is a unique phase of QCD which is created at very high temperature T and/or baryon chemical potential μ_b, a physical quantity connected to the pressure of the system. Such conditions are

thought to be found in high energy experiments, such as those carried out at heavy-ion colliders (SPS, RHIC, LHC), but also in several astronomical objects such as inner cores of neutron stars [3], or in the Big Bang itself [4]. The study of QGP - its proprieties (temperature, density, speed of sound, transfer coefficients) and evolution (equation of state) - is thus crucial to understand the behaviour of matter in the most extreme conditions that we can found in our Universe.

There is also a more fundamental question which still needs a clear answer: how can we actually describe QGP? The most simple model, an ideal gas of non-interacting quarks and gluons, actually fails at estimating some simple thermodynamic quantities, e.g. the energy density ϵ. According to the Stefan-Boltzmann law, for a system of particles with N_{dof} degrees of freedom:

$$\epsilon_{SB} = \int \frac{d^3p}{(2\pi)^3} \frac{P}{e^{P/T} \pm 1} \approx \frac{\pi^2}{30} \nu N_{dof} T^4 \ , \tag{1.2}$$

where $\nu = 1$ for bosons and 7/8 for fermions. For QGP, according to QCD, the degrees of freedom would be those of free gluons and quarks: $N_{dof} = 2\times(n_c^2-1)+7/8\times4\times n_c\times n_f = 37$. However, the Stefan-Boltzmann limit ϵ_{SB} lays $\sim 20\%$ above the predictions of the latest lattice-QCD calculations in the QGP regime (see fig.1.1).

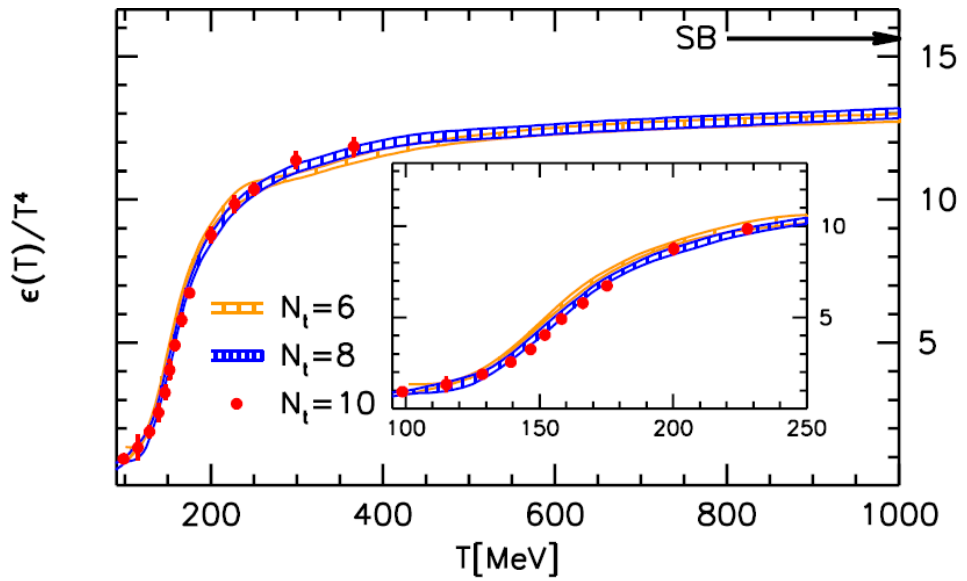

Fig. 1.1: The energy density normalized by T^4 as a function of the temperature on N_t = 6, 8 and 10 lattices. The Stefan-Boltzmann limit is indicated by an arrow [5].

This suggests that the QGP effective degrees of freedom are less than those of free quarks and gluons. The most natural explanation would then be the appearance of complex states or collective behaviours, which both add extra constraints to the system. In both cases, the ideal gas picture would be ruled out. Even if there is neither an analytical

proof of this phenomenon, nor a comprehensive theoretical explanation, experimental evidences arrived at a similar conclusion. What has in fact been discovered at RHIC and, more recently, confirmed by the ALICE experiment [6] is that QGP shows strong collective proprieties, in particular elliptic flow (see sec.1.2), and that it strongly absorbs partons propagating through it. Those phenomena have been consistently described by relativistic hydrodynamical models [7], treating QGP as a quasi-ideal (low viscosity) liquid. This in turn means a strongly-coupled plasma with very short mean free path, the opposite of what the naive picture of the asymptotic freedom would suggest! The origin of this unexpected behaviour is yet to be understood.

In fig.1.2 is shown the predicted phase diagram of quark matter according to the latest theoretical and experimental results. Apart from the color-confined hadron phase and the QGP, a peculiar color-superconducting (CSC) phase is expected at low T and high μ_b (see [8] for a recent review).

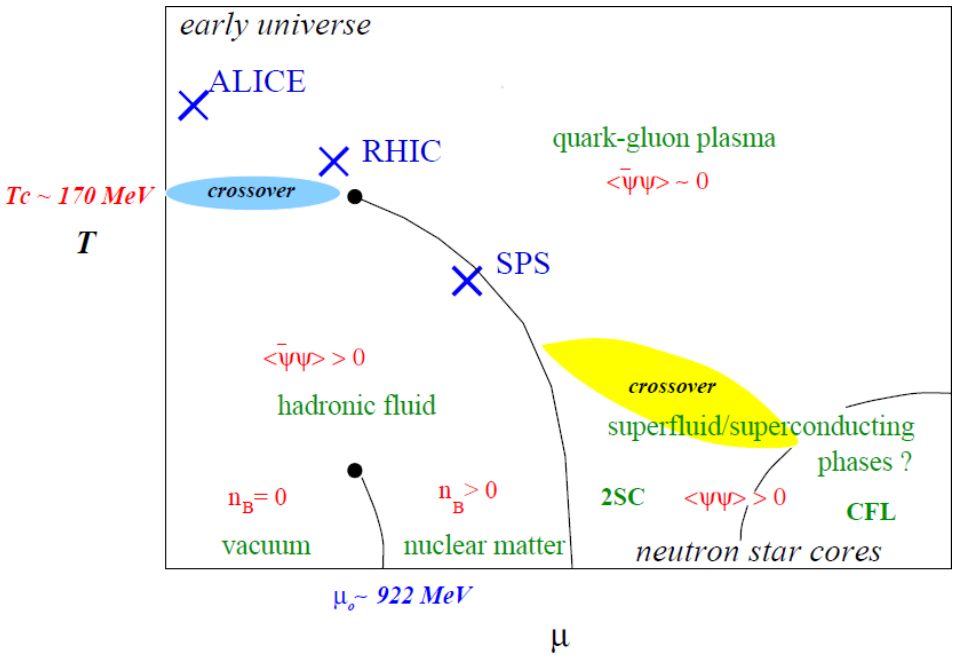

Fig. 1.2: The phase diagram of hot and dense QCD for different values of the baryon chemical potential μ_b and temperature T (adapted from [9]), illustrating the physics reaches of SPS, RHIC and the ALICE experiment at the LHC [10].

The transitions of quark matter between different phases can also shed some light on more fundamental questions connected to the symmetries of QCD, which in turn determine the proprieties of the hadrons. Since the quarks of the first generation (u, d) are relatively light ($m_u \approx 2$ MeV, $m_d \approx 5$ MeV), the QCD Lagrangian [11] shows and approximate *chiral symmetry* [12], which is thought to hold in the QGP phase, at energies $\mu \gg m_{u,d}$, but is spontaneously broken in the vacuum, since the QCD ground state is not invariant under chiral transformations. The corresponding pseudo-Goldstone bosons are

the three pions, charged and neutral, and their masses are connected to chiral symmetry breaking (χSB) through the Gell-Mann-Oakes Renner (GOR) relation:

$$m_\pi^2 f_\pi^2 = -2m_q\langle q\bar{q}\rangle \ , \tag{1.3}$$

the f_π being the pion decay constant and $\langle q\bar{q}\rangle$ the quark-antiquark condensate vacuum expectation value, which can be used as an order parameter for χSB. This explains the difference between the mass of the pion ($m_\pi \approx 140$ MeV) an that of its constituents. Recent lattice-QCD calculations have suggested that χSB can happen at temperatures lower than deconfinement [5] (see fig.1.3), which means that hadrons in a hot and dense medium can exist in a approximately chiral-symmetric state. Their observation (see sect.1.2) would be an unambiguous proof that chiral symmetry is actually restored in the QGP phase.

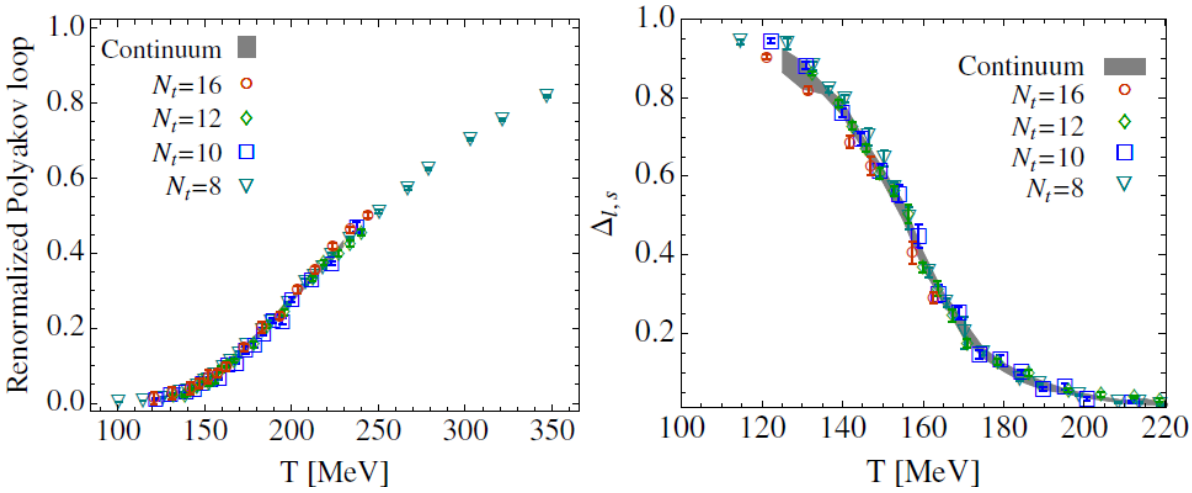

Fig. 1.3: Lattice-QCD calculations of the order parameters of the deconfinement (left) and the chiral (right) phase transitions as a function of temperature [13].

Summarizing, the research on QGP investigates the proprieties of systems of quarks and gluons at very high temperature and/or density, which experiments suggest to be far from trivial. This topic, apart from the study of QCD itself, has huge implications also in astrophysics and nuclear physics. These are some of the most important questions which still need a clear answer:

1. Do the predicted QCD phases at high T/μ_b (QGP, CSC) really occur?
2. Do the known phase transitions (deconfinement, chiral symmetry restoration) really occur? At which T/μ_b? Of which order are they? Is there any critical point?
3. How can we describe QGP? An ideal gas, a fluid or something even different?
4. What are its collective proprieties: temperature, density, degrees of freedom, speed of sound, transfer coefficients? What is then the partonic equation of state (EoS)?

5. What are the in-medium effects on hadrons (i.e. on hadrons produced in QGP)?

1.2 Heavy ion collisions

Heavy ion collisions provide a unique way to study QGP in a controlled way [14]. Differently from p-p collisions, in fact, the system can reach the required spatial extension (above the typical strong interaction range, ~ 1 fm), density ($N_{\text{part}} \gg 1$) and lifetime ($\tau \gg 1$ fm/c) to be described as in thermal equilibrium. With the latest generation colliders, which can accelerate ions above 100 AGeV, it is possible to reach the energy density of the phase transition: $\epsilon > 1$ GeV/fm^3.

After the collision, the system of scattered partons rapidly reaches thermal equilibrium (in ~ 1 fm/c $= 3.3 \cdot 10^{-24}$ s) and then, if T and/or μ_b are sufficiently high, QGP is thought to be formed and then survive for ~ 10 fm/c. As the system expands and cools down, around a critical temperature $T_c \approx 150 - 200$ MeV quarks start to recombine, because of the increasing binding force, and form hadrons; this transition is usually referred to as *chemical freeze-out*. The hadrons are then free to scatter around for some time, until the *kinetic freeze-out*, when they finally leave the interaction region. The overall evolution is schematically summarized in fig.1.4.

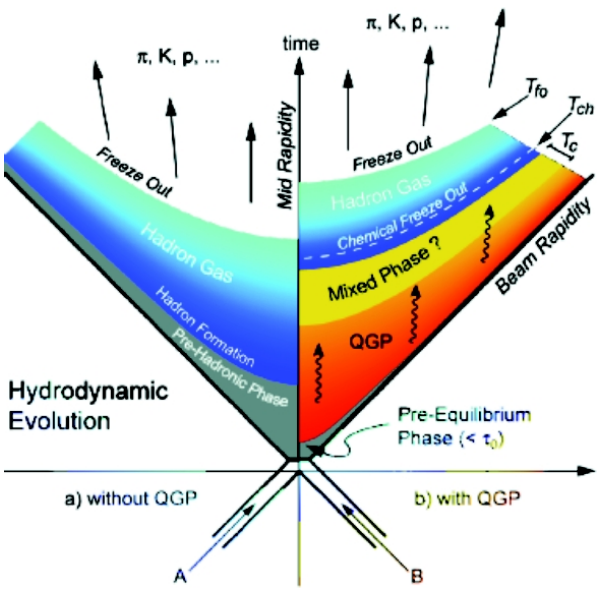

Fig. 1.4: Minkowsky diagram of the system formed in an heavy ion collision, assuming (right) or not (left) the QGP phase [15].

The geometry of a typical heavy ion collision is shown in fig.1.5. The ions initially present a disk-like shape: their width along the direction of motion is contracted, in the lab frame, because of the relativistic velocities.

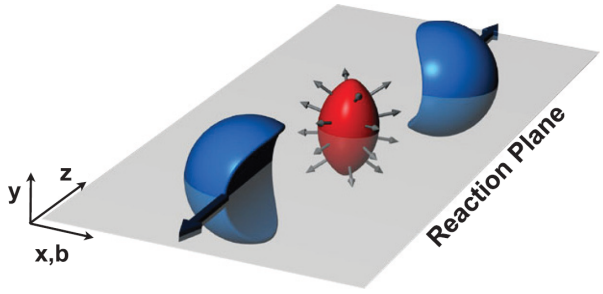

Fig. 1.5: Almond-shaped interaction volume after a non-central collision of two nuclei. The reaction plane is defined by the beam direction (z-axis) and the line connecting the center of the two nuclei, (x-axis) [16].

When they collide, a different portion of the nuclei can overlap, according to the position of the nuclei in the beam-transverse plane. Each collision is thus characterized by a number of participating partons N_{part} (or, equivalently, by an impact parameter b) and a number of binary collisions between each of them N_{coll}.

It is usually impossible to directly measure these quantities; more often, one relies on mean values extracted for classes of events. A convenient way to actually catalogue an ensemble of events, is via the collision centrality, defined as the percentage of non-overlapping area of the nuclei (e.g. 0% is perfect overlap, 100% is a missed collision).

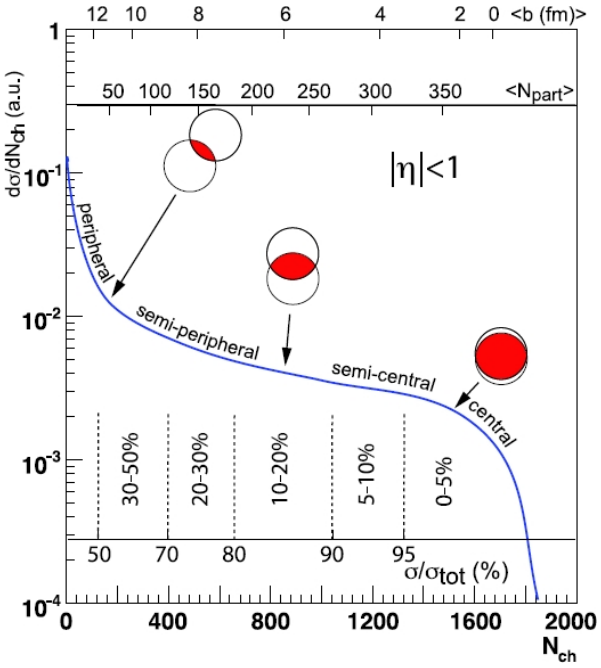

Fig. 1.6: A cartoon example of the correlation of the final state observable N_{ch} with other quantities (b, N_{part}) calculated with Glauber model. The plotted distribution and various values are illustrative and not actual measurements [17].

Centrality is directly extracted from the total charged particle multiplicity $N_{\rm ch}$, assuming that the two are monotonically correlated. In particular, as is shown in fig.1.6, one usually looks at the per-event $N_{\rm ch}$ differential distribution ($dN_{\rm evt}/dN_{\rm ch}$) and bins it in "centrality classes", according to the fraction of the total integral [17]. Mean values of $N_{\rm part}$, $N_{\rm coll}$ and b are then calculated for each class using initial state models (e.g. the Glauber model [18]), which are also dependant on extra inputs (nuclear charge density, inelastic nucleon-nucleon cross section) to be experimentally measured.

Because of the short lifetime of QGP, detectors are sensitive only to final products, after the kinetic freeze-out, i.e. to particles which already underwent all the in-medium effects. First of all, it is thus crucial to identify probes which carry informations about the different phases of evolution of the system, to disentangle the different mechanisms involved.

In this sense, an interesting probe are the hadrons formed by heavy quarks (c, b), usually called "heavy-flavoured". In fact, not only the reference (i.e. in absence of medium) η/p_T spectra can be very precisely calculated with perturbative QCD, but they are also easy to identify in the high-multiplicity environment of a heavy-ion collision, from production until observation [19]. Before hadronization, the large mass of the quarks implies lower probability to be completely thermalized, which allows them to preserve the "memory" of their interaction history; transport proprieties of the medium could thus be inferred from the heavy-flavour particles kinematical distributions [20]. Associated to heavy flavour, the thermal production of charm quarks [21] is also an interesting phenomenon to study.

Other useful probes are the photons and the low-mass dileptons: being insensitive to the strong interactions, they carry the information of their production mechanism unaffected through the whole system evolution. They may serve to extract the temperature of the system, in the different phases, as well as granting information on the EoS itself [22]. Hadrons decaying in dileptons near the transition phase can also help to study eventual signatures of chiral symmetry restoration beyond hadronization, as lattice-QCD calculations suggested (see fig.1.3).

It is also important to define some experimental observables relevant for the study of QGP, which are based on the total yields of the different particles and in their pseudorapidity (η) and transverse momentum (p_T) distributions. To see the effects of the medium, the data is compared with p-p systems, scaling it according to the number of participating nucleons. This is usually done, for each type of particle i produced in a collisions of ions $A-A$, via the nuclear modification factor:

$$R_i^{AA} = \frac{d^2\sigma_i^{AA}/d\eta dp_T}{\langle N_{coll}^{AA}\rangle d^2\sigma_i^{pp}/d\eta dp_T} \ , \tag{1.4}$$

which provides direct signature of an enhancement (suppression) of the selected process, whenever $R^{AA} > 1$ (< 1).

Another subject of study are the collective proprieties of the system, in particular the collective motion, usually referred to as *flow*. The most sensitive observable, being

independent from the interaction plane angle, which is not measurable and randomly distributed in each event, is the the two-particle correlation distribution C as function of the difference in azimuthal angle $\Delta\phi$ and pseudorapidity $\Delta\eta$:

$$C(\Delta\eta, \Delta\phi) = \frac{1}{N_{evt}} \frac{d^2 N_{ass}}{d\Delta\eta, \Delta\phi} = \frac{S(\Delta\eta\Delta\phi)}{B(\Delta\eta\Delta\phi)} \ , \tag{1.5}$$

where $S(\Delta\eta, \Delta\phi)$ refers to particles pairs from the same event and $B(\Delta\eta, \Delta\phi)$ to random combinatorial background and pair-acceptance effects.

Angular/rapidity correlations shows "conventional" events, e.g. jets ($\Delta\eta \approx 0, \Delta\phi \approx 0$) or back-to-back particles ($\Delta\phi \approx \pi$), which can be subtracted using the p-p reference, but also preferred directions of expansion of the system. These anisotropies in the flow would be directly connected to the EoS and the transport proprieties of the system [16]. To quantify them, one usually fits the data expanding $C(\Delta\eta, \Delta\phi)$ on a basis of harmonics:

$$C(\Delta\eta, \Delta\phi) = \frac{1}{N_{trig}} \frac{d^2 N_{ass}}{d\Delta\eta, \Delta\phi} \left[1 + \sum_{n=1}^{+\infty} 2\nu_n cos(n\Delta\phi) \right] \ . \tag{1.6}$$

The fourier coefficients ν_n thus determines the shape of the final particle distribution; according to them, one talks about *radial* flow (ν_0), *elliptic* flow (ν_2), *triangular* flow (ν_3) and so on.

1.3 ALICE

ALICE (A Large Ion Collider Experiment) [10] is a heavy-ion detector at the CERN LHC dedicated to the study of QGP, deconfinement and chiral symmetry restoration. It is also well suited for the study of p-p collisions, which will serve as a reference for heavy ion studies and for specific strong-interaction topics, for which ALICE is complementary to the other LHC detectors. Fig.1.7 shows the details of the detector. It is roughly divided in two main parts: a central barrel, embedded in a large solenoid magnet, to detect hadrons, electrons and photons, and a forward muon spectrometer. From outside to inside, the central barrel consist of two electromagnetic calorimeters (PHOS and EMCal), Transition Radiation (TRD) and Ring Imaging Cherenkov (HMPID) detectors, three arrays of Time-of-Flight (TOF), a cylindrical Time-Projection Chamber (TPC) and the Inner Tracking System (ITS), a six-layer, silicon vertex detector. The TRD, TOF, TPC and ITS cover the full azimuth. The forward muon spectrometer consists of a series of absorbers and tracking/triggering chambers, as well as a large dipole magnet. Other smaller detectors (ZDC, PMD, FMD, T0, V0) for global event characterization and triggering are located in the forward region ($|\eta| \geq 1.7$).

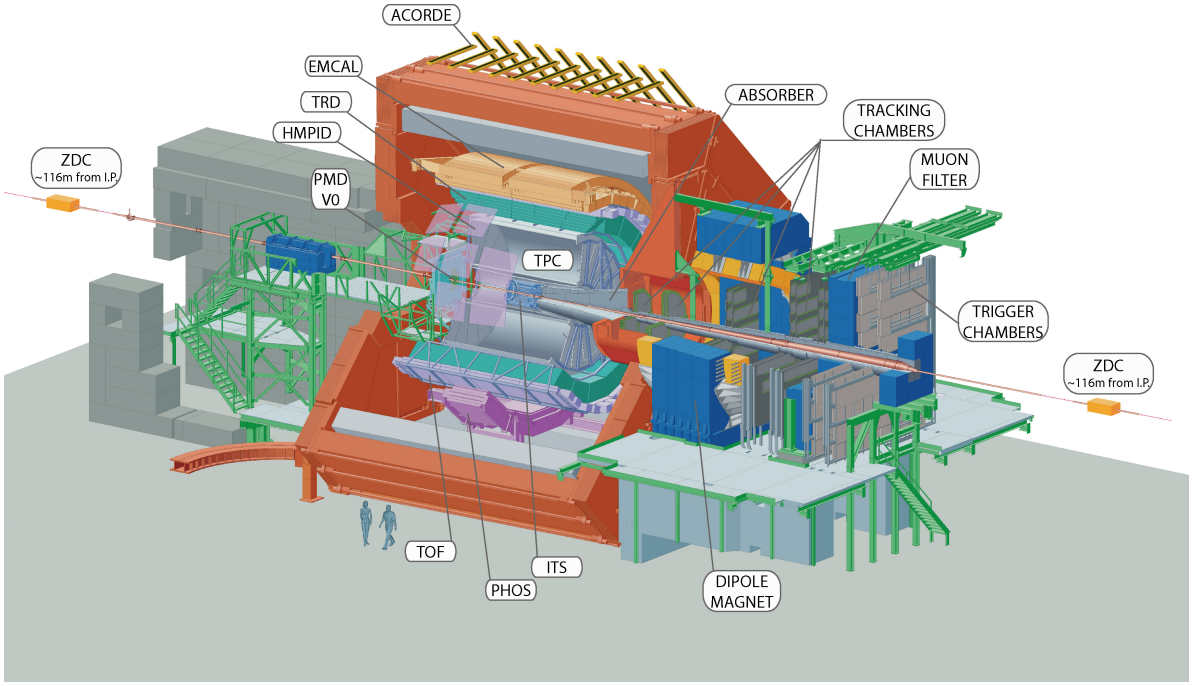

Fig. 1.7: Schematic view of the ALICE detectors [10].

ALICE's objective is to study the proprieties of QGP and, more generally, of QCD in high energy density conditions. In particular, the main areas of physics analysis include:

- In-medium thermalization of heavy quarks, which can be studied by measuring the charm and beauty baryon/meson ratio (Λ_c/D, Λ_b/B) and azimuthal anisotropy ν_2, and the possible in-medium thermal production of charm quarks.
- Heavy quarks energy loss, its mass and color-charge dependence, which can be addressed by measuring the nuclear modification factors R_{AA} of the p_T distributions of D and B mesons separately in a wide momentum range.
- Quarkonia production, in particular charmonium, for which the color screening of QGP (QCD analogous to Debye screening) is thought to involve a net suppression [23].
- Chiral symmetry restoration, studying modifications in the invariant-mass and p_T spectra of light vector mesons (ρ, ω) with dileptonic decay [24].
- Jet quenching, to map out the energy loss of hard scattered ($Q^2 \gg (2\text{GeV/c})^2$) partons, produced before thermalization, and hence reconstruct the evolution and composition of the system.

- Photon-jet correlations for high-p_T photons, to have a direct measurements of the rate of initial hard scattering and thus a control on N_{coll}.
- Thermal photons and low-mass dileptons, to measure the temperature and the collective proprieties of the system.

There are many constraints that such a program puts on the detector performances. Most of the observables in the heavy flavour sector, for examples, being mass or flavour dependant, require particle identification (PID) capabilities: ALICE uses different techniques, such as specific ionization-energy loss (dE/dx), time-of-flight, transition radiation, Čerenkov radiation. For low-mass dileptons, a good momentum resolution down to low-p_T is required: ALICE's dynamic range indeed spans from ≈ 150 MeV/c to above 100 GeV/c. These, together with a relatively low material budget ($\approx 10\%$ of radiation length for normal-incident particles, within ITS and TPC [19]) and good tracking capabilities, are the major strong points of ALICE. The detectors are designed to sustain the great charged particle multiplicity density expected in heavy ion collisions at LHC, i.e. up to $dN/d\eta \approx 8000$ [25]. ALICE's best performances are achieved in a mid-rapidity region ($|y| \leq 0.9$), i.e. where the lowest baryon density and maximum energy density is expected [10].

Chapter 2

Time Projection Chamber

A Time-Projection Chamber (TPC) is a detector which is able to provide 3D information for tracking and momentum measurement together with PID, via specific energy loss dE/dx. Basically, it consists of a chamber filled with gas in which the passage of charged particles leaves a track of electron-ion pairs from the ionization of the gas molecules. An electric field causes the freed electrons to drift towards the anode, where they are amplified and then read out, while the ions drift back towards the cathode. The pick up electrode at the anode is usually sectorized, to preserve the spatial information of the electrons in the plane perpendicular to the drift field. Measuring the arrival time of the electrons, it is possible to reconstruct the ionization points in the chamber and thus the 3D tracks of the incoming particles.

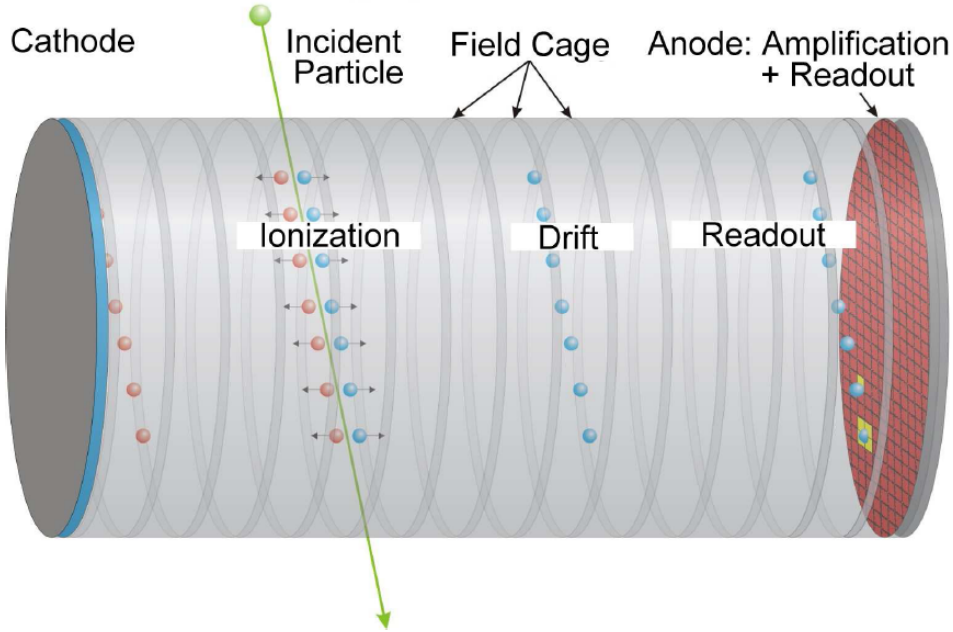

Fig. 2.1: General schematics of a TPC (adapted from [27]).

The electric field inside the drift volume has to be kept as homogeneous as possible: this is usually achieved with a field cage, i.e. conductive strips surrounding the TPC that divide the potential stepwise from the anode to the cathode. Placing a solenoid

around the detector, it is also possible to reconstruct the particle's momentum from the curvature of the tracks, due to the Lorentz force. An excellent reference on the subject can be found in [26]. In fig.2.1 the general schematics of a TPC are shown.

2.1 Ionization

The measured quantity in the TPC is the total number of electrons liberated in the ionization events along the particles tracks. It is possible to effectively describe this process and then correlate it to the physical quantity relevant for PID, the energy loss dE/dx.

Ionization events occur randomly: their number n over a distance x follows a Poisson distribution:

$$P(n) = \frac{(x/\lambda)^n}{n!}\, e^{-x/\lambda} \,, \tag{2.1}$$

where the mean free path λ can be computed from the electron density of the gas n_e and the ionization cross-section σ_I, $\lambda = 1/(n_e\sigma_I)$. Most of the collisions result only in one freed electron, but the total charge along a track comes also from *secondary* ionization, either by a primary electron which ionizes, or by de-excitation of the gas molecules, or again by interactions of their metastable states. For example, given two gas components A, B, of which one is in the excited state A^*, the following reaction can occur:

$$A^* + B \rightarrow A + B^+ + e^- \,. \tag{2.2}$$

Usually in a TPC mixture, A is a noble gas (e.g. Ar, Ne) and B is an additive required for stability in the amplification stage (see sec.2.5). This reaction goes under the name of *Penning effect* [28].

Secondary ionization from primary electrons depends on their energy; it is thus necessary to know their energy spectrum $F(E)$, or, equivalently, the corresponding differential cross section $d\sigma/dE$ of ionization:

$$F(E) = \frac{n_e\,(d\sigma/dE)}{\int n_e\,(d\sigma/dE)\,dE} \,, \tag{2.3}$$

where n_e is the electron density of the gas. One can also correlate it to the energy loss:

$$\frac{dE}{dx} = \int n_e\, E\, \frac{d\sigma}{dE}\, dE \,. \tag{2.4}$$

The most used model to compute $d\sigma/dE$ is the photo-absorption ionization model (PAI) [29], which assumes that ionization occurs via the exchange of virtual photons (i.e. photoelectric effect), and thus links it to the well measured photon-absorption cross section $\sigma_\gamma(\omega)$:

$$\sigma_\gamma(\omega) \approx \frac{Z}{n_e}\,\frac{\omega}{c}\,\epsilon_2(\omega) \,, \tag{2.5}$$

where ϵ_2 is the complex part of the dielectric constant $\epsilon = \epsilon_1 + i\epsilon_2$. The PAI differential cross section thus reads:

$$\frac{d\sigma}{dE} = \frac{\omega\epsilon_2}{c\beta^2\pi}\left[\frac{\sigma_\gamma(E)}{EZ}\log\frac{2mc^2\beta^2}{E[(1-\beta^2\epsilon_1)^2+\beta^4\epsilon_2^2]^{1/2}} + \frac{Z}{n\hbar c}\left(\beta^2 - \frac{\epsilon_1}{|\epsilon|^2}\right)\theta + \frac{1}{ZE^2}\int_0^E \sigma_\gamma(E')\,dE'\right] . \tag{2.6}$$

For energies above the highest atomic binding energy ($E_k \approx 100$ eV), $d\sigma/dE$ converges to the Rutherford formula for scattering on one electron:

$$\frac{d\sigma}{dE} \xrightarrow{E\gg E_k} \frac{2\,\pi\,r_e^2}{\beta^2}\,\frac{m\,c^2}{E^2}\ , \tag{2.7}$$

where $r_e = e^2/mc^2$ is the classical electron radius. The $1/E^2$ dependency translates into a long high energy tail of the primary electrons energy distribution $F(E)$. High energy electrons significantly contribute to the mean number of electrons per unit length $\langle dn/dx\rangle$, resulting in $\langle dn/dx\rangle \gg 1/\lambda$, as they deposit their energy mostly within a short distance (≈ 1 mm for a 10 keV electron in argon S.T.P. [26]), thus creating *clusters* of electrons along the track. From $F(E)$ it is possible to compute the so-called *cluster-size distribution* $P(n)$, i.e. the probability to liberate n electrons with each primary ionization event.

The experimental observable are not, however, the electron clusters, but the number of electrons integrated over a certain track length, correspondent to the granularity of the read-out plane. Since the ionization events follow a Poisson distribution, and with the knowledge of $P(n)$, it is possible to compute the *ionization distribution* $G(n,x)$, i.e. the probability to find n electrons over a distance x along the track, which actually describes the signal pulse height distribution (see fig.2.2).

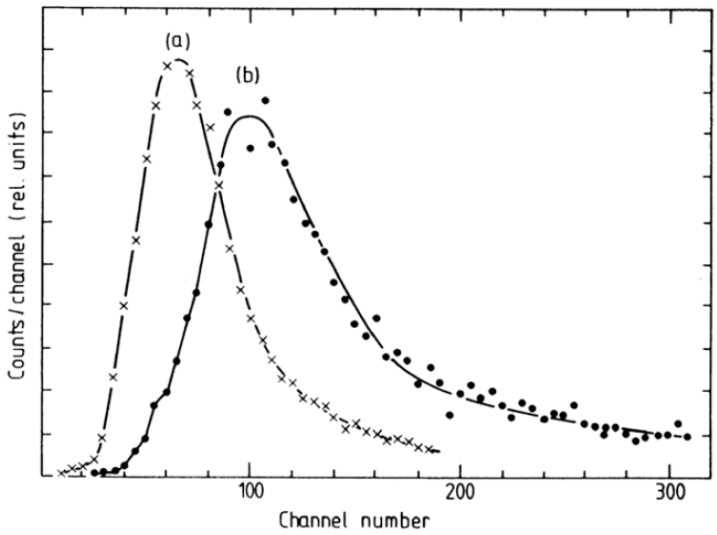

Fig. 2.2: Measured pulse height distribution for a 2.3 cm sample in Ar/CH4 at 1 atm: (a) 3 GeV/c protons, (b) 2 GeV/c electrons [30].

Ionization is not the only energy loss mechanism; excitation of the gas molecules, for example, contributes in a similar amount, without freeing charge. To correlate energy loss and ionization, it is thus necessary to define an *effective ionization potential* W, i.e. the energy that is spent, on the average, to produce one electron/ion pair. The average energy loss over a distance Δx is thus:

$$\left\langle \frac{\Delta E}{\Delta x} \right\rangle = W \frac{\langle G(\Delta x) \rangle}{\Delta x} \ . \tag{2.8}$$

2.2 Drift and diffusion

Electrons from ionization moves towards the anode, being accelerated by the drift field E_d. Along the way, they undergo collisions with the gas molecules and they get scattered in random directions. Because of their small mass, electrons loose any preferred direction of motion after each collision - their instantaneous velocity v_i is thus randomly oriented - but then they are immediately accelerated towards the drift direction. The average drift velocity v_d ($\ll v_\mathrm{i}$), neglecting the influence of the magnetic field B, is thus given by the acceleration and the average time between collisions τ:

$$v_\mathrm{d} = \frac{e\,E_\mathrm{d}}{m}\,\tau = \mu\,E_\mathrm{d} \ . \tag{2.9}$$

The mobility (μ) is another quantity often used to characterize the movement of electrons (and ions) in gases. It is defined as the ratio of drift velocity to applied electric field: $\mu = v_\mathrm{d}/E_\mathrm{d}$.

Because of the collisions, a point-like cluster of electrons would be spread, after a time t, according to a Gaussian distribution of width $\sigma^2 = 2Dt$. The diffusion coefficient D depends on the gas proprieties and the electric and magnetic fields. In a simplified model [26], it can be expressed as:

$$D = \frac{2\,\epsilon\,\tau}{3\,m} \ , \tag{2.10}$$

where τ is the mean time between collisions and ϵ, m the energy and mass of the electrons. The width of the spread σ after a lenght L can thus be expressed as:

$$\sigma^2 = \frac{4\,\epsilon\,L}{3\,e\,E_d} \ . \tag{2.11}$$

Typically, diffusion limits the space resolution achievable in the track reconstruction and is thus to be reduced. The minimum is reached for minimum electron energies, i.e. at thermal equilibrium with the medium ($\epsilon = \epsilon_\mathrm{T} = (3/2)kT$). In the so-called *hot gases* (e.g. argon) the electron energies are usually higher ($\epsilon \gg \epsilon_\mathrm{T}$), and thus higher fields are required to minimize diffusion. *Cold gases* (e.g. CO_2) correspond to the opposite case

($\epsilon \ll \epsilon_{\rm T}$). To compute the electron spread directly from the drift length L, for fixed gas and fields, the diffusion coefficient is usually redefined as:

$$D \equiv \sqrt{\frac{2\,D}{v_{\rm d}}} \quad \rightarrow \quad \sigma = D\,\sqrt{L}\,. \tag{2.12}$$

Electrons also feel the influence of the surrounding charge, since they usually move in clusters. The collision rate ($1/\tau$) is different whether the electron is inside or at the edge of the charge cloud [31]; this leads to a spatial anisotropy in the diffusion, and it is necessary to define a transverse $D_{\rm T}$ and longitudinal $D_{\rm L}$ diffusion coefficient. Considering a magnetic field B parallel to $E_{\rm d}$, the transverse diffusion is reduced by the curling of the electrons in the $x-y$ plane:

$$\frac{D_{\rm T}(B)}{D_{\rm T}(0)} \approx \frac{1}{1+\omega^2\,\tau^2}\,, \tag{2.13}$$

where $\omega = (e/m)B$. The longitudinal diffusion, on the contrary is unaffected. This contribution can be rather important for TPCs (see fig.2.3).

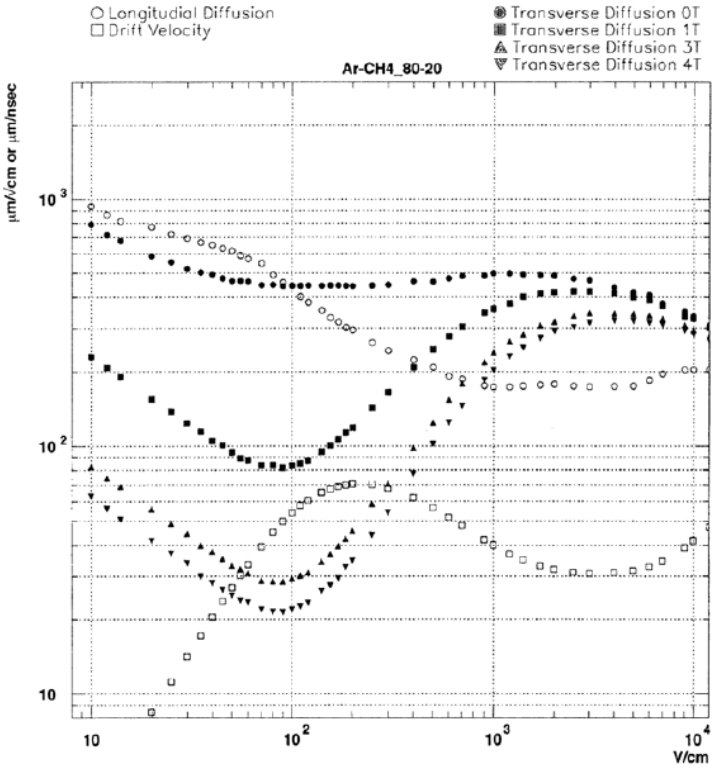

Fig. 2.3: Computed transverse and longitudinal diffusion constants for electrons in Ar/CH4 (80/20), in μm/cm$^{1/2}$, as a function of electric and magnetic fields. Drift velocity in μm/ns [31].

.

Along their drift, electrons can be absorbed in the gas by the formation of negative ions. This process is called *attachment*. The noble gases typically used in TPCs have small electron affinities and do not capture electrons. Impurities (i.e. O_2, H_20), on the contrary, can significantly contribute to attachment even in small amounts ($\sim$10 ppm). The rate of attachment R is given by the absorption cross section σ of the impurity, its density n and the electron average velocity $\langle v_i \rangle$:

$$R = \sigma \, n \, \langle v_i \rangle \ . \tag{2.14}$$

2.3 Amplification

In most of the TPCs built so far the amplification of the primary electrons is performed with a grid of wires at positive potential, which constitute the anode. Detectors with such an amplification scheme are called Multi-Wire Proportional Chambers (MWPCs). The wires are sufficiently thin ($\sim 10\ \mu$m) to generate a high electric field (~ 200 kV/cm) around them, which accelerates the primary electrons up to induce secondary ionization; these electrons, in turn, are accelerated and end up ionizing the gas. The result is a chain reaction that produces an avalanche of electrons. Their number n along a distance x growths exponentially:

$$n \approx n_0 \, e^{\alpha x} \ , \tag{2.15}$$

where α is the first Townsend coefficient; it usually depends on the applied electric field E and the gas density ρ. Assuming the latter to be constant, the average amplification $\langle A \rangle = n/n_0$ is:

$$\langle A \rangle = \exp \left(\int \frac{\alpha(E)}{dE/dx} \, dE \right) \ . \tag{2.16}$$

Since the multiplication is a stochastic process, the number of electrons produced will vary from avalanche to avalanche; it has been found [32] that a good approximation of the amplification probability $P(A)$ in proportional counters is given by the *Polya distribution*:

$$P(A) = \frac{m^m}{\Gamma(m)} \left(\frac{A}{\langle A \rangle} \right)^{m-1} e^{-m(A/\langle A \rangle)} \ , \tag{2.17}$$

where the parameter m depends on the voltage settings and the gas used, and is thus to be fixed experimentally. Fluctuations in the amplification (also called *gain*) are also caused by different parameters, that one has to take into account in practical applications:

- geometrical imperfections or mechanical defects in the chamber components (cathode, wires, anode),
- edge effects, i.e. smaller fields on the edges of the drift volume,
- pressure and temperature variations, which influence the gas density.

During the amplification process, positive ions of the gas atoms are freed along the electron avalanche. Due to their low mobility ($\mu \approx 1$ cm^2/Vs), they usually take long to drift back to the cathode and get collected. In case of a continuous flow of particles, at rates higher than the ion collection time, they will accumulate in the drift volume, building up clouds of positive charge which unavoidably deviates the electrons from the drift direction, resulting in distortions of the reconstructed tracks. The overall effect of the accumulated ions is usually referred to as *space charge effect*.

In MWPC-TPCs, this is usually avoided introducing a gating mechanism, i.e. another grid of wires placed in front of the amplification stage which collects the back-drifting ions and prevents more electrons from getting amplified. The wires can be set at the same potential (*monopolar* gating grid), all the field lines ending up in them, or at alternating potential of $V_g \pm \Delta V$ (*bipolar* gating grid) [31]. The gating grid is switched on and off alternatively, according to a trigger; the maximum rate is limited by the collection time of the ions. Because of the high voltage, the gating grid must be placed a few mm from the amplification region, which means $\sim$100 μs ion collection time and, conversely, $\sim$1 kHz maximum rate.

MWPC-TPCs usually use extra grids of wires to correct the electric field. The *shielding wires* straighten the field at the transition between the amplification and the drift region, while the *field wires* reduce the cross-talk between adjacent anode wires. The general configuration of a MWPC with the gating mechanism is shown in fig.2.4.

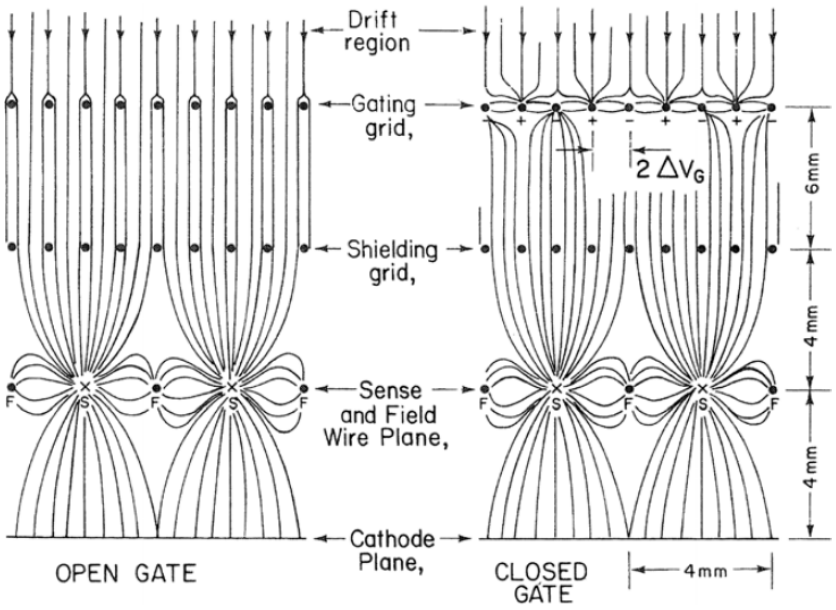

Fig. 2.4: Schematics of the field lines for an open and closed gating grid [33].

2.4 Signal formation

The signal consists of the currents induced on the electrodes surrounding the amplification region, like the anode wires. Usually the readout includes a planar electrode, properly divided in pads (*pad plane*), to preserve the spatial information of the arriving electrons. The current I_R induced by the moving charges around the wire is given by:

$$I_R = -\frac{q}{V_w}\mathbf{E_w} \cdot \mathbf{v} \ , \tag{2.18}$$

where E_w (*weighting field*) is a conceptual field, assuming that the charge q is removed, the read-out electrode is set to voltage V_w, and all other surrounding electrodes are grounded [34]. The electrons, being collected within $\sim$ 1 ns, make up only a small fraction ($\sim$ 6%) of the total induced signal, the rest coming from the movement of the ions. However, the time ions take to drift back to the cathode ($>$ 100 μs) is usually much bigger than the typical signal time width required to avoid pile-up. Part of their contribution is usually cut-off in the electronic pulse shaping.

2.5 Discharges

The amplification process also results in the excitation of many gas atoms, which can subsequently lose their energy emitting photons in the visible and UV range. These photons may in turn ionize the gas atoms or extract electrons from the surrounding electrodes (photoelectric effect), resulting in creation of even more charge. This effect, usually called *photon feedback*, degrades the energy resolution and could develop full avalanches separated from the primary one. If the fields are strong enough, the process can be self-sustaining, thus resulting in a complete electric breakdown. To prevent the problem, the noble gas is usually mixed with a smaller fraction of *quenching gas*, which usually consist of an organic, polyatomic gas (CO_2, CH_4) with large photon absorption cross section in the visible and UV range, because of the multiple rotational and vibrational excitation levels of the molecules, see fig.2.5.

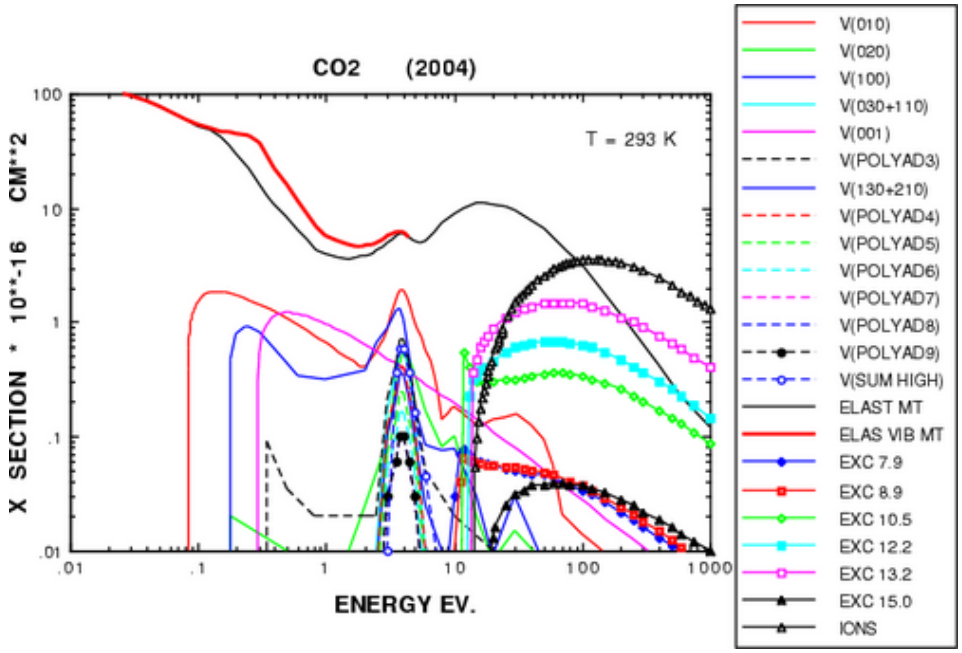

Fig. 2.5: CO_2 photo-absorption cross section, with the contributions of different processes [67].

However, there other mechanisms involved in the creation of discharges. According to experiments made with parallel plate capacitors, when the concentrations of electrons in an avalanche exceed a certain number ($\sim 10^8$) - the so-called *Raether limit* [35] - the space charge produced is strong enough to locally intensify the electric fields and thus give rise to a forward-backward propagating avalanche, a *streamer*, whose total charge is almost independent from the primary one [36]. In case of MWPCs, the streamer propagates only a few mm from the anode wires, as the electric field rapidly drops, and do not lead to a full electrical breakdown [26].

Chapter 3

GEM upgrade of the ALICE TPC

3.1 ALICE TPC: status and perspectives

The TPC is the main charged particle ID and tracking device of ALICE. It consists of a cylindrical barrel with a field cage, which constitute the drift volume, two readout electrodes on the sides and one central cathode, that provides the drift field. The TPC spans over -250 cm $< z <$ 250 cm, with an inner radius of 87 cm and an outer radius of 247 cm, covering full 2π azimuthal angle and a range $|\eta| < 0.9$ of pseudo-rapidity. It covers a large p_T range, from 0.1 GeV/c up to 100 GeV/c, with good momentum resolution. The TPC was designed to sustain the extreme charged particle multiplicity densities expected at LHC, up to ~ 8000 $\mathrm{d}N_{\mathrm{ch}}/\mathrm{d}\eta$. The readout electrodes are divided into 18 trapezoidal sectors, each covering 20° azimuthal angle. Each sector is then divided along radial direction in an Inner and Outer Readout Chamber (IROC and OROC, respectively), see fig.3.1.

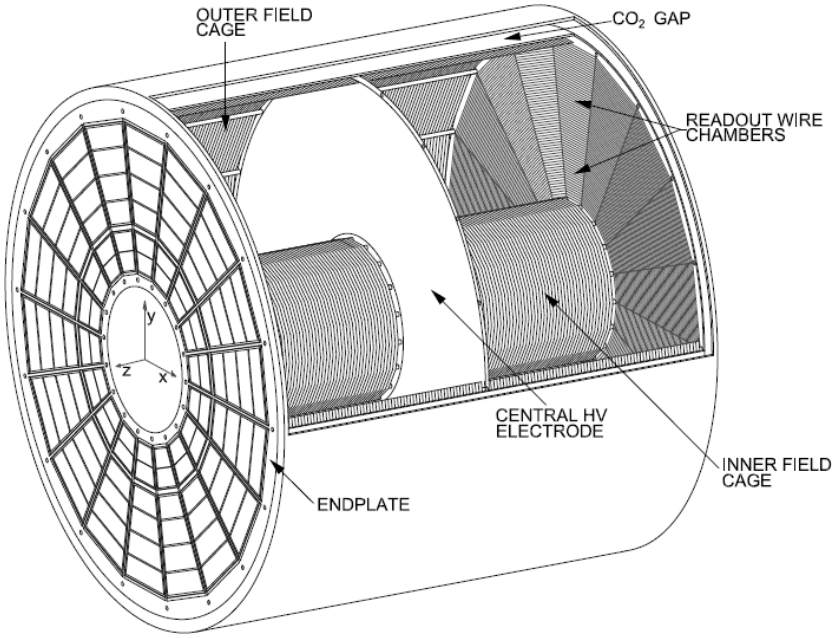

Fig. 3.1: Schematic view of the ALICE TPC [37].

The chambers currently employ MPWC technology with gating grid. The read-out planes are divided in pads of different sizes, depending on the radial position: 4×7.5 mm^2 (IROC), 6×10 mm^2 and $6\times$ 15 mm^2 (OROC) in $r\phi \times r$, for a total of 557,568 readout channels. The gas used in the TPC is Ne/CO_2 (90/10), chosen for its low multiple scattering and diffusion ($D_T \approx D_L \approx 220\ \mu m/\sqrt{cm}$) proprieties. A detailed description can be found in [1].

The gating grid, used to reduce the back-drifting of ions (see sec.2.3), sets some strict limits on the TPC read-out rate. In Ne/CO_2 (90/10), the collection of ions from the anode wires takes $\sim 180\ \mu$s; with other $\sim 100\ \mu$s imposed to avoid event pile-up, an overall intrinsic dead time of $\sim 300\ \mu$s limits the TPC to a maximum operating rate of ~ 3.5 kHz in p-p collisions. For Pb-Pb collisions, because of the higher multiplicities, the constraints are even more severe, down to ~ 300 Hz. Operating without the gating grid would be impossible, since the ions can take up to 156 ms to cover the full drift length (2.5 m), resulting in unbearable space-charge effects in the drift volume. It should be noted, however, that also the readout system currently imposes limits on the rate, i.e. ~ 500 Hz for central Pb-Pb collisions.

Up to now, the detector has operated with Pb-Pb collisions at $\sqrt{s_{NN}} = 2.76$ TeV (2010-2011), with an integrated luminosity $\mathcal{L}_{int}$ of 0.16 nb^{-1} [37]. After the first LHC long shut-down (LS1), for RUN 2 (2015) a major upgrade of the luminosity, up to $\mathcal{L}_{int} = 1$ nb^{-1}, is expected, which translates into 5 kHz minimum bias Pb-Pb collision rate over the beam-time. Because of the current limitations, only $\sim 1/10$ of the events will be recorded. For RUN 3 (2019) the LHC will be further upgraded, up to luminosities of $\mathcal{L}_{int} = 10$ nb^{-1}, or 50 kHz minimum bias Pb-Pb collisions. It is thus clear that a major upgrade of the TPC, both of the read-out chambers and electronics, is required to exploit the high statistics that the LHC can provide. Many physical observables, especially in the heavy flavour and charm sectors (see sec.1.2), are deeply statistics-dependent and would not be valuably measurable, if not even accessible, in the present scenario [19]. The main idea behind the upgrade is thus to substitute the MWPC-based readout chambers and to operate in a continuous, trigger-less readout mode, i.e. without gating. The proposed technology, which combine a comparable spatial and momentum resolution with an intrinsic suppression of the ion back-flow, is the Gas Electron Multiplier (GEM).

3.2 Gas Electron Multipliers

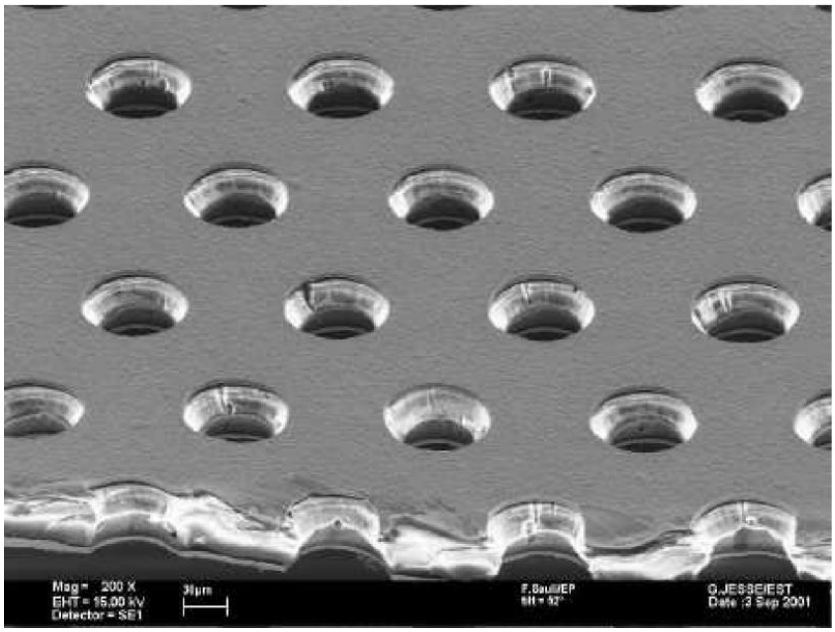

Fig. 3.2: Electron microscope image of a GEM foil.

The Gas Electron Multiplier (GEM) [2] is an amplification technology for gaseous detector introduced by F. Sauli in 1996, at CERN. It is based on the use of thin kapton foils (~ 50 μm) coated with copper layers (~ 5 μm) on both sides, with a high-density matrix of holes through which electrons can pass (fig.3.2). The holes are usually double-conical, with an inner radius of ~ 50 μm and an outer one of ~ 70 μm, disposed on a hexagonal grid of ~ 140 μm pitch. Applying a moderate difference of potential (~ 100 V) between the two conductive sides of the GEM, a strong electric field (~ 10 kV/cm) is created at the center of the holes, where the field lines are focused. Electrons going through produce an avalanche: part is collected on the bottom side of the GEM, and the rest of the electrons drift towards the read-out anode - or the next amplification stage, in a multiple GEM-stack. Symmetrically, ions produced in the amplification process are partially collected on the upper copper layer and partially drift back. Intrinsic ion-backflow suppression is a unique characteristics of GEMs.

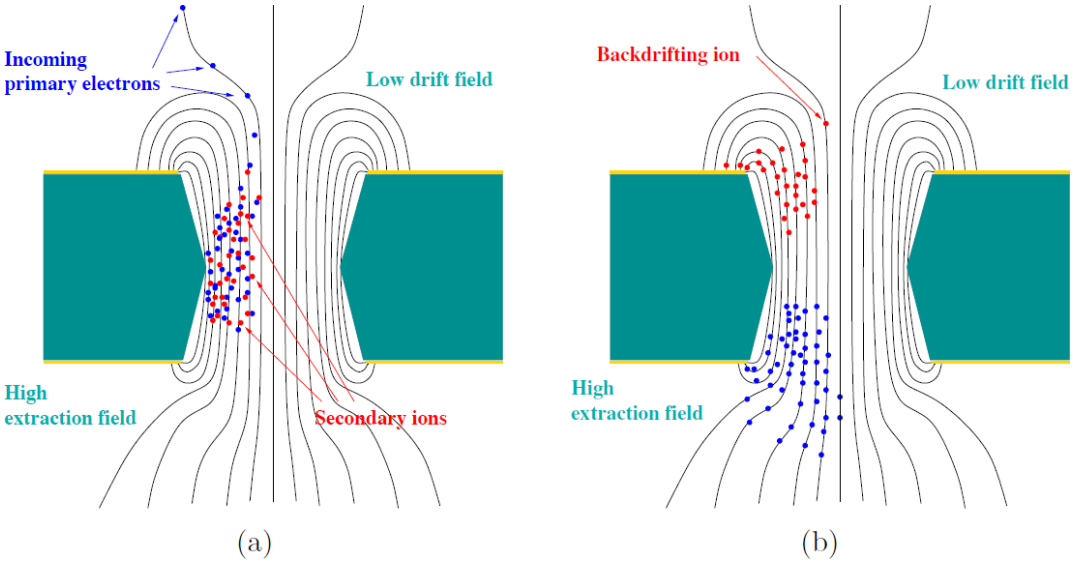

Fig. 3.3: Sketch of the working principle of a GEM: electrons drift into a hole and trigger an avalanche (a); the ions produced get mostly collected, while the electrons drift to the anode (b).

It is convenient to introduce some quantities, that are often used to describe the proprieties of a GEM:

- *collection efficiency* (ϵ_c), the fraction of primary electrons that arrive into a hole,
- *extraction efficiency* (ϵ_t), the number of electrons (ions) extracted from the holes per produced electron (ion),
- *ion back-flow* (IBF), the number of ions reaching the drift cathode per produced electron,
- *absolute gain* (G), the number of electrons produced per primary electron in the amplification process,
- *effective gain* (g), the total number of electrons reaching the anode per primary electron.

These quantities are then related according to:

$$g = G\,\epsilon_c\,\epsilon_t\ . \tag{3.1}$$

The overall amplification, i.e. the effective gain, is exponentially dependent on the voltage applied across a GEM:

$$g = e^{a\Delta U}\ , \tag{3.2}$$

where the coefficient a depends on the GEM geometry. Amplification of a factor of ten thousand can be reached, but usually, to get to such high gains, a set-up of multiple GEMs in a stack is used, operated at lower voltages and thus more stable.

Concerning IBF, it is usually minimized with an asymmetric configuration of fields, lower above a GEM and higher below [39], to have, respectively, worse extraction efficiency for ions and better for electrons (see fig.3.3). In most of the used gas mixtures (Ar and Ne based) values of $\sim 1\%$ have been experimentally reached [37], which is still one order of magnitude above what is normally achievable with a gating grid ($< 10^{-3}$). A strong point of GEMs, compared to MWPCs, is an excellent time resolution, and conversely excellent z resolution in TPC applications. The signal is in fact formed directly by electrons collected at the read-out plane, after the amplification, which means a pulse width of the order of ~ 10 ns. The slow tail induced by the ions is cut off, since their charged is screened by the conductive copper layers.

However, GEMs showed to be more problematic in terms of stability. The reasons is connected to the high charge densities that could be reached inside a GEM-hole and the relatively small distances of the electrodes. Contrary to wire chambers, the formation of a propagating streamer most likely results in an electrical breakdown, as the ionization channel connects the two copper layers and a temporary short is formed.

3.3 GEM-TPC

Since the invention of the GEM, gaseous detectors based on this technology have been extensively used in nuclear and particle physics. The pioneer was the COMPASS experiment at CERN [40], which developed triple-GEM tracking detectors with parallel-plate geometry. They showed excellent proprieties: high efficiency (97%), good space-time resolution (70 μm, 12 ns), stable up to rates of 25 kHz/mm^2 [41]. Since then, several high-rate particle physics experiments, like LHCb [42], PHENIX [43] and TOTEM [44] adopted this technology. Also the CMS experiment at LHC recently planned to upgrade its muon detection system with GEMs [45].

The most notable example for the ALICE experiment is the GEM-TPC prototype [46] developed for the PANDA experiment [47] and recently installed in the FOPI apparatus at GSI. It was possible to test its capabilities in a running experiment, which features a 0.6 T solenoid magnetic field and support detectors for tracking (Central Drift Chambers) and TOF (Resistive Plate Chambers). It was used a beam of 1.7 GeV/c pions colliding on a carbon target, with a rate of $\sim 1.5 \times 10^4$ Hz. The gas was Ar/CO_2 (90/10), in a drift field of 360 V/cm. The amplification was based on a triple-GEM structure, operating at a gain of 3800. The read-out plane, with an inner (outer) radius of 10 (20) cm, consists of 10254 hexagonally shaped pickup pads, with 3.0 mm outer diameter. The space resolution measured at small drift lengths was 230 μm in $r\phi$. A precise gain calibration over the whole readout plane allowed to achieve an excellent energy resolution, $\Delta E/E = 4.4\%$. In fig.3.4 the dE/dx spectrum of the GEM-TPC

prototype is shown. The dE/dx resolution, averaged over all the particles produced, is 14-17%, in the momentum range 200-800 MeV/c [48]. If one considers the relatively small track length (20 cm at high p_t), and thus the small number of samples ($\sim$ 20), there is clearly margin for improvement in the ALICE case.

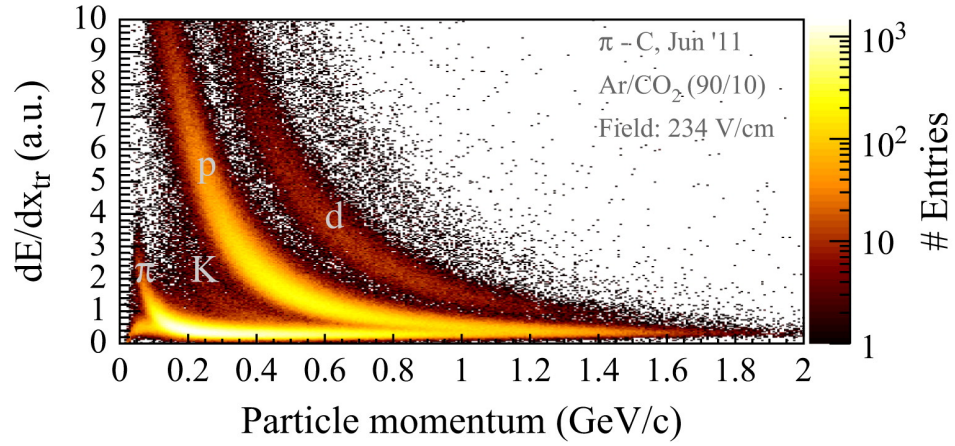

Fig. 3.4: dE/dx as a function of particle momentum in the PANDA/FOPI GEM-TPC prototype, discarding the lowest 5% and highest 25% of all amplitude-sorted samples [48].

The ALICE GEM-TPC must anyway fulfil extra requirements connected to the LHC environment (high multiplicity, high rates), the experimental set-up and the physics objectives. First of all, the excellent tracking capabilities of the current TPC must be preserved. The main problem will arise from the space-charge effect, which will be unavoidably higher operating in un-gated mode. Tracking proprieties are constrained by electron diffusion (dependent on drift length), track inclination angle and total charge density. For tracks of Minimum Ionizing Particles (MIPs) with large p_T, i.e. vanishing inclination angle, the space-point resolution in $r\phi$ and z are between 400 and 800 μm [10]. This sets the intrinsic track resolution, i.e. the mean distance of reconstructed ionization points to the reconstructed track: $\sigma_{\rm intr} \approx 200\ \mu$m. The objective is to properly calibrate the TPC, taking into account the space-charge effect, so to keep distortions of the electron tracks (after correction) below $\sigma_{\rm intr}$, as is achieved in the current TPC. A detailed study of this issue has been performed [37] in the conditions foreseen during RUN 3 at LHC. For a Pb-Pb interaction rate of 50 kHz, and a ion collection time of 0.16 s, $\sim$ 8000 minimum bias collisions contribute to the ion pile-up at any given moment. The effective gain has to be kept at a minimum of 2000, to have a signal-to-noise-ratio of 20. With the minimum IBF usually achievable with triple-GEM detectors ($\sim$ 1%), this translates into a shift of the electron trajectories up to $\sim$ 10 cm, (see fig.3.5) which currently pose serious problems to correction algorithms: latest results arrived at distortions (after calibration) of the order of $\sim$ 1 mm [37]. There are thus two ways to proceed, which are both currently followed by the ALICE GEM-TPC collaboration: one is to improve the correction algorithms, implementing precise calculations of space-

charge density fluctuations and other effects previously neglected; the other is to improve ion back-flow suppression, working on the GEM settings.

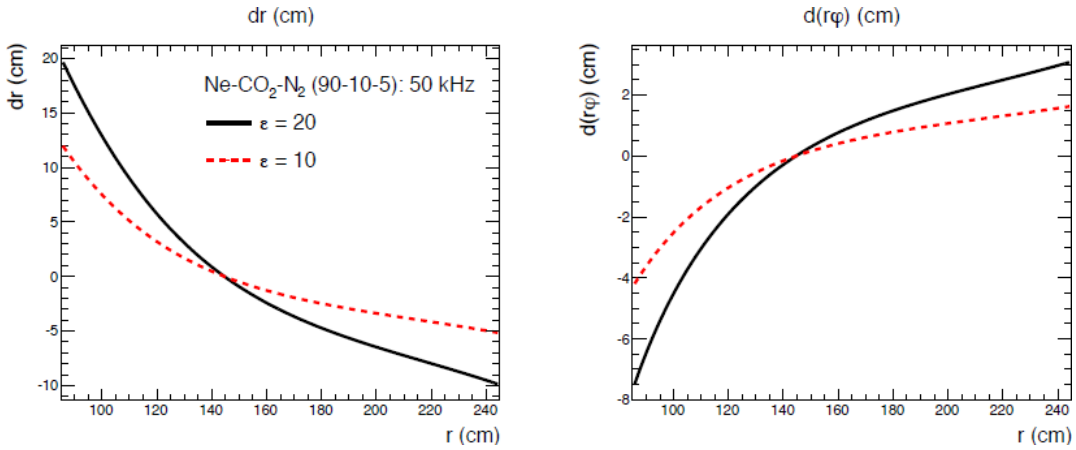

Fig. 3.5: Space-point distortions in r (left) and $r\phi$ (right) close to the central electrode ($z \approx 10$ cm) for $Ne/CO_2/N_2$ (90/10/5). Rate 50 kHz, IBF 1% ($\epsilon = 20$) and 0.5% ($\epsilon = 10$) [48].

In fig.3.6 a typical triple gem stack is shown, as it was first proposed for the ALICE ROCs, with the definitions commonly used for these settings: GEMs are numbered from top to bottom, E_{drift} corresponds to the drift field, E_{ti} denote the transfer fields between GEM-foils and E_{ind} the induction field between the last GEM and the pad plane.

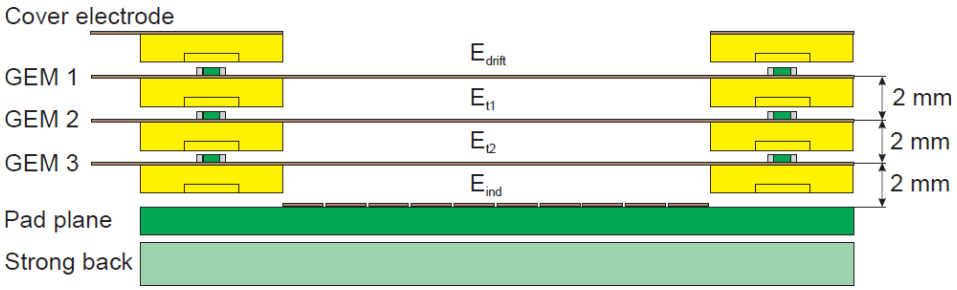

Fig. 3.6: Schematic exploded cross section of the GEM stack. The gaps between subsequent GEM-foils and between the last GEM and the pad plane are 2 mm. Each GEM foil is glued onto a 2 mm thick support frame defining the gap.

To minimize IBF, triple GEMs are usually operated with increasing amplification: $\Delta U\text{GEM1} < \Delta U\text{GEM2} < \Delta U\text{GEM3}$. GEM1, in fact, directly faces the drift volume: any produced ion which is not collected will unavoidably build up space-charge. Amplification is then kept at minimum. Most of ions are produced at GEM3, where there is a higher chance to collect them in the GEMs above. Moreover, using a low transfer field above (E_{t2}) and a higher below (E_{ind}) GEM3, a reduced ion extraction efficiency allows

to block most of them. This propriety is strictly correlated in the difference between the two fields. The upper limits on fields asymmetry are imposed by the first Townsend coefficient $\alpha(E)$: above a certain value of transfer field - $E \approx 5$ kV/cm in the gas mixture currently used in the ALICE TPC, Ne/CO_2 (90/10) - electrons start to be amplified also in the gap between GEM-foils, which then spoils both ion back-flow suppression and stability. This is one of the reasons for which we proposed a different gas mixture, $Ne/CO_2/N_2$ (90/10/5), which allows to get to higher field asymmetry configurations (≈ 5.5 kV/cm).

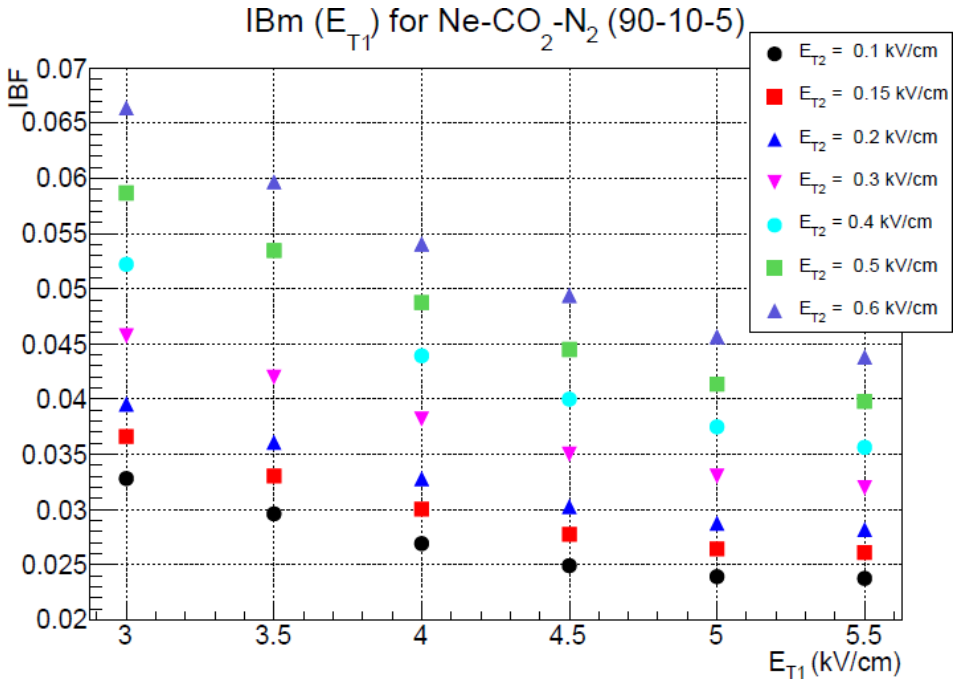

Fig. 3.7: Measured ion back-flow as a function of E_{t1} for several values of E_{t2} [37].

A remarkable R&D program has been pursued at TU-München to study the lower limits on IBF achievable with GEM detectors. With triple-GEM setup in $Ne/CO_2/N_2$ (90/10/5), minimum IBF values of $\sim 2-3\%$ have been achieved, see fig.3.7, despite a careful optimization of voltage and field settings. This led to test quadruple-GEM configurations, with different combination of large pitch (L) foils (280 μm), which are expected to further reduce the ion extraction. With a setting of type S-L-L-S values down to 0.34% have been reached [37], settling a safe working point for operations in ALICE. That is the reason why the quadruple GEM-stack is currently the baseline solution for the GEM-TPC upgrade. Further optimization of fields and GEMs geometry, as well as measurements with ROC prototypes, are nevertheless needed.

Another critical point about the ALICE GEM-TPC is the stability in the extreme conditions foreseen for RUN 3. In particular, for a charged particle density of $\mathrm{d}N_{ch}/\mathrm{d}\eta = 500$, a rate of primary ionization clusters of ~ 100 kHz/cm is expected at the IROCs.

At the nominal gain of 2000, this translate into a current density at the readout anode of ~ 1 nA/cm^2, assuming that all primary particles are MIPs. With a safety factor of 10, which takes into account the contribution of highly ionizing particles, background, secondaries, etc., a maximum current density of ~ 10 nA/cm^{2}s is expected [37]. These values are of course an average over the operation period; single rare events, e.g. the decay of an activated nuclei at the edge of the chamber, are expected to induce higher, even if instantaneous and local, charge densities. The choice of the new gas mixture, $Ne/CO_2/N_2$ (90/10/5), was also motivated by stability reasons, as it was expected that the extra fraction of quenching gas would help in this sense.

In conclusion, ion back-flow suppression and stability are the most critical proprieties of GEM detectors which need to be optimized for future operation in the ALICE TPC.

Chapter 4

Read-Out Chambers

The ALICE TPC read-out chambers are divided in 18 trapezoidal sectors, each covering a range of 20° in azimuthal coordinate. Each of these is further divided, at $r \approx 50$ cm, into an Inner (IROC) and Outer (OROC) Read-Out Chamber. The ROCs, in the GEM upgrade of the TPC, consist of:

- a trapezoidal aluminium frame ("alubody"),
- an extra support frame made of fiber-glass ("strong back"), for the pad plane,
- the pad plane (multi-layer PCB, with the pick-up side divided in pads),
- the GEM-stack.

The overall design of the alubodies will mostly follow the one of the MWPC-based chambers. The mechanical stability will be in fact more than sufficient to prevent deformations due to the weight or the tension of the GEM-foils. Of course, minor modifications are needed for the different high-voltage (HV) scheme, the cut-outs for the new front-end cards (FEC), connected to the pad plane, and the mounting structure of the GEM-stack itself. The pad plane will be adapted to match the active area of the GEM-foils, but the dimensions of the pads are not planned to be changed: 4×7.5 mm^2 (IROC), 6×10 mm^2 and 6×15 mm^2 (OROC) in $r\phi \times r$, for a total of 557,568 readout channels.

The GEM stack consists of several GEM-foils, each one glued to a 2 mm fiber-glass support frame, one on top of the other. The gap between the foils is determined only by the thickness of the frame, i.e. no extra spacer are used. In fig.4.1 and 4.2 the layout of the ROCs and the dimensions of the GEM-foils are shown: $497 \times (292 - 467)$ mm^2 for the IROC, $1142 \times (468 - 870)$ mm^2 for the OROC. The design of the GEM-foils and the frames followed several principles:

- minimize dead areas, not to deteriorate the resolution of the chamber,
- provide the necessary mechanical stiffness,
- allow precise alignment of the different components,

- guarantee the functionality of the chambers even in case of local breakdowns on the GEMs.

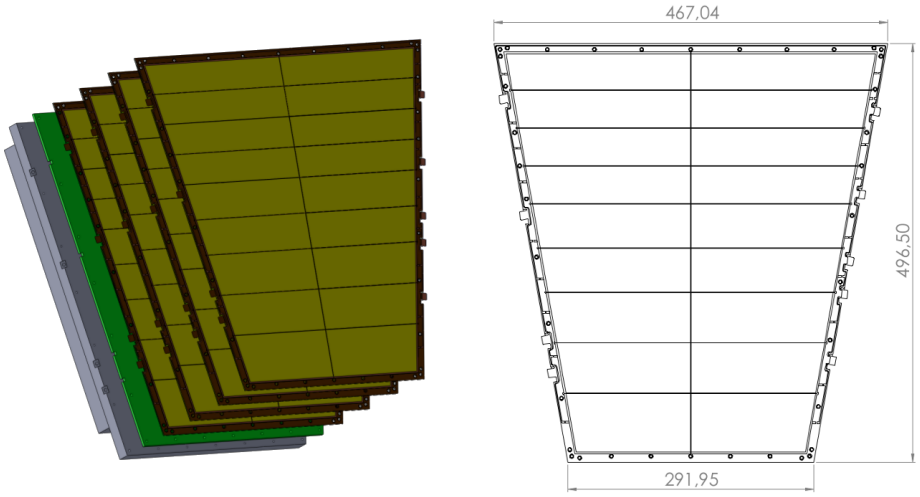

Fig. 4.1: Left: Exploded view of a GEM IROC. Right: dimensions (in mm) of an IROC GEM-foil.

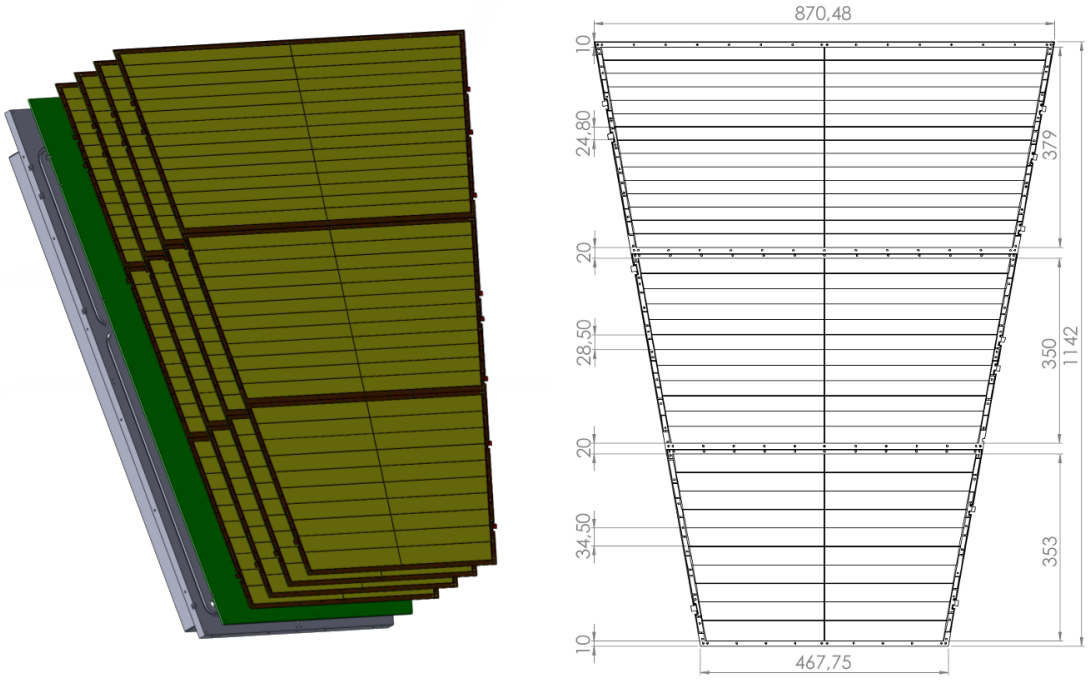

Fig. 4.2: Left: Exploded view of a GEM OROC. Right: dimensions (in mm) of a OROC GEM-foil.

4.1 GEM-foils

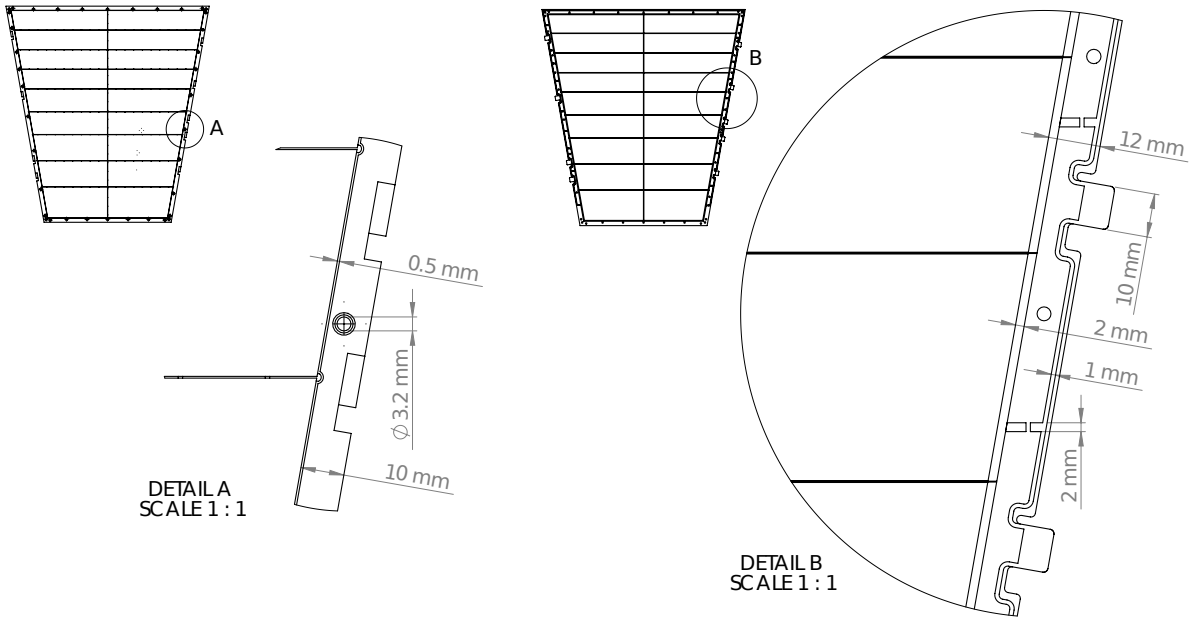

Fig. 4.3: Detailed view of the features of the frames (left) and of the GEM-foils (right), see text.

The details of the GEM-foils and the frames are sketched in fig.4.3. The GEM-foils are made of three layers, two conductive on the exterior (copper) and one insulating in between (kapton). The copper with GEM-holes ("active area") extends over most of the surface; on the sides, a margin (12 mm) is left to be glued to the frame. The frames also feature a 0.5 mm wide, 0.5 mm deep rim around the gluing area, to prevent the glue from slipping into one of the GEM-holes, which could produce a permanent short in the foil.

At the top side of the foil, the active area is divided in trapezoidal sectors, independently connected to the power supply from the sides via a HV pattern implemented on the kapton margin (1 mm wide). The GEM-foil is divided along the azimuthal angle in two parts, with half of the sectors on each. This configuration allows to minimize the dead area along the radial direction, which is most crucial for tracking. On each HV connection, a high-ohmic SMD protection resistor is soldered (1-10 MΩ); in case of a temporary short between the two copper layers, this protection resistor helps to:

- limit the current provided by the power supply, which could damage the foil,
- avoid a voltage drop on the bottom copper layer.

Moreover, thanks to the division in sectors, in case of a local breakdown (i.e. a permanent short), the rest of the foil would still be operating. The sectors are chosen to have

a constant surface of ~ 100 cm^2, which corresponds to an overall stored charge of ~ 2 μC, to reduce the damage to the foil in case of a spark. This scheme have also shown to reduce the probability of propagating a discharge through multiple GEM-foils and the pad plane [49]. The distance between sectors is set to 200 μm, to prevent sparks in case one of them is short-circuited.

Before being glued on the frames, the GEM-foils are stretched with a linear tension $T = 10$ N/cm, to prevent the sagging due to the electrostatic forces and to avoid the formation of wrinkles (and thus field distortions). To achieve a uniform tension, the foils are stretched with a pneumatic tool in their original, rectangular production shape and then cut-out along the frame, after the glue has dried. The overall gluing procedure is summarized in fig.4.4.

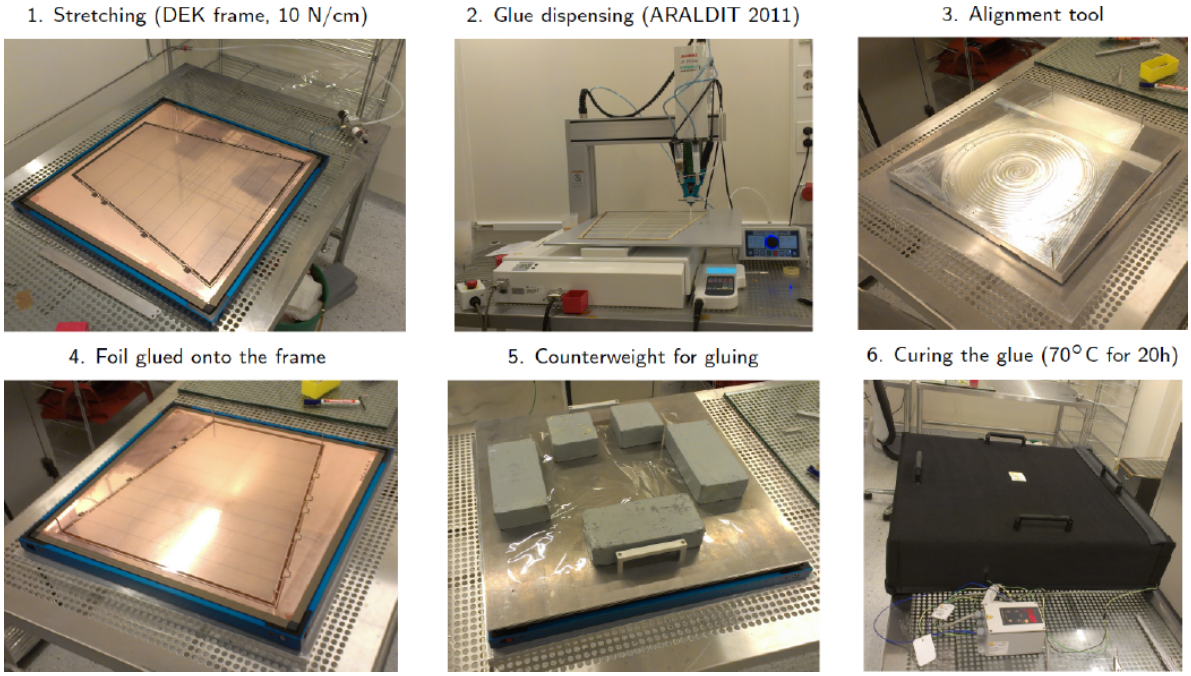

Fig. 4.4: Foil gluing procedure: the IROC GEM-foil, in its original rectangular production shape, is mounted on the stretching tool. The glue is dispensed along the frame, the foil is placed above it and pressed with an aluminium plate, specially milled not to touch the active area. Finally, it is put inside a heating hood for 24h at 60°C, to cure the glue.

In principle, the frame should be as little as possible, to minimize the dead area. The width (1 cm) is constrained by the mechanical stiffness required to sustain the tension of the foils, considering the fixed thickness (2 mm), which sets the distance between the GEM-foils. An extra spacer grid of 400 μm width is placed across the borders between the HV sectors, to prevent the sagging of the foils in case the stretching tension is lost.

Because of the challenging dimensions of the ROCs, the mechanical behaviour of the

GEM-foils under realistic operating conditions has been studied. The crucial aspect to be kept under control is the sag of the foils, due to electrostatic forces, which affects the resulting transfer fields. Two nearest GEM-foils constitute in fact two plates of a capacitor, and thus feel a pressure of:

$$P = \epsilon_0 \left(\frac{\Delta V}{d}\right)^2 . \tag{4.1}$$

In a multiple-GEM stack with equal transfer (or induction) fields this force is compensated by the one attracting to the opposite electrode (GEM-foil or anode), but in general is not the case, like on GEM1, as the drift field is kept smaller than the transfer ones. We therefore use the ideal capacitor model to establish an upper limit on the resulting sag of the GEM-foils.

To compute the deformation of a foil submitted simultaneously to a transversal load P and a tensile force T one has to take into account the flexural rigidity of the different layers. It has been found [50], however, that GEM-foils are much more stiff in bending than in tensioning, i.e. they approximately behave like a cable. For a one-dimensional strip of length l, the maximum displacement $u_{\max}$ would be:

$$u_{\max} = \frac{1}{8}\frac{P\,l^2}{T} . \tag{4.2}$$

For a rectangular foil of sides a,b there is a geometrical factor k dependant on the ratio $\zeta = a/b$:

$$u_{\max} = k(\zeta)\,\frac{P\,l^2}{8T} , \tag{4.3}$$

$$k(\zeta) = \left[1 - \frac{32}{\pi^3}\sum_{n=1}^{+\infty}\frac{(-1)^{n+1}}{(2n-1)^3}\mathrm{sech}\frac{(2n-1)\pi}{2}\zeta\right] < 1 . \tag{4.4}$$

In the present case, the worst scenario foreseen for operations in the ALICE-TPC was simulated: transfer gap $d = 2$ mm, foil thickness t = 60 μm, voltage $\Delta V_{\max} = 1100$ V - corresponding to the maximum transfer field before amplification in $Ne/CO_2/N_2$ (90/10/5) (5.5 kV/cm). Fig.4.6 shows the maximum deformation expected on a GEM foil as a function of its sizes. Thanks to the spacer grid, we limit the boundaries of the free-to-bend foil area to those of the HV sectors: in the worst case, i.e. the upper-most sectors of the OROC, $\sim 2.48\times 43.5\,\mathrm{cm}^2$, a maximum deformation of ~ 4 μm is expected, which is perfectly negligible.

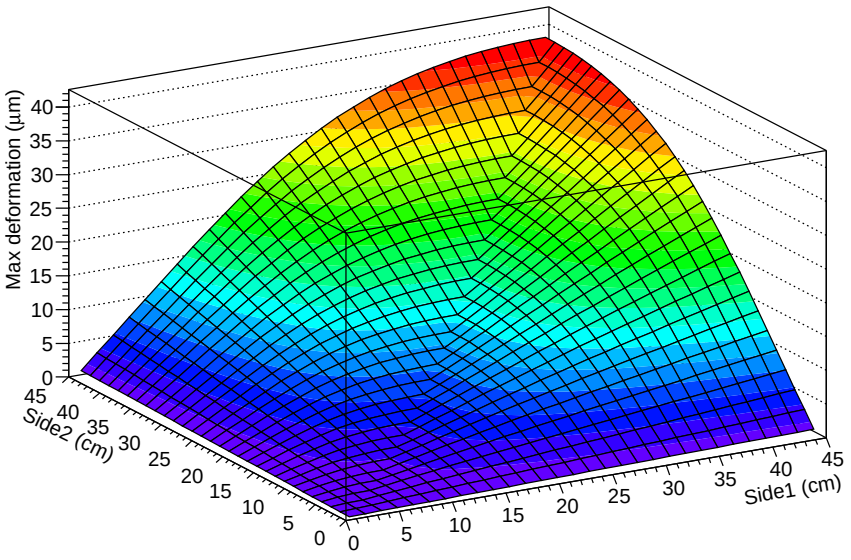

Fig. 4.5: Maximum deformation expected on a GEM foil as a function of its lateral dimensions.

4.2 IROC prototype

A prototype of the Inner Read-Out Chamber equipped with a triple GEM-stack has been built, using the alubody and the pad-plane of the standard MWPC-based IROC. The tests were carried out using a special drift chamber (*test box*), with a drift volume of $57 \times 61 \times 10.6$ cm^3. One the side of the read-out plane there is the GEM-stack and ~ 10 cm above there is the cathode, a thin foil (50 μm) of aluminized mylar; below the GEMs, a cut-out on the alubody allows to connect the front-end cards to the pad-plane. To have a uniform field across the drift volume, there is a 8-strip field cage, with 15 mm pitch. The potential of the field cage strips is set by a resistor chain. The potential of the last strip, closest to the GEM-stack, is adjusted so that it matches those of the GEM1 top electrode. On the lateral sides of the test box, two aluminized mylar windows (60 μm thickness) allow to use radioactive sources and beams for measurements with the IROC.

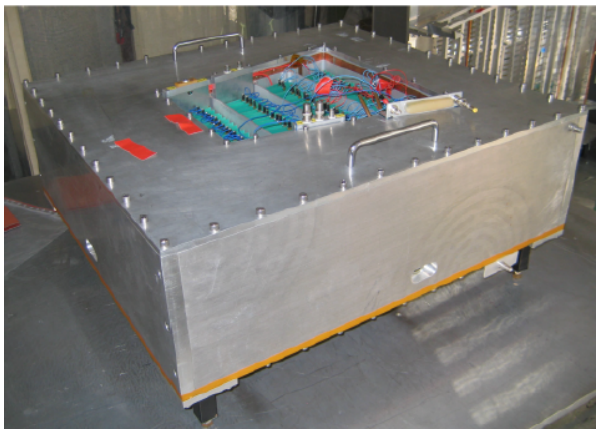

Fig. 4.6: The test box.

In the first tests, the GEM-foils were independently powered up using an ISEG EHS 8060n 8-channel 6 kV high voltage module, while for the drift cathode a ISEG HPn300 30 kV module was used. A dedicated software allowed a constant monitoring of the currents on each HV channel, within 1 nA resolution, with remote control and adjustable tripping behaviour: in case of an over-current detected on one GEM foil, all the channels could be shut down. To ensure a safe discharge of the foils after a trip of the power supply, resistors to ground were added on each electrode. The overall HV scheme is displayed in fig.4.7.

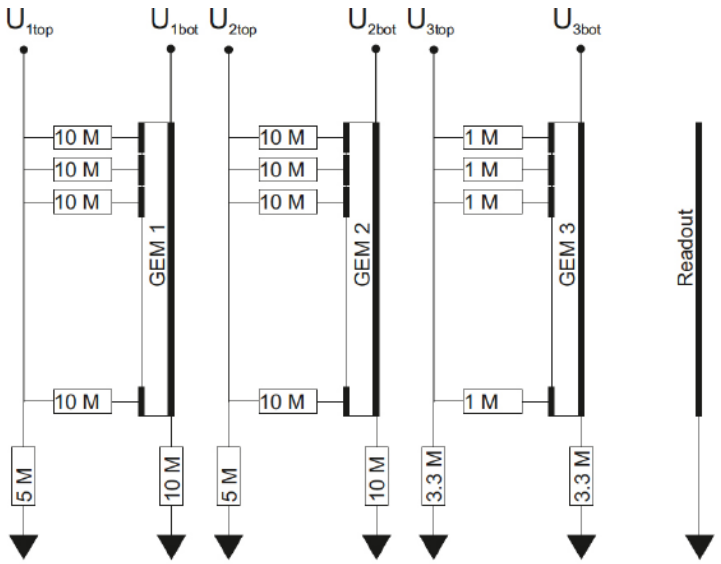

Fig. 4.7: Schematics of the HV distribution of the prototype, showing the protection and grounding resistors.

The choice of the voltages and the fields across the GEM-foils is most crucial for the characteristics of the detector. On one side, as previously pointed out, one has the

optimized settings for ion back-flow suppression: ΔUGEM1 $<$ ΔUGEM2 $<$ ΔUGEM3 and $E_{t2} \ll E_{t1},\ E_{ind}$. On the contrary, to improve the stability of the detector, it is thought to be more convenient to have the biggest amplification (highest ΔU) on GEM1, where one has less incoming electrons, while minimizing those on GEM3. Moreover, to avoid the drop of the electron extraction efficiency associated to low E_{t2} (see sec.6.5), which has to be compensated with higher ΔUGEMs, it is safer to have equal transfer fields across all the GEM-foils. These settings, that will be referred to as "standard" (the name was inherited from [40]), have indeed shown in previous measurements to be more stable [49]. "Standard" and "IBF" are then the first HV settings that were tested with the IROC prototype; the absolute values of the different GEMs/fields, corresponding to an effective gain of ~ 1000 in Ne/CO_2 (90/10), are reported in tab.4.1.

	Standard	Ion-backflow
ΔUGEM1	272 V	225 V
E_{t1}	2.54 kV/cm	3.8 kV/cm
ΔUGEM2	248 V	235 V
E_{t2}	2.54 kV/cm	0.2 kV/cm
ΔUGEM3	218 V	285 V
E_{ind}	2.54 kV/cm	3.8 kV/cm

Table 4.1: Different IROC HV settings, gain ~ 1000 in Ne/CO_2 (90/10).

The first beam test was carried out at the CERN PS, using beams of electrons and pions with momentum between 1 and 6 GeV/c. The drift field was 400V/cm and the gas mixture Ne-CO2 (90-10), as in the current ALICE TPC. The FECs were read out using the current TPC read-out system [25]. The average DAQ rate was 500 events/spill, with a spill length of 0.5 s, for a beam intensity of about 2000 particles/spill. The main objective of this experiment was to test the PID capabilities of the GEM detector. For this reason, only clearly isolated tracks were used in the analysis. Further cuts were applied on the number of electron clusters per track, excluding the 5% lowest and 15% highest fraction. A typical dE/dx spectrum at gain 5000 is shown in fig.4.8. The energy loss resolution is then computed as:

$$\frac{\sigma(dE/dx)}{\langle dE/dx \rangle} \ . \tag{4.5}$$

In the different HV settings and within the momentum range of the beam, values within 10-11% have been reached [37] [51], which is compatible with current MWPCs performances. This first test thus showed that the PID capabilities of the current TPC will be preserved in the GEM upgrade.

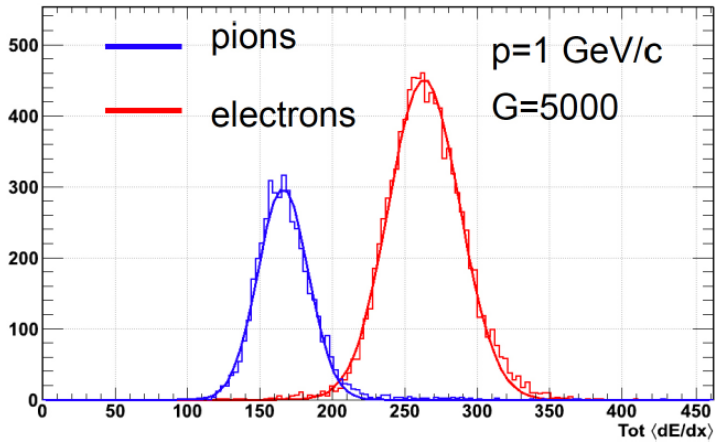

Fig. 4.8: dE/dx spectrum of 1 GeV/c electrons and pions [37].

A second test was carried out at LHC, in the ALICE cavern itself, during the 2013 p-Pb run at $\sqrt{s_{\mathrm{NN}}} = 3.5$ TeV. Again, drift field and gas were the same of the ALICE TPC. In this case the main goal was to test the stability of the detector in the LHC conditions. The detector was installed under the beam-pipe, at $\sim$ 10 m from the interaction point (see fig.4.9). In that position, with the current collision rate, the total particle rate was expected to be $\sim$ 5 MHz per rapidity unit, close to what expected in the TPC rapidity range during RUN3 ($\sim$ 25 MHz per rapidity unit). During 21 days of operation, 21 trips of the power supply occurred, mostly with IBF settings. No correlations were found between the trips and beam conditions or instabilities in the other ALICE detectors. The most probable reasons of these trips were sparks occurring between the two conductive layers of the GEM-foils. At the end of the test, the detector was disassembled to search for evidence of discharges: in all the problematic sectors, a brownish area on the copper layer around a GEM-hole was visible (see fig.4.10), which clearly indicates a spark occurred. Even if the detector was still operating after the test, the resistance between the two sides of a GEM-foil decreased in seven sectors; because of the lower potential drop, the effective gain was reduced as well.

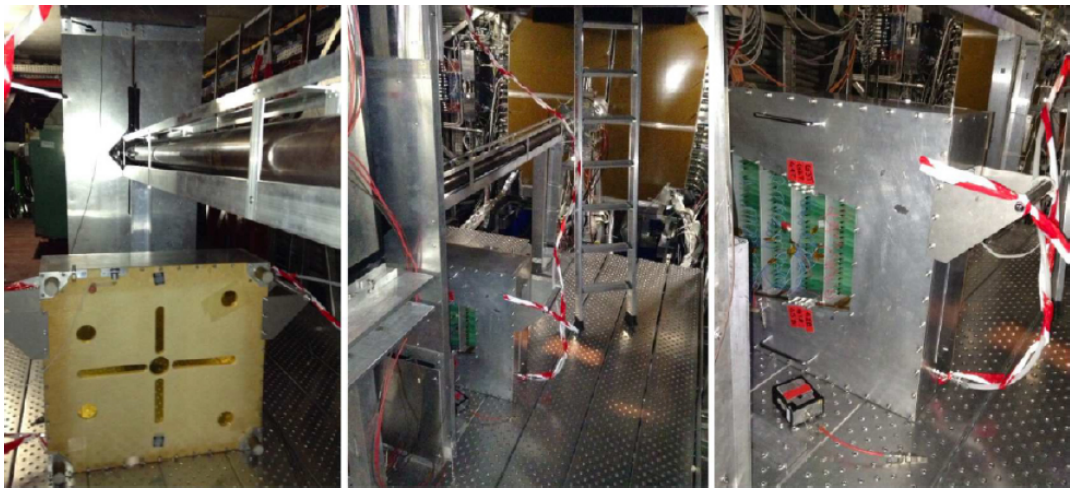

Fig. 4.9: Views of the prototype installed underneath the LHC beam pipe, in the miniframe used to service the ALICE detectors [37].

Considering the long period of operation the ALICE TPC has to sustain, such a high rate of discharges, which could introduce inefficiencies in the gain or even permanently damage GEM-foil sectors, is not acceptable. The LHC experience showed the necessity of further studies and tests on the stability of the detector. There was also the need to introduce new improvements in this sense. In the context of this work, we proceeded on two parallel ways: on one side, we prepared and performed another beam-time test with an upgraded IROC prototype, trying to reproduce the LHC conditions in terms of charge density across the detector. On the other, we started an extensive R&D program on smaller GEM detectors, to understand the influence of different parameters (gas choice, HV scheme, electric fields) on stability.

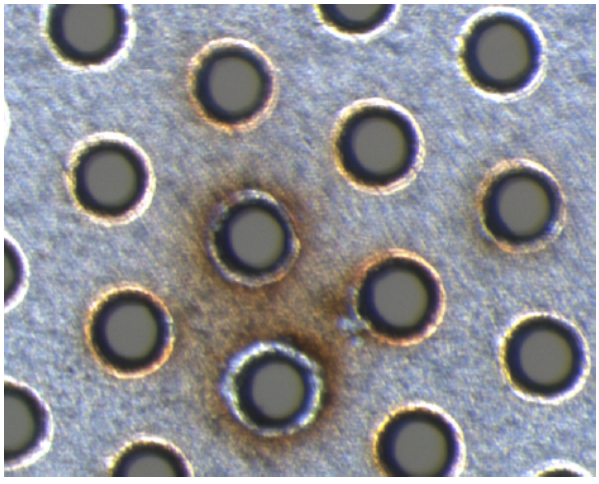

Fig. 4.10: Typical appearance of a GEM-hole after a discharge.

Chapter 5

IROC stability tests

This dedicated stability test was aimed to precisely measure the discharge rate (discharge per particle) in the GEM IROC prototype under beam conditions. It was performed at the Maier-Leibnitz-Laboratorium (MLL), [52] located at the TU-München campus, in Garching (Germany). The facility features a tandem van de Graaff accelerator with a maximum terminal voltage of $\sim$ 10 MV (fig.5.1), which is then able to accelerate ions up to 20 MeV. The maximal beam current can reach up to $\sim$ 1 μA ($\sim 10^{12}$ Hz). In the hall of the experiment (Hall II), the maximal beam current is limited to 10 nA (10^{10} Hz) for radiation protection purposes.

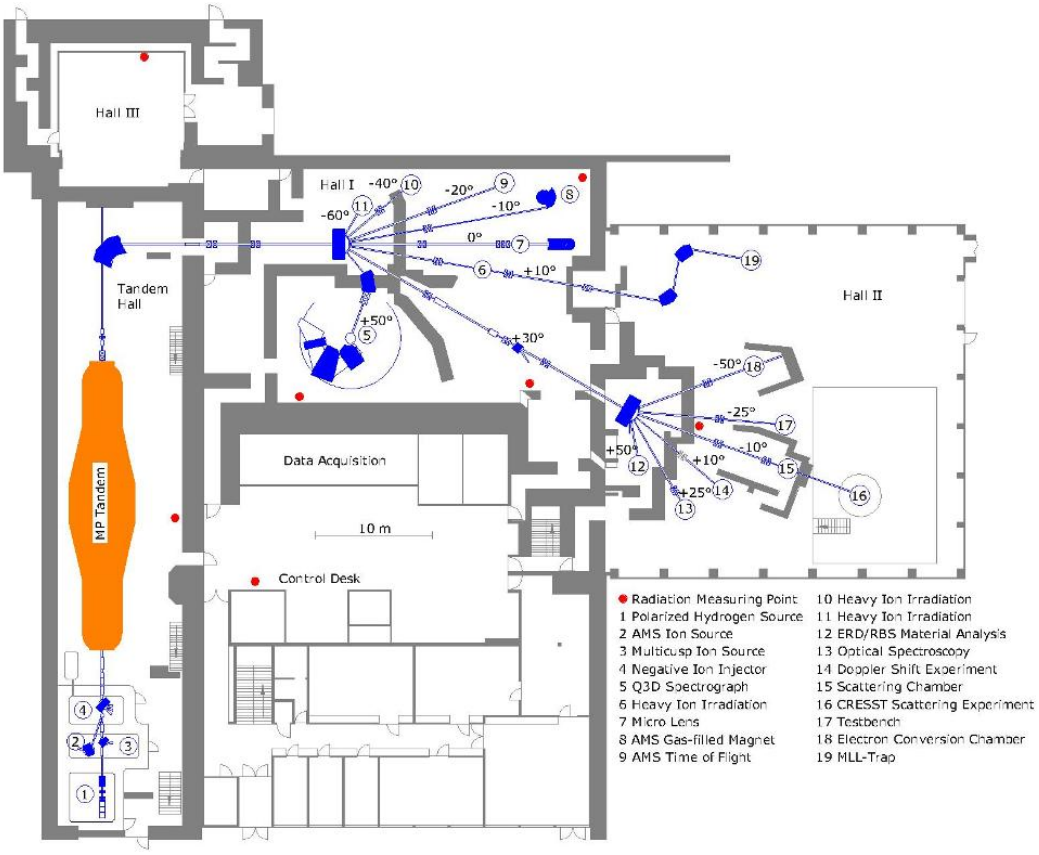

Fig. 5.1: A map of the Maier-Leibnitz-Laboratorium (MLL). The experiment was located in Hall II, -10°.

A beam of low-energy protons was used, which deposit a high charge density along their tracks, allowing to get even above the LHC conditions in terms of current flowing across the GEMs (see sec.5.1). To achieve a uniform irradiation over the detector, the beam was orientated parallel to the GEM-foils, across the two mylar windows on the sides of the test box (fig.5.3).

Several modifications were introduced after the LHC tests in the detector, including the new gas mixture $Ne/CO_2/N_2$ (90/10/5), with an extra fraction of quenching gas (N_2). As it was measured later (see sec.6.2), this already introduces a consistent improvement in terms of stability. To preserve the functionality of the foils also in case of multiple discharges, a different HV scheme is used. Even if all the resistors were chosen to minimize large voltage drops in case of a HV trip, the slow reaction time (100 ms) of the power supply could actually unavoidably lead to such scenarios, which in turn are dangerous for the GEM-foils. Moreover, the necessary grounding resistors impose relatively large time constants before all the elements are discharged. The use of a voltage divider (fig.5.2) allows to prevent the problem. The time constants for discharging the foils after HV trips are also expected to be at least an order of magnitude lower. A voltage U_{tot} is supplied on one channel by the power supply and then distributed according to a series of resistor. For each GEM:

$$\Delta U_i = R_i \frac{U_{\mathrm{tot}}}{R_{\mathrm{tot}}} \ . \tag{5.1}$$

And the same applies for the potential difference between different foils, defining the transfer and induction fields.

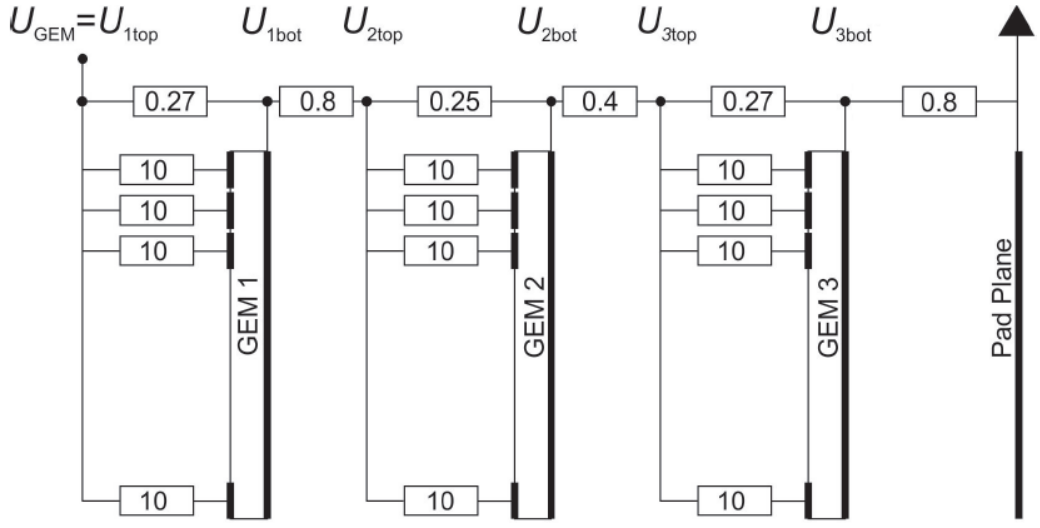

Fig. 5.2: Schematics of the HV distribution via a resistor chain (values in MΩ).

5.1 Simulations

The crucial parameter for this stability test is the charge flowing across the GEM-foils, or current per unit area (A/m^2). A dedicated study with Geant4 [53] was then carried out to simulate the energy deposition and straggling of the protons in the the detector. In fig.5.3 a sketch of the set-up used in the simulation is shown. In particular, the simulation includes all the components of the beam-line and of the test box with which the beam can interact: the kapton window, at the exit of the beam-line, the air gap between the latter and the detector, the aluminized mylar of the test box windows, the field strips and the gas volume, including the areas outside of the drift volume. We neglect possible electron losses due to field distortions at the edge of the field cage, as there are extra 10 mm of the frame before the active area of the GEM-foils.

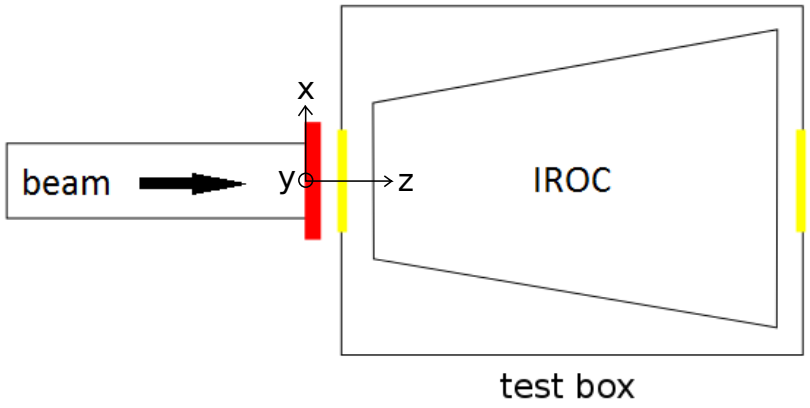

Fig. 5.3: Schematic view of the simulated geometry. In red, the window at the end of the beam line, in yellow the windows of the test box.

In fig.5.4 the energy deposition in the drift volume as a function of the proton energy is shown. In principle, stopping the protons in the drift volume allows to reach higher local ionization densities (*Bragg peak*), but at the cost of not having a uniform irradiation of the GEM-foils. For this reason, the energy of the protons is chosen to be 20 MeV: in fig.5.5 the energy loss dE/dz across the 49.65 cm length of the GEM-foils is shown. For a proton energy of 20 MeV we expect a total energy deposition on the active area of $E_{\text{dep}} = 1.10 \pm 0.05$ MeV. It is worth to note that the biggest contribution to the uncertainty does not come from the energy straggling of the protons - which would result in fluctuations of the deposited charge - but from the distance of the detector from the beam window, as it was not mechanically fixed and the measurements performed lack of precision. Apart from this systematic error, the irradiation of the detector is uniform, which is what is relevant in this experiment.

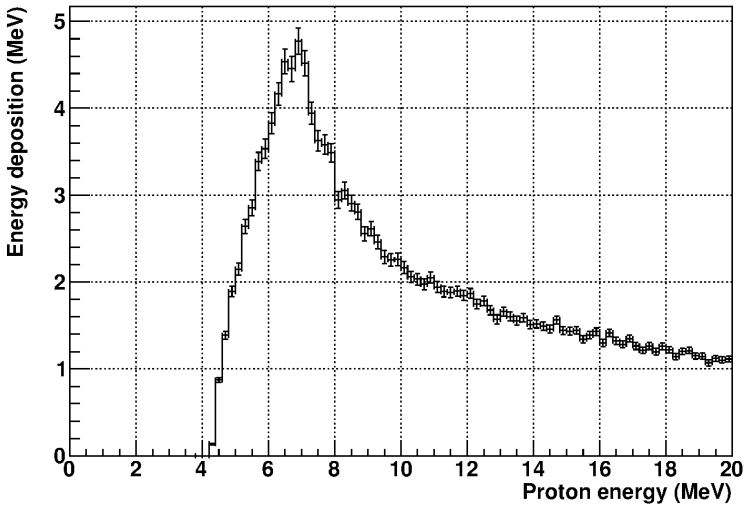

Fig. 5.4: Energy deposition in the drift volume as a function of the initial proton momentum.

In our gas mixture, $Ne/CO_2/N_2$ (90/10/5), which has an effective ionization potential $W_i = 37.285$ eV, and at nominal gain $g = 2000$, we thus expect at the last GEM-foil a total charge per proton Q:

$$Q = \frac{E_{dep}}{W_i}\, g\, e = 9.4 \pm 0.4 \text{ nC} , \tag{5.2}$$

where e is the elementary charge. To estimate the area of the GEM-foils irradiated by the ionization tracks, the lateral deviation of the protons from the beam axis due to multiple scattering was needed. This is usually not an issue in gas detectors, because of the low density of the absorber, but with low energy protons it has to be taken into account. The initial profile of the beam in the simulations is adjusted according to experimental measurements (see sec.5.4), assuming for simplicity a gaussian density distribution, centred on the beam axis. The protons distribution at the output window is shown in fig.5.6. From this simulations, we don't expect the protons to be stopped on the GEM-foils, which may induce a higher discharge probability [49].

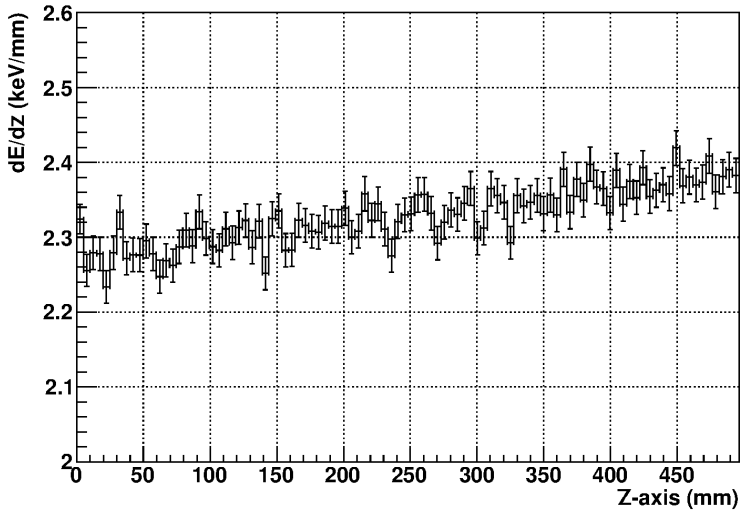

Fig. 5.5: Energy loss dE/dz across the active area of the GEM-foils, for 20 MeV protons.

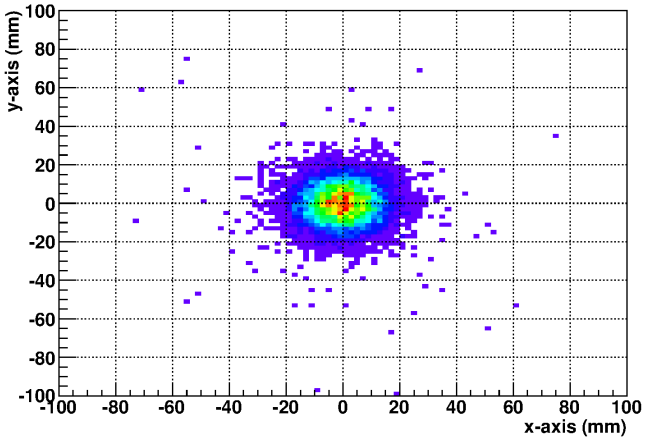

Fig. 5.6: Proton position distribution at the exit window of the test box. Beam-axis is in (0,0). GEM-foils are located at $y = -53$ mm.

The overall current in the GEM-foils is determined by the amplification of the primary electrons along the ionization tracks. At the rates used in our experiment (10-250 kHz), no pile-up of the electrons amplification is expected in the GEM-foils. The ions, which are collected on the GEMs in $\mathcal{O}(1\mu s)$, do not accumulate as well. We then expect only primary electrons from single tracks to contribute to the current. This simplify the estimation of the current density. The lateral size of the electron clusters along the tracks is rather small, as the range of most of the primary electrons is within a few μm. The dominant contribution on the final charge density at the GEM-foils comes from the

transverse electron diffusion. In $Ne/CO_2/N_2$ (90/10/5) at $E_{drift} = 400$ V/cm, $D_T = 223$ $\mu m/\sqrt{cm}$ (see sec.6.5), i.e. the cluster spatial extension σ expected after a drift length $\Delta y \approx 5$ cm is:

$$\sigma = D_T \sqrt{\Delta y} \approx 498 \ \mu m \ . \tag{5.3}$$

Since the scattering of the protons along y is isotropic, the average diffusion of the clusters is unaffected. Considering an average energy loss along the track $\langle dE/dz \rangle \approx$ 2.35 keV/mm (see fig.5.5), the charge density per proton at $g = 2000$ is:

$$\left\langle \frac{dQ}{dA} \right\rangle = \frac{\langle dE/dz \rangle}{W_i \, \sigma} \, g \, e \approx 4.05 \ \text{pC/cm}^2 \ . \tag{5.4}$$

5.2 Read-out and set-up

A previously explained, a discharge consists of a propagating streamer connecting the two copper layers of a GEM-foil, across one or more GEM-holes, which then has two unambiguous signatures in:

- *Voltage drop* across the foil, because of the temporary short; conversely, the current supplied by the power supply rises.
- *Huge charge released* - for one sector, up to $\sim$2 μC - which induces a big signal on the pad-plane.

The set-up that was developed allowed to monitor both. Compared to the TPC-related tests, is possible to simplify read-out scheme, since a full reconstruct of the proton tracks was not needed. The Front End Cards (FECs) connected to the pad-plane are divided into four rows, perpendicular to the radial direction of the IROC (see fig.5.7). For each row, the signals of the FECs are summed up, ending up with four pad-plane sectors read out in total. This choice allowed to control that the protons were not stopped inside the detector and, at the same time, to simplify the read-out scheme and minimize the data flow.

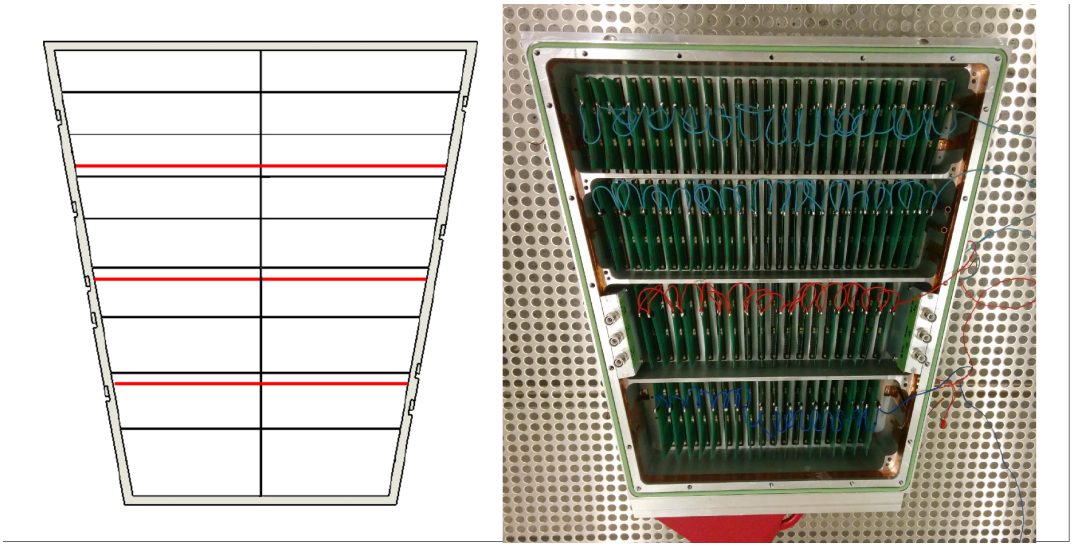

Fig. 5.7: Left: sketch of the four pad-plane sectors read out (in red), superimposed to the IROC GEM foil. Right: picture of the back of the alubody, with the four rows of cards defining the pad-plane sectors.

Discharge signals had been previously observed to be big enough to be discriminated without any additional amplification from the electronics. In our case, however, is important to keep constant track of the beam conditions, to disentangle possible discharges from fluctuations in the proton rate or from bunches of multiple protons. It is then needed to simultaneously record the energy spectrum of the beam and the number of discharges.

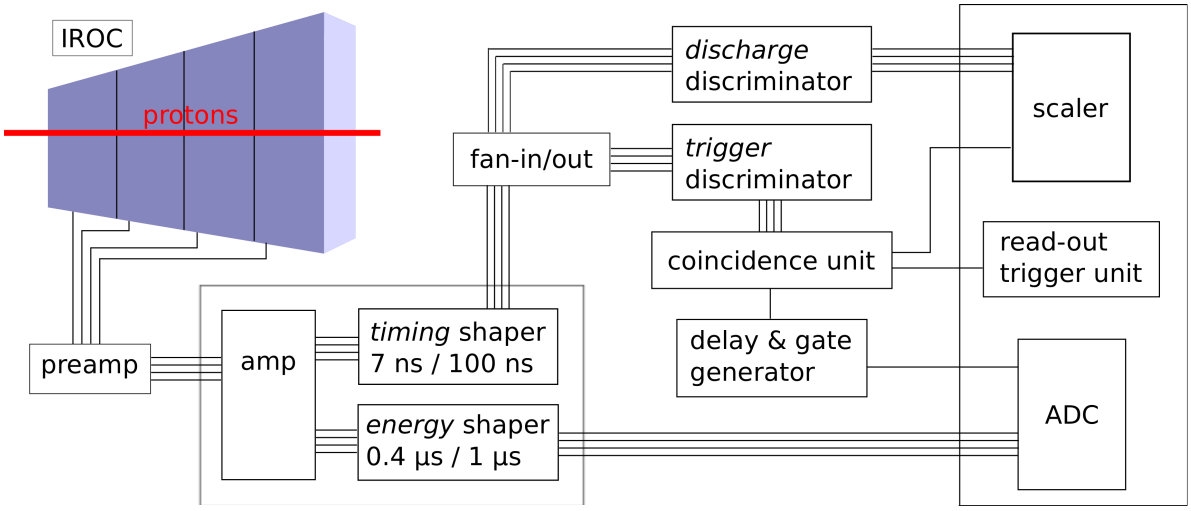

Fig. 5.8: Sketch of the read-out scheme.

The overall read-out scheme is shown in fig.5.8. At first, the raw signal from the pad-plane is amplified and then split. The two branches are shaped with different time constants, according to the different purposes: the *slow* signal (0.4 μs rise / 1 μs decay time) is digitalized in an ADC, while the *fast* one (7 ns rise / 100 ns decay time) provides the signal both for the discharge counter and the read-out trigger. The discharges, selected with a high threshold discriminator, are counted with a scaler. The trigger condition is three proton signal in coincidence out of four channels; this choice takes into account local inefficiencies and gain fluctuations, plus the possibility of loosing a sector of the GEM foil after a discharge. The trigger also provides the gate to the ADC, after a delay set to make it match the *slow* signal. The scaler and the ADC are located in a common VME crate with a processor board (*Power PC*), which reads out both modules simultaneously according to the trigger signal. This allows to correlate *event-wisely* beam conditions and discharges, which is crucial to have a meaningful measure of the detector instability. The modules used were a Mesytec MPR-16 charge sensitive pre-amplifier, a Mesytec STM-16+ shaper, a CAEN V560 16CH scaler and a CAEN V785 32CH peak sensing ADC.

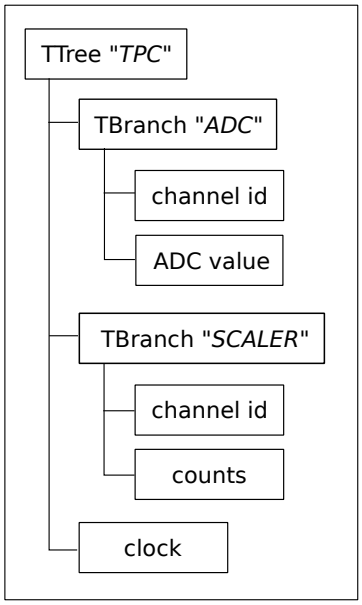

Fig. 5.9: Structure of the data file.

The Power PC is read out via a dedicated software, based on the Multi-Branching System (MBS) [54] DAQ software, developed at GSI (Darmstadt) and adapted for this experiment. The data from the ADC and the scaler are saved in a ROOT file, for off-line analysis; the structure is shown in fig.5.9. Two channels of the scaler are dedicated to count the trigger signals and the event time, using a 1 Hz logic signal from a pulser. An additional on-line monitoring of the scaler data was also implemented. Besides the total counts, it also shows the counting rate (counts per second), to easily access the the proton (from the trigger signal) and discharge rate.

The detector is powered using an ISEG EHS 8060n 8-channel 6 kV high voltage module for the three GEM-foils and the last strip voltage of the field cage, and by an ISEG HPn300 30 kV module for the cathode voltage. The modules are controlled via SNMP over a WIeNeR M-Pod controller, which is connected to a dedicated PC. The HV is controlled using a slow control program developed by [55] and re-adapted for our experiment. The program allows to set the tripping behaviour - current limits, trip time - of the different channels (resistor chain, last strip and cathode) and to monitor the currents on-line.

5.3 Detector and read-out commissioning

The IROC was equipped with a triple GEM-stack of standard-foils (140 μm pitch, double-conical holes, 50 μm inner diameter). The GEMs were powered up with a resistor chain. Tab.6.3 shows the different HV settings, corresponding to a gain of 2000 in $Ne/CO_2/N_2$ (90/10/5), that were used in this experiment. Previous experiences suggested that "IBF" HV settings worsen the stability of the detector: the aim was then to disentangle the effects of the two main parameter which differ with respect to the "standard" settings, i.e. the low E_{t2} and the reversed amplification scheme (ΔUGEM1 $< \Delta U$GEM2 $< \Delta U$GEM3). For this reason a hybrid setting, "reversed", with same fields as "standard" and same amplification distribution as "IBF", was used.

	Standard	**IBF**	**Reversed**
ΔUGEM1 (V)	284	227	213
E_{t1} (kV/cm)	2.6	3.0	2.6
ΔUGEM2 (V)	260	278	260
E_{t2} (kV/cm)	2.6	0.1	2.6
ΔUGEM3 (V)	227	318	298
E_{ind} (kV/cm)	2.6	3.0	2.6

Table 5.1: Different IROC HV settings, gain 2000 in $Ne/CO_2/N_2$ (90/10/5).

The effective gain was calibrated using an ^{55}Fe γ source (5.89 keV), placed right behind the cathode of the test box (made of 50 μm of aluminized mylar) and pointing towards the drift volume. Knowing the energy E_γ of each photon, the charge deposited in the detector is simply E_γ/W_i, where W_i the effective ionization potential of the gas used. Knowing the rate ν of the source, the current expected at the anode, without amplification, is:

$$I_{exp} = \frac{E_\gamma}{W_i} \nu e \ . \tag{5.5}$$

The ratio between the current measured at the pad-plane I_{meas} and the expected one is then the effective gain:

$$g = I_{meas}/I_{exp} \ . \tag{5.6}$$

The rate of the ^{55}Fe source was extracted from the energy spectrum, after background subtraction, dividing the integrated area by the live time of the measurements (i.e. excluding the dead time).

Fig.5.10 shows a typical ^{55}Fe energy spectrum in Ar/CO_2 (90/10). The photons are expected to be fully absorbed in the drift volume, which then translates in a single-peaked spectrum corresponding to fully ionizing energy deposition. However, in argon-based mixtures, there is a competitive mechanism. The photon can remove an electron from the inner K-shell of the argon atoms (binding energy $E_B = 3.21$ keV), leaving

behind an Ar^+-ion; the latter could either emit an Auger electron carrying an energy close to E_B, which is most probably stopped in the drift volume (resulting in a full-energy signal), or a low-energy photon, which on the contrary can escape without ionizing the gas atoms. There is thus a small probability of having a signal corresponding to an energy of $E = E_\gamma - E_B = 2.68$ keV.

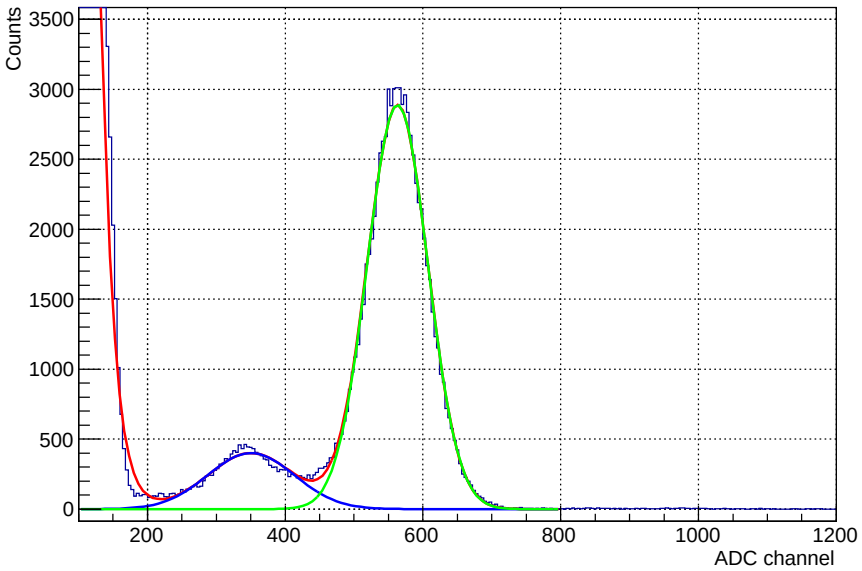

Fig. 5.10: ADC spectrum of ^{55}Fe photons in Ar/CO_2 (90/10), "standard" HV settings, gain $\sim 10^4$, fitted with the sum of an exponential and two Gaussian functions (red). The resulting peaks after background subtraction are shown, corresponding to an energy of 5.89 keV (green) and 2.68 keV (blue).

The effective gain depends on the amplification in the GEMs, mainly set by the gas proprieties and the ΔUGEM, and on the transfer fields in between, as they determine the collection and extraction efficiency of the electrons. It was then necessary to calibrate each HV setting independently for each gas mixture. In fig.5.11 the gain calibration curves used in this experiment are shown. One can notice that for "IBF" settings higher voltages on the GEMs (see tab.6.3) are required to compensate the low electron extraction efficiency after GEM2, due to the low E_{t2}.

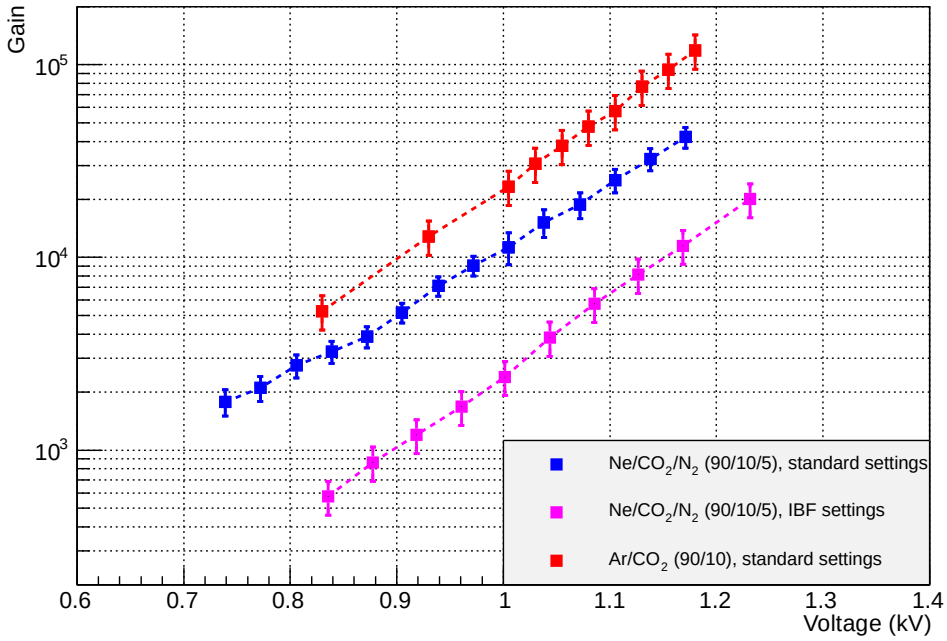

Fig. 5.11: Gain calibration curves for $Ne/CO_2/N_2$ and Ar/CO_2 (90/10). The voltage refers to the total voltage applied on the GEMs and distributed, among them, via the resistor chain.

After properly calibrating the detector, it was needed to check whether the discharge signals could be clearly discriminated from the signals of protons. For this, a low rate ($\sim$ 0.5 Hz) gaseous ^{222}Rn source, which emits α-particles (5.49 MeV), has been used. The energy deposition is $\sim$ 20 times higher than that of protons: in case of a full energy deposition over one pad-plane sector (i.e. one channel), 5.49 MeV for α-particles versus 1.1 MeV / 4 pad-plane sectors = 0.257 MeV for protons. The discharge signal, on the contrary, depends only on the charge stored in the GEM sectors. The ^{222}Rn source thus provided a safe benchmark for the purposes of this experiment. It should be noted, however, that it was used a pre-amplifier with 20 times higher input range, to avoid it to saturate. Fig.5.12 shows a typical discharge signal on the oscilloscope. Since the ^{222}Rn atoms are homogeneously diffused in the gas and the direction of the α-particles is isotropic, some of the ionization tracks ($\sim 3-6$ cm, depending on the gas, see fig.6.8) do not entirely lie in the drift volume and they do not result in a full energy signal. This explains why the energy spectrum (fig.5.13) presents a long tail preceding the full-energy peak.

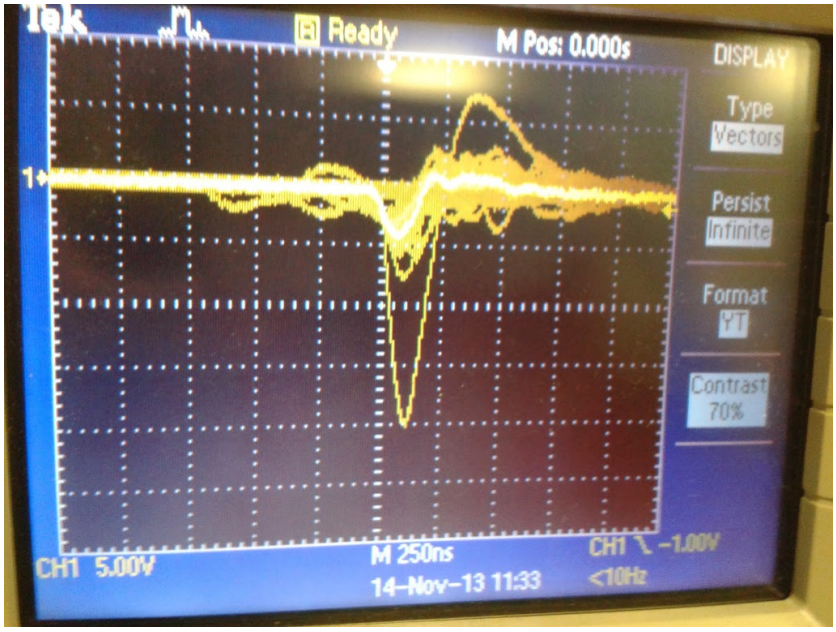

Fig. 5.12: Typical discharge signal at the oscilloscope, after shaping and amplification. The smaller signals are from 5.49 MeV α-particles (see text).

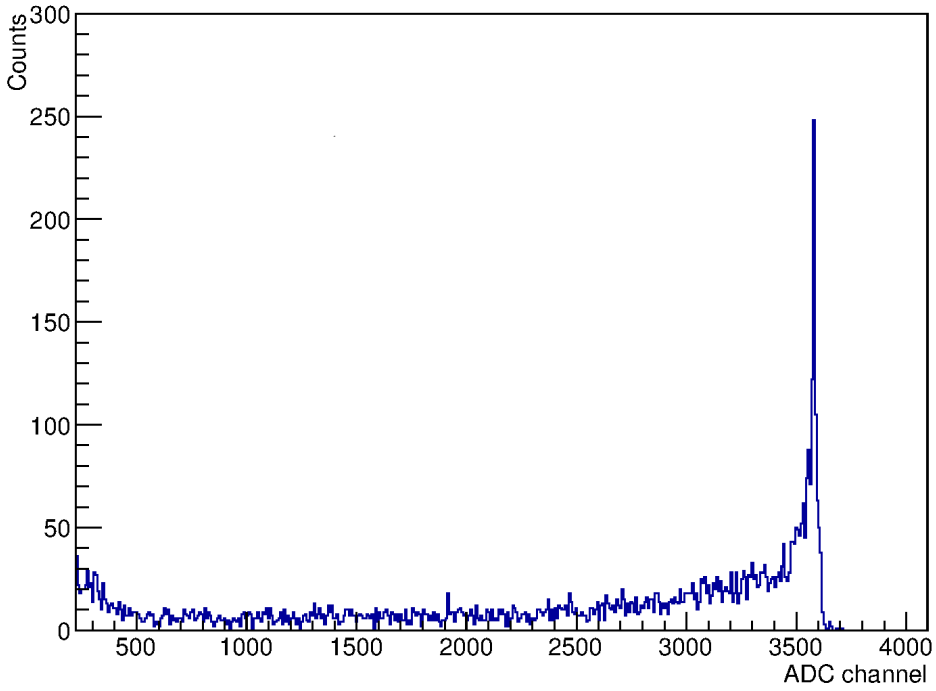

Fig. 5.13: ADC spectrum of ^{222}Rn α-particles in Ar/CO_2 (90/10); "standard" HV settings, gain $\sim 10^4$.

5.4 Results

As seen from simulations (see sec.5.1), it was first needed to estimate the beam lateral profile, to compute the surface of the GEM-foils irradiated by the beam and the energy deposition distribution. We used a CsI scintillating crystal placed in front of the beam window. Since the crystal emits photons in the visible range, it was sufficient to use a camera to have a direct view of the beam profile. With a reasonable margin, the beam was estimated to be focused within ± 5 mm.

The gas used during all the proton runs is $Ne/CO_2/N_2$ (90/10/5). In connection with the ALICE GEM-TPC project, the priority was to test the stability of the different settings, especially the "IBF" ones, at the gain of 2000 foreseen for real TPC operations. The proton rate is set at 10 kHz, which corresponds to an expected current density of 40.5 nA/cm^2, of the same order of magnitude of what expected at LHC in 50 kHz Pb-Pb collisions ($\sim$ 10 nA/cm^2) [37], during RUN 3. A typical energy spectrum in one of the pad-plane sectors is shown in fig.5.14: the single energy peak, followed by a small amount of pile-up. For a signal pulse width $\tau \approx 2$ μs, set by the shaping time, the probability of tail pile-up (interval between pulses $\Delta t < \tau$) at a rate $\nu = 10$ kHz is $P(\Delta t < \tau) = 1 - e^{-\nu\tau} \approx 2\%$, which explains the tail after the proton peak, as the integrated area corresponds to $\sim 3\%$ of the one of the peak itself.

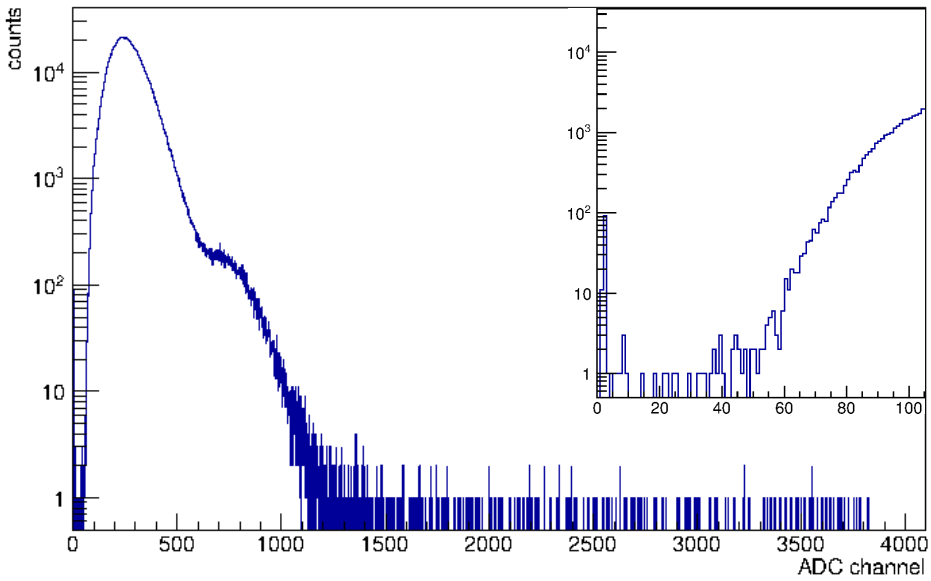

Fig. 5.14: ADC spectrum of protons, "IBF" HV settings, gain 2000.

During the first runs, each one $\sim$ 1 h long, no discharges were observed in the different settings, allowing us to establish lower limits of discharge probability in such conditions (tab.5.2).

HV settings	Gain	Current density (nA/cm^2)	Disch. Prob.
Standard	2×10^3	40.5	$< 2.5 \times 10^{-8}$
IBF	2×10^3	40.5	$< 2.5 \times 10^{-8}$

Table 5.2: Limits on discharge probability: gain 2000, 10 kHz proton rate.

Since no discharges were recorded, the "reversed" HV settings were not tested. To set the limits of our detector in terms of amplification capabilities in such harsh environments, the gain is increased, scaling the potential U_{tot} supplied to the resistor chain in steps of $\Delta U/U_{\text{tot}} = 5\%$, in $\sim$ 16 min long runs. Because of the voltage divider HV scheme, in order to increase the gain the transfer fields have to change as well. However, while the amplification on GEMs can be increased by one order of magnitude with $\sim +10\ \Delta U$, the proprieties associated to the transfer fields, which correspondingly change by $\sim 10\ \Delta U/2$ mm ≈ 0.05 kV/cm, are less affected.

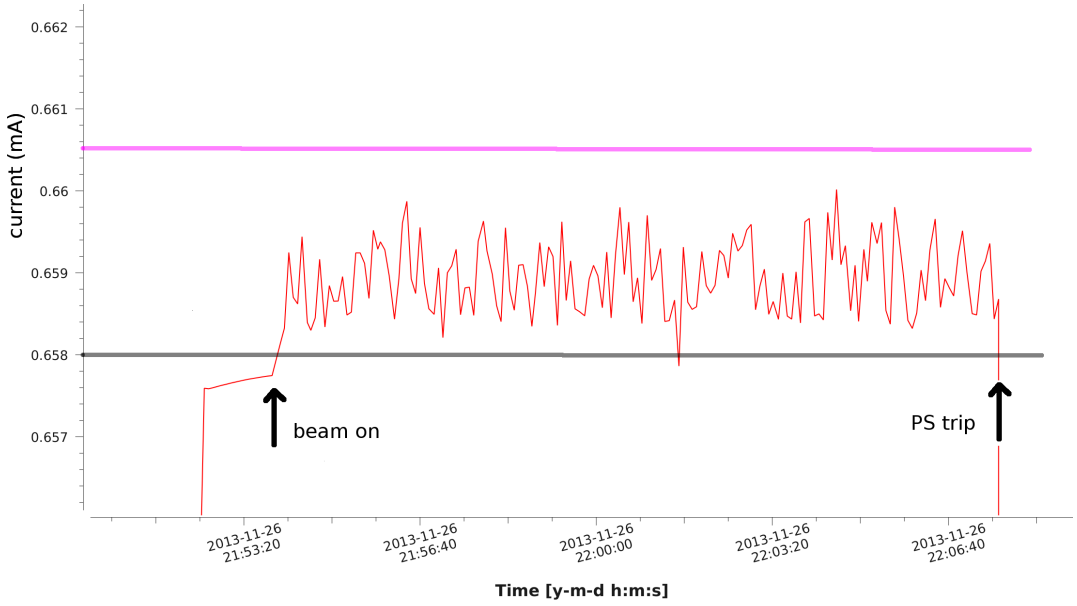

Fig. 5.15: Typical current measurement. The gray line shows the current expected from the standard powering of the resistor chain, the magenta line indicates the current limit set to record a trip, $\sim 2\ \mu$A above. When the beam was turned on, a fluctuating current appeared, because of the amplification process in the GEM-foils. When a discharge occurred, the power supply (PS) tripped, even if the over-currents were too fast to be recorded.

The proton rate was kept constant at 10 kHz. Above $g \approx 10^4$, the pre-amplifier was saturated by standard signals of protons, making impossible to discriminate discharges from the pad-plane signals. The discharges were then detected only from the over-currents measured by the power supply. In particular, the current limits were set below

the rises expected in case of a discharge ($\sim$ 2 μA) and the trips of the power supply were then recorded. In the conditions of our experiment, because of the great charge deposited by the protons, the amplification mechanism itself induced a non-negligible fluctuating current, which had to be taken into account while setting the thresholds. A picture of the current monitor during the beam, with the threshold set for the power supply trips, is shown in fig.5.15.

In "standard" and "reversed" HV settings no discharges were again recorded, up to $g = 1.23 \times 10^5$, above which the chamber started to show instabilities (power supply trips) even without the beam. The corresponding lower limits are then reported in tab.5.3.

HV settings	**Gain**	**Current density** (nA/cm^2)	**Disch. Prob.**
Standard	$(0.45 - 1.23) \times 10^5$	91 - 1646	$< 1.7 \times 10^{-7}$
Reversed	$(0.45 - 1.23) \times 10^5$	91 - 1646	$< 1.7 \times 10^{-7}$

Table 5.3: Limits on discharge probability: scan on gain, 10 kHz proton rate.

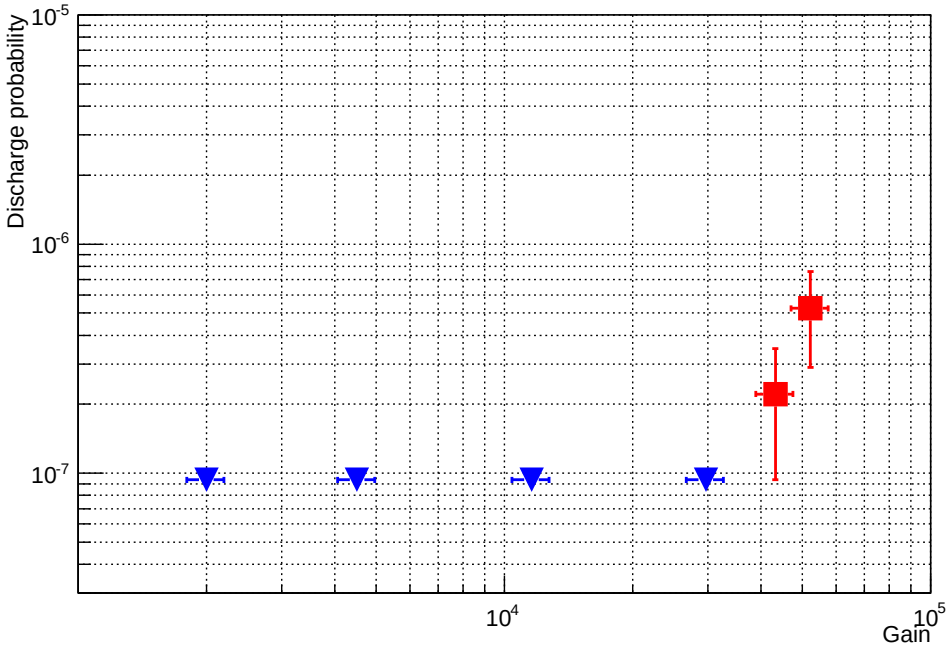

Fig. 5.16: Discharge probability as a function of gain, recording trips of the power supply, in "IBF" HV settings. Blue points are lower limits, red points established values (see text).

The only discharges were recorded with "IBF" settings above $g \approx 4.3 \times 10^4$ (expected current density $\sim$ 91 nA/cm^2), see fig.5.16. Above a gain of $g = 5.2 \times 10^4$ the current

fluctuations due to the beam itself became of the same order of magnitude as the current limits, which again made impossible to discriminate discharges from the measurement of the over-currents.

The final test was performed increasing the beam intensity at a fixed gain of 2000. Since the only discharges appeared with "IBF" HV settings, only these were used. Also in this case the limits of the read-out were reached, as pile-up started to dominate in the signal processing. The extrapolation of the real proton rate was based on an independent measurement of the beam intensity, using a Faraday cup placed right after the accelerator. Within the limits of the read-out, the rate measured with the IROC and the beam intensity measured with the cup were linearly correlated (see fig.5.17); above ~ 50 kHz, the read-out reached saturation. From a linear fit, it was possible to estimate the proton rate through the IROC; the limit of the fit region corresponds to 50 kHz rate measured with the IROC, which corresponds to a probability of tail pile-up of $\sim 5\%$.

Because of the pile-up, it was not possible to exploit the signals from the pad-plane to measure discharges; they were measured via the trips of the power supply due to over-currents. The rate was increased step by step, until 258 ± 8 kHz (expected current density $\sim 1045 \pm 32$ nA/cm^2). No discharges were recorded, allowing to set lower limits on discharge probability (tab.5.4).

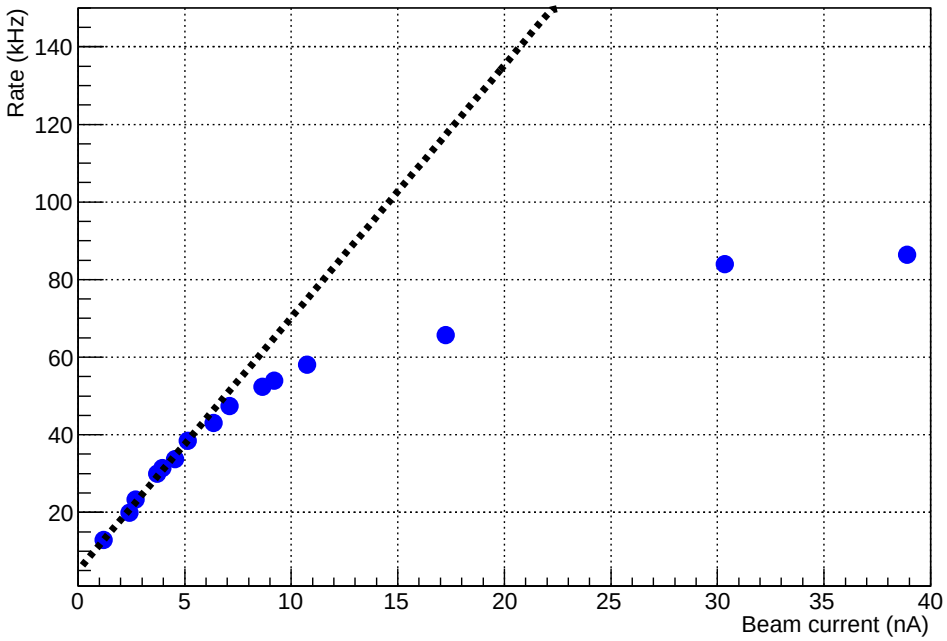

Fig. 5.17: Rate measured with the IROC as a function of the beam intensity. The real rate is extrapolated from a linear fit within 50 kHz.

HV settings	**Max p rate**	**Current density** (nA/cm^2)	**Disch. Prob.**
IBF	258 ± 8 kHz	1045 ± 32	$< 3.9 \times 10^{-8}$

Table 5.4: Limits on discharge probability: scan on proton rate, gain 2000.

Within the limits of the beam intensity and of the statistics that was collected, the detector was stable. Also with "IBF" HV settings, which previously showed to be more problematic in this sense, no discharges were observed up to high gains, ~ 10 times higher than what is foreseen to be used in ALICE, and current densities ~ 100 times higher than those expected in 50 kHz Pb-Pb collisions during RUN 3.

Comparing these results with what was experienced in previous beam tests, two main differences have to be pointed out, which were probably connected to the better stability observed:

- The new gas mixture, with an extra fraction of quenching gas (N_2).
- The direction of the beam, parallel to the GEM-foils.

As previously said, in fact, the direction of the ionization tracks with respect to the GEMs can also play a role: the interaction of the particles with the GEM-foils could lead to very high, very localized clusters of electrons, ending up in one GEM-hole, which would then more likely trigger a discharge. However, other previous observations were confirmed in this test: there is still an indication that the voltages and the fields ($\Delta U\text{GEM}_i$, $E_{ti,\text{ind}}$) do play a role in terms of stability, as was measured later (sec.6.4), and that the settings optimal for ion back-flow suppression worsen the stability of the detector.

This test constituted an important benchmark for the GEM-IROC prototype, that militates in favour of the possibility to sustain the ALICE TPC scenario during RUN 3. Further tests at LHC are nevertheless required to unambiguously prove the reliability of the detector. As a final remark, concerning the future of the ALICE GEM-TPC project, it's important to evidence that the latest modification foreseen for the detector, featuring a quadruple GEM-stack, are expected to introduce an additional improvement in terms of stability, as the GEMs could be operated at lower voltages and the electron distribution among different GEM-holes would be enhanced, thus reducing the maximum GEM-hole charge density. Further tests with this new configuration are of course also needed.

Chapter 6

Discharge studies

The test with the IROC prototype was performed to measure its limits in an extremely harsh environment, with the latest settings foreseen at that time for the ALICE GEM-TPC upgrade. These settings were chosen to fulfil the requirements that are most crucial for the TPC, mainly the IBF suppression, while no systematic study of their influence on stability was ever performed. The main purpose of this work was then to study this influence, with the objective to find a common working point between IBF suppression and stability. Many different detector's parameters can play a role:

- gas choice,
- voltages on GEMs,
- transfer and induction fields.

Since the mechanisms involved in the formation of discharges in GEMs are still known only to a limited extent, it was not easy to foresee how these parameters could affect stability. For this reason, we carried out a dedicated study using a smaller triple-GEM detector. The choice of a smaller detector was mainly motivated by having more flexibility in changing the settings and, eventually, in substituting damaged GEM-foils, and by requiring less gas consumption; however, since the GEM-foils and the HV settings used had the same characteristics of those of the IROC, this measurements are expected to provide direct insight on its limits.

What is also important in the framework of this study is to give a consistent explanation of the measurements, to disentangle the results from the specific experimental set-up and extract a general model of discharge formation in multi-GEM detectors, which could be successfully applied to estimate its stability in different scenarios. This was partially accomplished by a detailed simulation of the detector and the microscopic picture of the GEM amplification. The relevant quantities which were studied are:

- primary ionization density across the drift volume,
- maximum number of electrons produced on each GEM,
- charge sharing between different GEM-holes.

6.1 Detector and read-out

A triple-GEM detector was used, with a small drift chamber, sketched in fig.6.1. The signal is read out from a single pad, the anode, of 8x8 cm^2, above which a triple GEM-stack of 10x10 cm^2 standard foils (140 μm pitch, double-conical holes, 50 μm inner diameter) is placed. The distances between the GEM-foils are 1.8 mm. The cathode is placed 2.5 cm above the GEMs. The surrounding box features two windows, one on the side and one above (aligned to a small hole on the cathode), of thin kapton (50 μm), for measurements with radioactive sources.

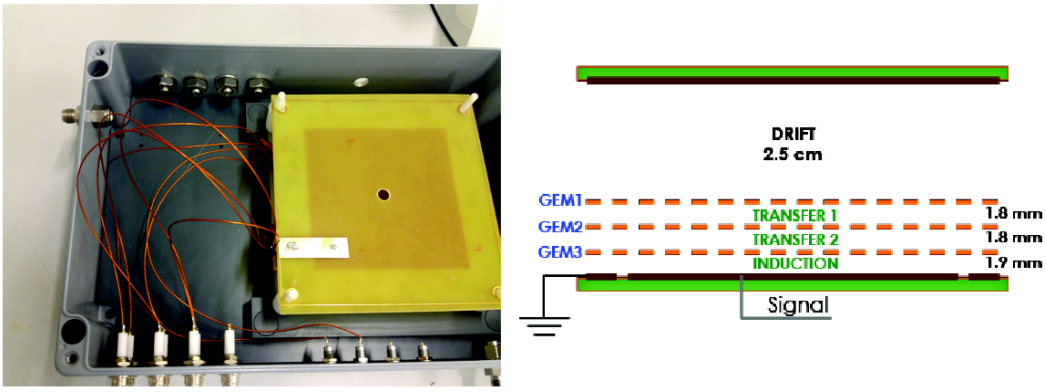

Fig. 6.1: Left: top view of the small triple-GEM detector. Right: sketch of the GEM-stack used in the measurements.

The read-out scheme is shown in fig.6.2. The signal induced at the anode is either processed in an amplifying-shaping branch, to record the energy spectra, or used to identify discharges: the raw signals are attenuated by 14-18 dB, i.e. factor $\sim 5-8$ on amplitude, before being discriminated (fixed threshold of -1 V) and then counted on a scaler. The same low rate ($\sim$ 0.5 Hz) gaseous ^{222}Rn source is used, both to calibrate the read-out and for the discharge measurements. A typical signal from a discharge, after attenuation, is shown in fig.6.3 (left).

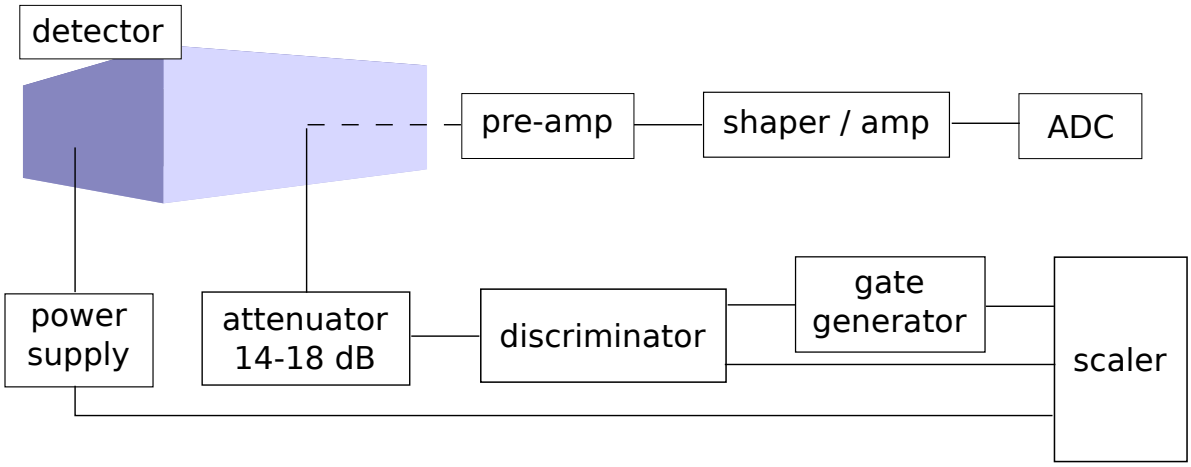

Fig. 6.2: Sketch of the readout scheme.

Discharge signals are usually rather long ($\sim$ 1 μs) and noisy ($\sim$ 20% oscillations in amplitude): to avoid multiple counting from the signal tail, a gate ($>$ 1 μs) is generated from the discriminator and used to veto the scaler. It has also been observed that two discharges may appear in sequence, separated by a time interval of $\sim$ 60 μm, see fig.6.3 (right); since the source rate was much lower, the two are most probably associated to the same highly ionizing event. It would then be the case of a *propagating discharge* across different GEM-foils. Since for protection reasons the HV was supplied via a resistor chain, it was impossible to monitor the currents on the single GEMs and thus confirm this interpretation. Nevertheless, some insight can be had on the underlying physical process from the time scale involved.

Fig. 6.3: Discharge signals at the oscilloscope (yellow) and the gate generated from the discriminator (blue), with pulse height scale 1 V/div. Left: single discharge signal, with 200 ns/div time scale. Right: double discharge event, with 20 μs/div time scale.

It is definitely higher than the typical drift time of the electrons across the GEMs ($\sim 10 - 100$ ns). On the contrary, the time scale roughly matches the drift time of ions between GEMs: the second discharge could then be caused by the back-drifting ion charge-cloud produced in the first one.

Because of the limitations of our apparatus, no further studies were done around the causes and the nature of these propagating discharges. Since they were triggered by the same event, according to the definition of discharge probability (discharge per particle) used in this study, they were counted as one discharge. The multiple counting was avoided using a longer gate (1 s) for the scaler. The dead time, that was taken into account in the computation of the α-particle rate, was anyway small compared to the typical discharge rates that were measured (10^{-3}–10^{-6} Hz). The rate of the ^{222}Rn source was measured with two independent methods: from the energy spectrum, using the amplifying-shaping branch of the read-out (see fig.6.2), and counting the un-attenuated raw signals, discriminated with a proper threshold. Both methods give comparable results within statistical uncertainties.

The effective gain was calibrated using the ^{55}Fe low-energy γ source (5.89 keV), placed on the window above the cathode and pointing towards the drift volume. The principle was the same of the one used with the IROC: record the energy spectrum, measure the rate of the source and, knowing the energy deposition, extract the gain as the ratio between the current measured at the anode and the expected one, without amplification. Gain curves were taken with every HV setting in every gas. As a reference, the calibration of some the different configurations used in these measurements are reported in fig.6.4.

The low rate source set the main limitations in terms of the statistics that could be collected: to measure discharge probabilities down to $\sim 10^{-5}$, ~ 3 days of measurement were required. This forced to measure at very high gains ($> 10^4$), above the typical operative values of $g \sim 2000$. It has to be mentioned that these long term measurements could have been affected by gain fluctuations due to pressure and temperature variations, as extensively observed with gas detectors [57], which were partially corrected calibrating the gain at the beginning and the end of each measurement. Nevertheless, the biggest contribution in the uncertainties of the effective gain was due to the measurements of the current at the anode, which usually had a relative error of $\sim 10\%$.

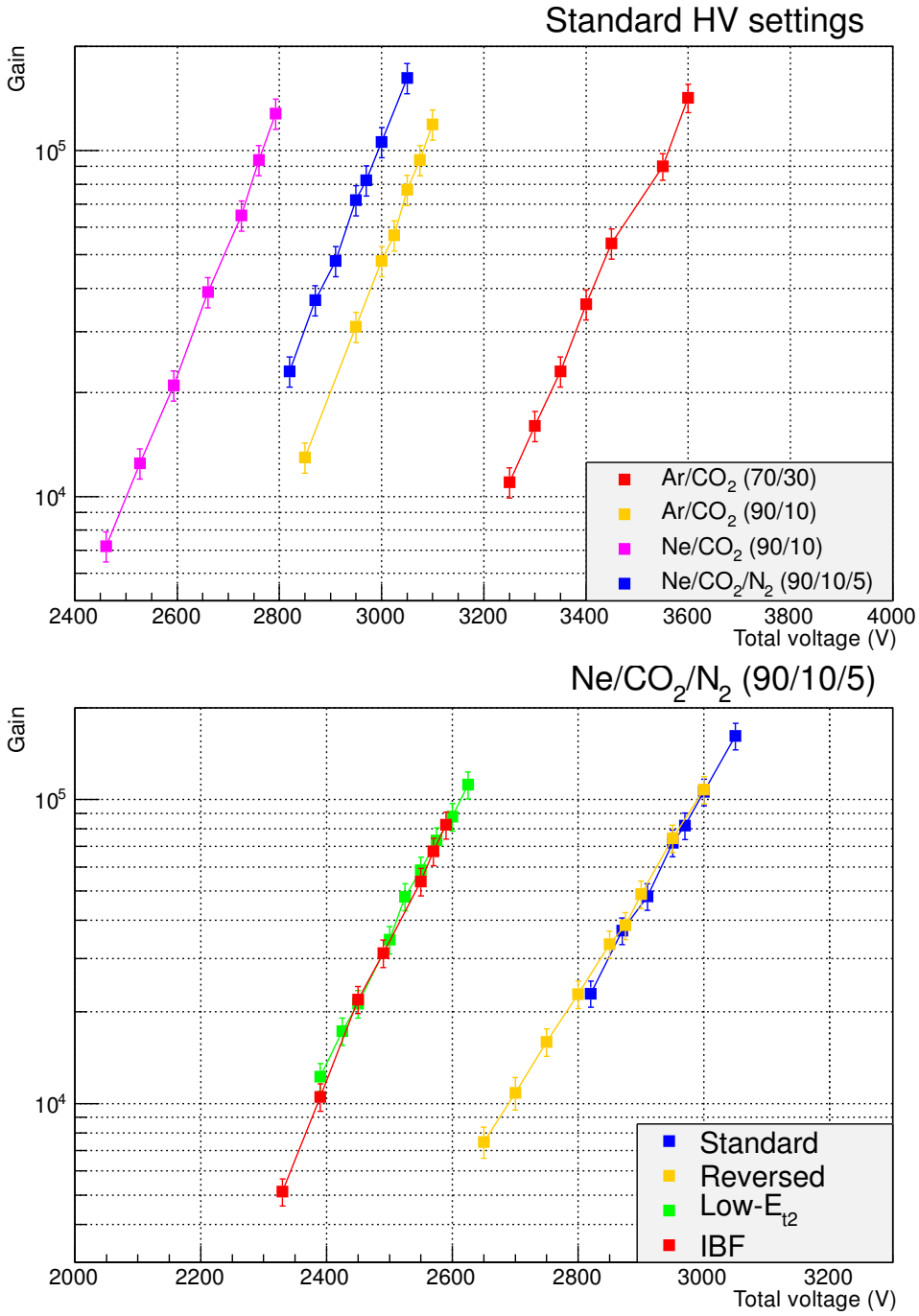

Fig. 6.4: Gain calibration in different gases with "standard" HV settings (up) and with different HV settings in $Ne/CO_2/N_2$ (90/10/5) (down). The total voltage is the one applied to the resistor chain.

6.2 Gas effects

The first measurements were aimed to establish the contribution of the different gas mixtures on the discharge probability. It has to be evidenced that no systematic studies on triple-GEM detectors were ever made in this sense. There are different indications regarding limits of operation in argon-based mixtures, as they were used by many GEM detectors built so far: Ar/CO_2 [41] [46], Ar/CF_4 [58], $Ar/CF_4/C_4H_{10}$ [59]. The only extensive study on discharge probability was performed in Ar/CO_2 (70/30) [49], however focusing on the effects of other parameters (number of GEMs, HV settings). For neon-based mixtures, on the contrary, there is only a limited experience in real applications [57] and no dedicated studies of its stability in GEM detectors. Considering, more in general, Micro-Pattern Gas Detectors (MPGDs), some observations were made [60] concerning the differences between argon and neon in Micromegas [61] detectors, concluding that with the latter higher gains could be reached before the appearance of discharges.

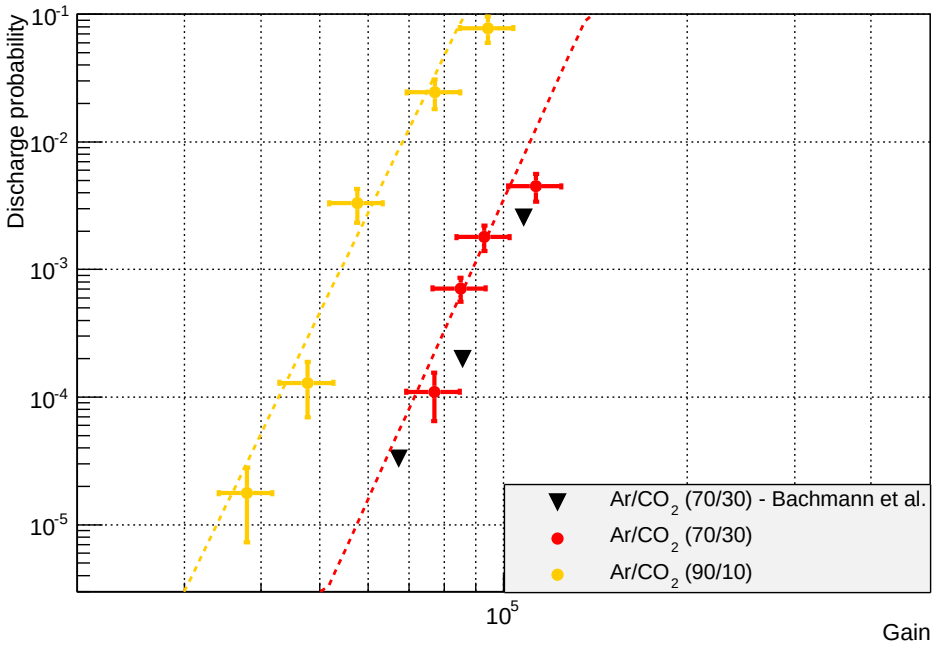

Fig. 6.5: Discharge probability as a function of gain in argon-based gas mixtures, with "standard" HV settings, compared with measurements from [49] (Bachmann et al.).

The discharge probability was first measured in two argon-based gas mixtures, as a function of the effective gain. The results are shown in fig.6.5. The measurements in Ar/CO_2 (70/30) from [49], performed with a ^{222}Rn source, are also shown. Considering

the slightly different HV settings and the different ambient conditions (pressure, temperature, oxygen and water content), the agreement is rather good. For the other gases, no previous measurements were published. In fig.6.6 the measurements in neon-based gas mixtures are shown.

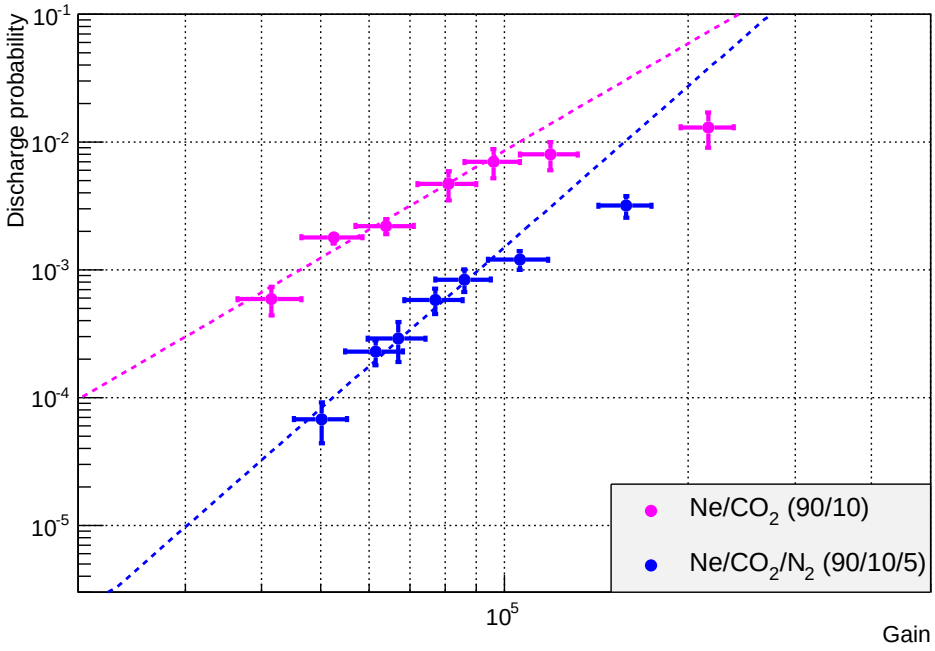

Fig. 6.6: Discharge probability as a function of gain in neon-based gas mixtures, with "standard" HV settings.

The results clearly show a consistent effect, of order of magnitudes, that small fractions of quenching gases (CO_2, N_2) introduce in terms of discharge probability. Considering the same effective gain, i.e. same charge flowing across the GEMS, neither the differences in primary ionization or diffusion, which reduces the charge density at the GEM-holes, are enough to explain the differences observed. The results suggest that other mechanisms may play a bigger role in discharge formation, for example absorption of photons from atomic de-excitation or electronic capture (photon feedback suppression), for which quenchers are thought for (see sec.2.5). It also seems that the curves roughly follow a power-law dependence (straight lines in log-log scale), of the form:

$$P_{\mathrm{d}}(g) \approx a\, g^{b}\,, \tag{6.1}$$

where a and b are set by the gas proprieties. The dotted lines in fig.6.5 and 6.6 are results of fit with this function. The values of the slope parameter b of the different fits are reported in tab.6.1.

gas mixture	slope parameter b
Ar/CO_2 (70/30)	10.5 ± 0.6
Ar/CO_2 (90/10)	9.8 ± 0.4
$Ne/CO_2/N_2$ (90/10/5)	4.1 ± 0.6
Ne/CO_2 (90/10)	2.8 ± 0.5

Table 6.1: Slope parameters for different gas mixtures, "standard" HV settings.

The slope is similar between mixtures with same noble gas, even in the case of the neon, where a different quencher is added. This suggests that it is mainly set by the noble gas, i.e. by the primary ionization density, while the fraction of quenching gas only introduces an offset. A deviation from this behaviour is observed above $g > 10^5$. The effective gain was measured with a low-energy ^{55}Fe γ-source, which induce $\sim 10^3$ times less ionization electrons than the α-particles; for the latter, at this high gains, the detector is being operated close to the Raether limit, where deviations from the proportionality in the amplification of the GEMs have been observed [62] [63]. The main mechanism involved is thought to be the space charge effect in the GEM-holes, that locally reduces the electric field [64]; the smaller effective gain in the case of the α-particles could then explain the measurements. Because of the low rate of the ^{222}Rn source, it could not be used to measure the gain, and thus confirm this interpretation.

6.3 Charge density simulations

As the measurements showed, the discharge formation is certainly connected to the proprieties of the quenching gases, which are rather complex to simulate, but also on the local charge density on the GEM-foils, which on the contrary can be computed from the energy deposition in the drift volume. A detailed simulation of the experimental set-up has been developed to study this effect. We used Geant4 [53], with a *physics list* - set of simulated interaction processes and relative cross-sections - dedicated to low-energy electromagnetic interactions (G4EmLivermore), which are responsible for the ionization of the gas molecules. The charge density mainly depends on the energy loss dE/dx of the α particles along their tracks; this is described by the well-know Bethe-Bloch formula:

$$\frac{dE}{dx} = \frac{4\pi n e^4}{mc^2\beta^2} Z^2 \left(\log \frac{2mc^2\beta^2\gamma^2}{I} - \beta^2 \right) , \tag{6.2}$$

where mc^2 is the rest energy of the electron, Z the charge of the travelling particle, n the electron density and I the mean excitation energy of the atoms of the medium. This formula is derived considering every possible event that can contribute to energy loss in the medium; this includes those scattering events with high-energy transfers, that result in the creation of a high-energy electron (δ-ray). These do not really contribute to the

energy deposition along the track, as they will be stopped within a range bigger than the typical spatial resolution of the detector. The introduction of an effective cut-off in the maximum possible energy transfer (up to 250 keV, for instance, in argon-based mixtures [26]), leads to the so-called *restricted* Bethe-Block formula, which has been found to successfully describe the ionization density in gas detectors [26] [25].

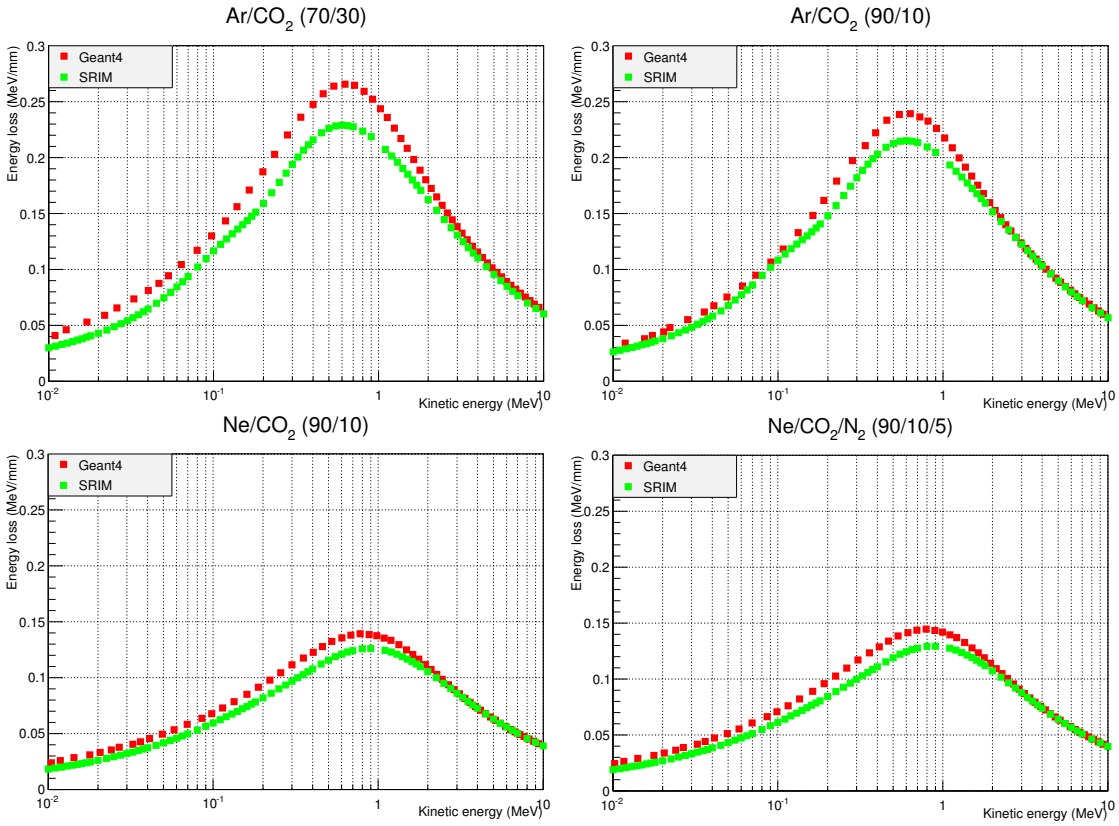

Fig. 6.7: Straggling function of α-particles in different gases, comparing Genant4 and SRIM predictions.

In Geant4, the energy loss is calculated on an *event-per-event* basis and the cut-off is set by the minimum energy that secondary particles need to have to generate independent tracks. For the purposes of this work, it was important to validate the predictions of Geant4 with an existing reference. A dedicated Monte-Carlo code for heavy-ions, Stopping and Range of Ions in Matter (SRIM) [65], was used, as it last version available (SRIM-2013). This latter only computes the *total* energy loss of ions, so no cuts were used with Geant4, for the above-mentioned reasons. The most meaningful quantities to compare are the *straggling functions*, energy loss dE/dx as a function of the particle energy: an overall compatibility, within $\sim$ 10%, was found for all the gas used (see fig.6.7).

In fig.6.8 the predicted *Bragg curves* - energy loss (dE/dx) as a function of the track

length - for 5.489 MeV α-particles in the different gases are shown. Since the dimensions of the detector (drift volume: $2.5 \times 10 \times 10$ cm^2) are comparable to the typical track lengths, different acceptances and total energy depositions are expected in the different gases, considering that the ^{222}Rn atoms are homogeneously diffused in the gas and the direction of the α-particles from their decay is isotropic. The biggest difference comes from the different densities of the gases, to which the energy loss is directly proportional: at 21.1 °C and 1 atm, argon density is 1.65 mg/cm^3 and neon one 0.84 mg/cm^3.

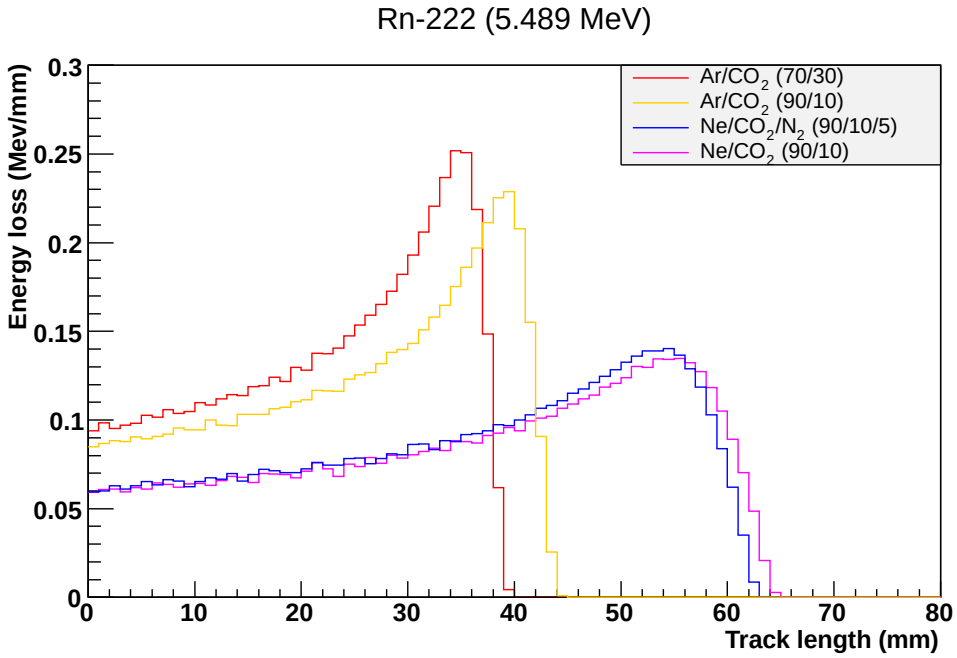

Fig. 6.8: Bragg curves of 5.489 MeV α-particles, for different gases.

The following parts of the detector set-up were included in the simulation: cathode, drift volume, GEM-stack, gas between the GEMs. The primary ionization is not calculated on a *collision-by-collision* basis, but is extracted from the energy deposition at each *step* of the tracks. The *average* number of electrons $\langle n \rangle$ ionized along each step length Δx_i, knowing the effective ionization potential of each gas W, is:

$$\langle n \rangle = \frac{(\Delta E / \Delta x)_i}{W} \, . \tag{6.3}$$

To simulate the fluctuations in the ionization density due to different collision dynamics, the *real* number n is sampled according to a gamma distribution with mean value $\mu = \langle n \rangle$ and dispersion $k = \langle n \rangle / \nu$, where ν is the Fano factor:

$$P(n) = \frac{x^{k-1} \, e^{-xk/\mu}}{(\mu/k)^k \, \Gamma(k)} \, . \tag{6.4}$$

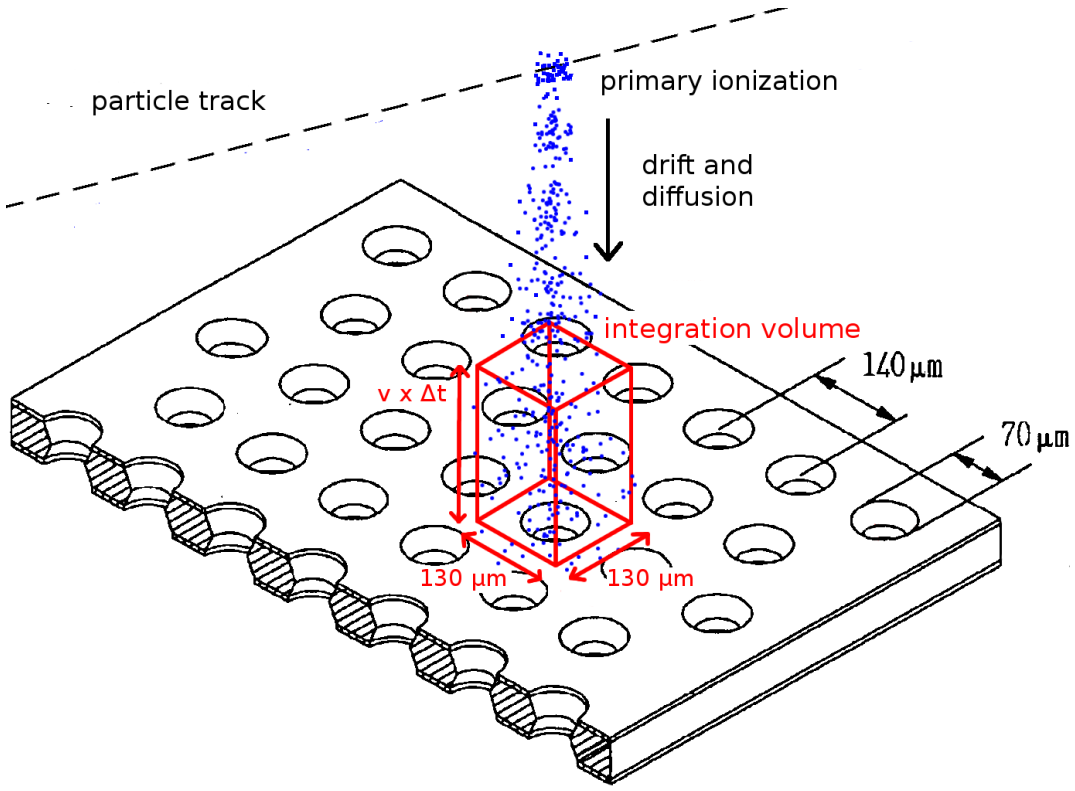

Fig. 6.9: Artistic view of the GEM-hole charge density computation: the number of primary electrons after simulating drift and diffusion is integrated in volumes of $130 \times 130 \times (v_{\mathrm{d}}\,\Delta t)$ μm^3 (see text).

No measurements of the Fano factor of the different gas mixtures used were performed. We therefore used the value measured with 5.3 MeV α particles in pure argon: $\nu = 0.2$ [66].

The position of the ionization electrons is randomly distributed along the step length. Since the electrons undergo diffusion (both transverse and longitudinal), according to their distance from the GEMs, before being amplified, this is simulated with a random shift in their position according to a Gaussian distribution of width $\sigma_{x,y} = D_{\mathrm{T}}\sqrt{\Delta z}$, $\sigma_z = D_{\mathrm{L}}\sqrt{\Delta z}$. The diffusion coefficients, for the different gases, are computed with a dedicated simulation (see sec.6.5). Of course, not all the electrons arriving on a GEM-hole after one event sum up in the avalanche, as they are amplified in different instants. Assuming a typical time scale of an amplification event - including drift across 3 GEMs and collection - of $\Delta t \approx 100$ ns, the integration along the z-axis (perpendicular to the GEMs) is performed in steps of $\Delta z = v_{\mathrm{d}}\,\Delta t$, where the drift velocity v_{d} depends on the gas. The gas proprieties used in this simulations, as calculated by a dedicated Magboltz [67] simulation (see sec.6.5), are reported in tab.6.5. For the sake of simplicity, the geometric shape of the GEM-holes area in the simulation does not reproduce the real

honeycomb structure, but is a square surface of equivalent area (~ 130 μm side).

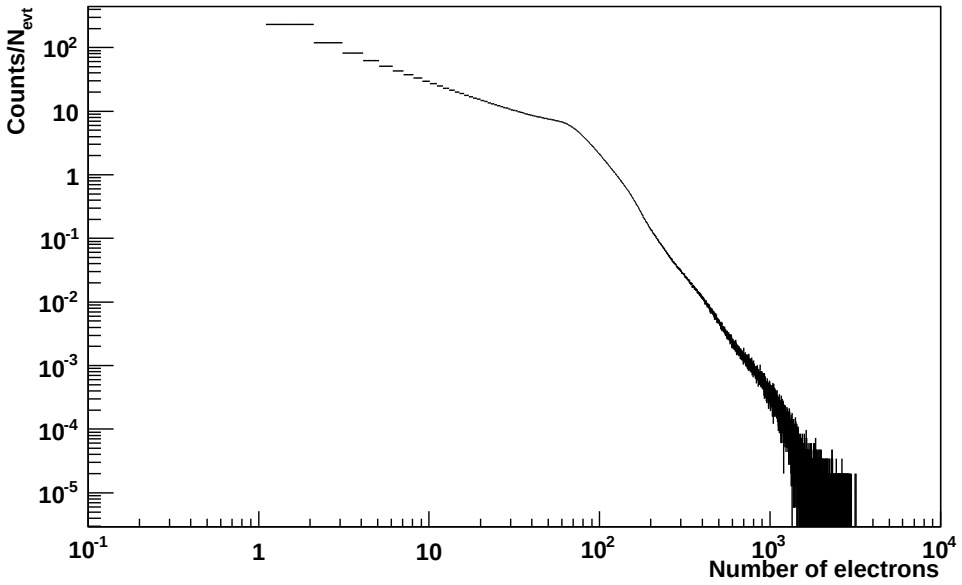

Fig. 6.10: GEM-hole charge density distribution (see text) in Ar/CO_2 (90/10), normalized on the number of events.

An artistic view visualizing the procedure is shown in fig.6.9. A typical *GEM-hole charge density distribution* $\rho(n)$ - number of electrons per unit volume, as defined before - computed from a simulation is shown in fig.6.10. To translate the computed charge density in terms of discharge probability, some assumptions need to be done: first of all, that the formation of a spark is due *only* by the local concentration of charge. The discharge probability $P_{\rm d}$ is then the probability *per event* to exceed a critical charge density $\rho_{\rm crit}$ in one GEM-hole:

$$P_{\rm d} = \int_{\rho_{\rm crit}}^{\infty} \rho(n)\, dn \ . \tag{6.5}$$

The primary ionization critical density is clearly proportional to the Raether limit, but is also affected by all the other processes that distribute, subtract or add charge inside the detector and have not been simulated: attachment, Penning effect, collection efficiency on GEM1, etc. In the following, they will be implicitly included them in the definition of the *effective* Raether limit $RL_{\rm eff}$, i.e. the primary charge deposited in the volume above a GEM-hole that eventually leads to a discharge. Since $\rho(n)$ does not include the gain g of the detector, it also has to be taken into account: increasing the amplification, one obtains an equal number of electrons in the GEM-holes from less primaries. The critical density is thus:

$$\rho_{\rm crit} = \frac{RL_{\rm eff}}{g} \ . \tag{6.6}$$

The gain fluctuations expected in the amplification stages are not simulated. Other possible effects connected to the GEM proprieties are also neglected. Since $\rho_{\text{crit}}(g)$, integrating the GEM-hole charge density distribution as in eq.6.5, we obtain the discharge probability as a function of gain, $P_{\text{d}}(g)$. The only free parameter which is tuned to match the measurements is RL_{eff}, which corresponds to the horizontal offset of the $P_{\text{d}}(g)$ curves. The results are shown in fig.6.11 and 6.12, respectively for argon- and neon-based mixtures.

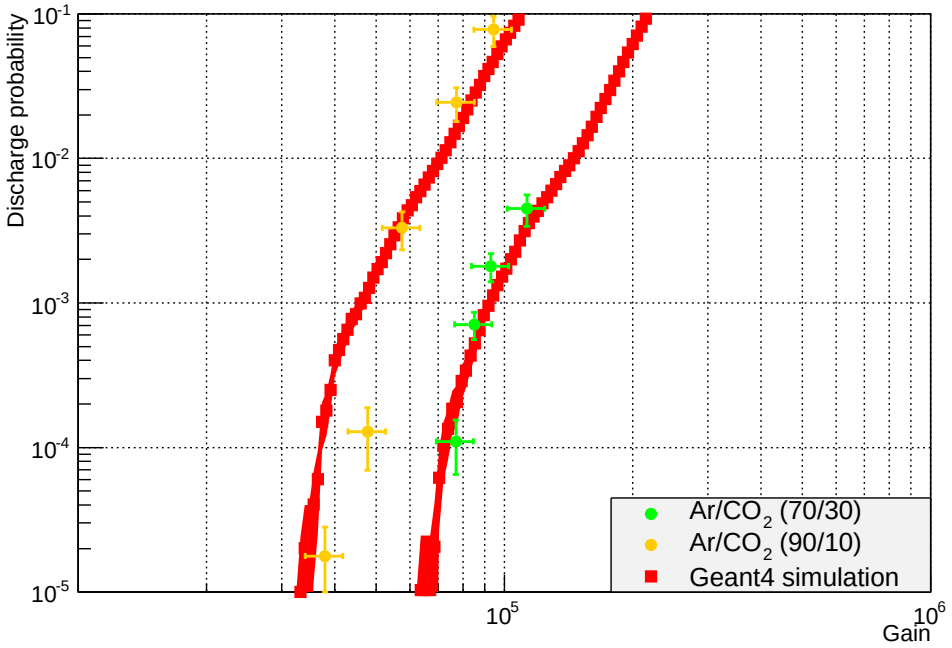

Fig. 6.11: Predicted $P_{\text{d}}(g)$ curves from Geant4 simulations, compared to measurements, in argon-based mixtures.

An overall agreement is found between simulations and measurements. The most remarkable deviation is observed in neon-based mixtures at high gains. This could be explained as well with the saturation of the effective gain, as described in sec.6.2. The absolute values of RL_{eff} that best match the measurements are reported in tab.6.2. The effects of the quenching gases translate, in this model, in a difference of the maximum charge sustainable, quantified in terms of RL_{eff}. The model successfully explains the power-law dependence of $P_{\text{d}}(g)$ with the similar behaviour of the GEM-hole charge density distribution, that is observed for high-charge density events ($n > 100$) in the simulations (see fig.6.10):

$$\rho(n) \propto n^{-b} \Rightarrow P_{\text{d}} = \int_{\rho_{\text{crit}}}^{\infty} \rho(n) dn \propto \frac{1}{b-1} \left(\frac{g}{RL_{\text{eff}}} \right)^{b-1} \propto g^{b} \, . \tag{6.7}$$

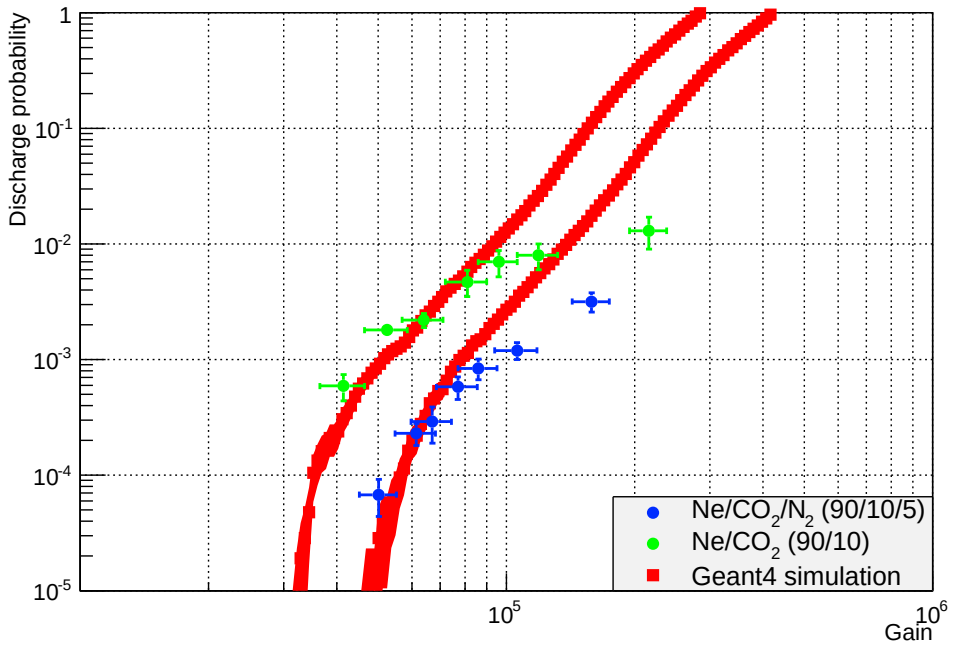

Fig. 6.12: Predicted $P_{\mathrm{d}}(g)$ curves from Geant4 simulations, compared to measurements, in neon-based mixtures.

The differences in the slopes of argon- and neon-based mixtures can then be explained in terms of the different energy deposition scenarios. In argon, which is denser, there is a higher probability that tracks are fully contained in the drift volume, with a higher average dE/dx: the steep $P_{\mathrm{d}}(g)$ curve reflects the statistics of the ionization distribution in the gas. In neon, on the contrary, the average charge density in the drift volume is smaller, but more particles end up on the GEMs, resulting in a high charge density close to the GEM-holes, where diffusion does not contribute: the combination of the two results in a flatter curve.

gas mixture	$RL_{\mathbf{eff}}$
$\mathrm{Ar/CO_2}$ (70/30)	2.80×10^8
$\mathrm{Ar/CO_2}$ (90/10)	1.05×10^8
$\mathrm{Ne/CO_2}$ (90/10)	6.40×10^7
$\mathrm{Ne/CO_2/N_2}$ (90/10/5)	1.00×10^8

Table 6.2: Effective Raether limits for different gas mixtures.

Because of the different approximations that have been used in this model, it is not possible to state anything definitive concerning the *real* Raether limits of the detector in the different gas mixtures. Care must also be taken when directly extrapolating these

results, in terms of charge densities, to different scenarios: because of the steepness of the $P_{\mathrm{d}}(g)$ curves, small systematic errors in the computation of the charge can translate into a big offset of the predicted discharge probability. In particular, a realistic description of the ionization distribution along a track and of the gain fluctuations in the detector is required to confirm these predictions. Also the interaction of the particles with the GEM-foils, which could have an influence, needs to be better understood, including a precise microscopic modelling of the electrons extracted into the gas and the resulting charge densities.

However, the overall agreement between simulations and measurements shows that the discharge probability is strongly correlated with the GEM-hole primary charge density, and suggests that - at least with the "standard" HV settings used in these measurements - it is indeed the *crucial* parameter for the determination of the dependency of the discharge probability on the gain. These results give as well confidence that a meaningful estimation of GEM detectors stability can be performed in different scenarios, including the LHC one, using the simple model proposed and the values of RL_{eff} hereby reported. It is worth to note that a similar approach has been previously adopted [68] in a stability study with Micromegas detectors. Different assumptions were made in the simulations and the scenario was different as well (15 GeV π^+ beam-source): nevertheless, the basic idea, that discharges happen when locally - in the sense of the area were the amplification takes place - exceeding a certain charge density critical value, was the same. The results were consistent with the measurements, as in this work.

Another interesting result of the simulations is that the ratios of the different RL_{eff} allow to estimate the effects of the different gas components. Possible systematic errors introduced by the approximations in the computation of the GEM-hole charge density are expected to cancel out. Indeed already a small fraction of nitrogen (4.8%) increases the maximum charge sustainable by a factor:

$$RL_{\mathrm{eff}}^{\mathrm{Ne/CO_2/N_2\ (90/10/5)}} / RL_{\mathrm{eff}}^{\mathrm{Ne/CO_2\ (90/10)}} \approx 1.56\ . \tag{6.8}$$

On the other hand the different fraction of carbon dioxide (CO_2) in argon-based mixtures, from 10% to 30%, translates into:

$$RL_{\mathrm{eff}}^{\mathrm{Ar/CO_2\ (70/30)}} / RL_{\mathrm{eff}}^{\mathrm{Ar/CO_2\ (90/10)}} \approx 2.67\ . \tag{6.9}$$

These numbers confirm the observations made in sec.6.2: the quenching gases strongly affect the maximum charge sustainable by a GEM before electrical breakdown. This in turn suggests that the photon feedback mechanism play a major role in the formation of propagating streamers in GEM detectors. Finally, it is possible to compare the two noble gases with an equal fraction of quenching gas:

$$RL_{\mathrm{eff}}^{\mathrm{Ar/CO_2\ (90/10)}} / RL_{\mathrm{eff}}^{\mathrm{Ne/CO_2\ (90/10)}} \approx 1.64\ . \tag{6.10}$$

Even if this result does not allow to derive general conclusions, it indicates that argon can sustain higher charge densities than neon before the appearance of discharges. However,

since argon is denser and has a lower ionization potential than neon, the average primary charge density is also higher, which means that it would not necessarily be more stable in practical applications.

6.4 HV settings effects

The effects of different HV settings on the discharge probability were studied as well, in the gas mixture $Ne/CO_2/N_2$ (90/10/5). As previously said, there are two main differences between the "standard" and "ion back-flow" settings, respectively optimized for stability and ion back-flow suppression:

- the order of amplification, set by the voltage applied on GEMs,
- the low transfer field above GEM3 (E_{t2}).

To disentangle the contribution of these two parameters to discharge formations, a series of measurements with intermediate settings ("reversed" and "low-E_{t2}") was carried out. The specifications of the different HV settings at gain 2000 are reported in tab.6.3.

	standard	**IBF**	**reversed**	**low-E_{t2}**
ΔUGEM1 (V)	284	227	213	318
E_{t1} (kV/cm)	2.6	3.0	2.6	3.0
ΔUGEM2 (V)	260	278	260	278
E_{t2} (kV/cm)	2.6	0.1	2.6	0.1
ΔUGEM3 (V)	227	318	298	227
E_{ind} (kV/cm)	2.6	3.0	2.6	3.0

Table 6.3: Different triple-GEM HV settings, gain 2000 in $Ne/CO_2/N_2$ (90/10/5).

The results are shown in fig.6.13. Both amplification order and low transfer field have a considerable effect on stability, that translates into a difference of more than one order of magnitude, for a fixed effective gain, of the discharge probability, which sum up to the "IBF" HV settings values. These measurements shows that the voltages and the electric fields in the GEMs can actually be much more crucial for stability than the choice of the gas mixture. The gas choice fixes the total primary charge density on the GEMs, which cannot then explain the differences observed. What is indeed connected to the HV configuration, and can differ even at a fixed effective gain, is the *real* charge flowing through the GEM-holes. This depends on the collection and extraction efficiencies of each GEM, which in turn are set by the electric fields and the ΔUGEMs. Moreover, the charge sharing among different GEM-holes on GEM2 and GEM3, which reduces the

GEM-hole charge density, can also be affected by the HV settings. These effects will be extensively studied in sec.6.5 and will partially explain these measurements.

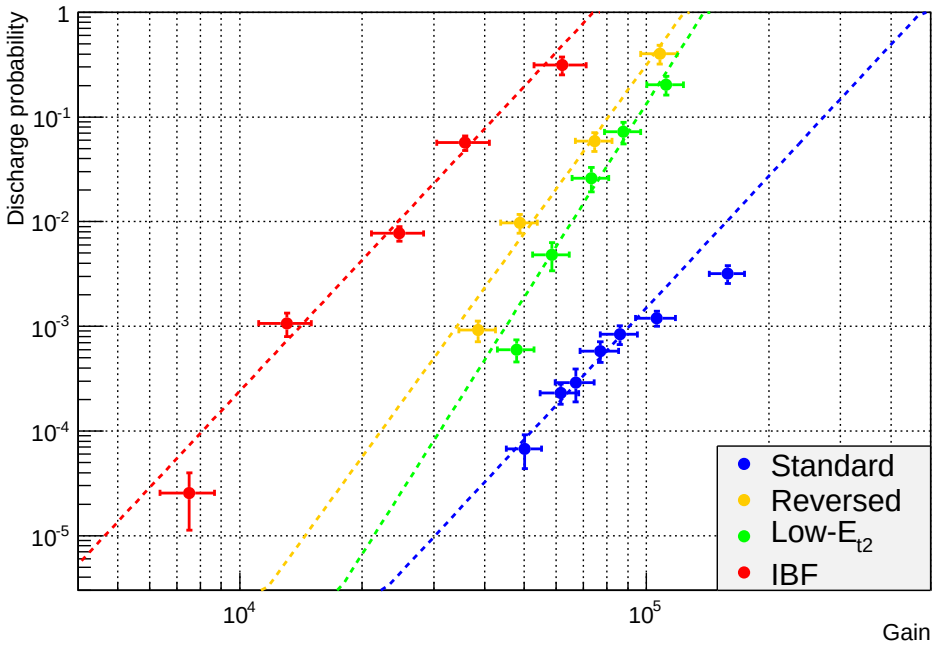

Fig. 6.13: Discharge probability in $Ne/CO_2/N_2$ (90/10/5), with different HV settings (see tab.6.3). The dotted lines are fits with eq.6.1.

One also observes a variation in the slope b of the $P_d(g) \propto g^b$ curves (see tab.6.4) in the "reversed" and "low-E_{t2}" settings. This effect could come from the different scaling of the absolute voltages ($\Delta UGEM$) and the fields. In fact, using a voltage divider as a powering scheme, to increase the total gain of the detector one increases the total potential supplied and this is distributed according to the resistors to every electrode. The effects responsible for the higher discharge probability can have a dependence on the absolute voltages on each GEM and the fields which needs to be disentangled from the measurements at different effective gains.

HV settings	**slope parameter** b
standard	4.2 ± 0.6
reversed	5.4 ± 0.6
low-E_{t2}	6.1 ± 0.7
IBF	4.2 ± 0.5

Table 6.4: Slope parameters for different HV settings, in $Ne/CO_2/N_2$ (90/10/5).

The effect of the order of amplification has been further studied, measuring the discharge probability for other two settings, with amplification order between "standard" and "reversed". Fig.6.14 shows the differences at equal gains, as a function of the amplification order:

$$\frac{\Delta U\text{GEM3} - \Delta U\text{GEM1}}{\Delta U\text{GEM2}} \,. \tag{6.11}$$

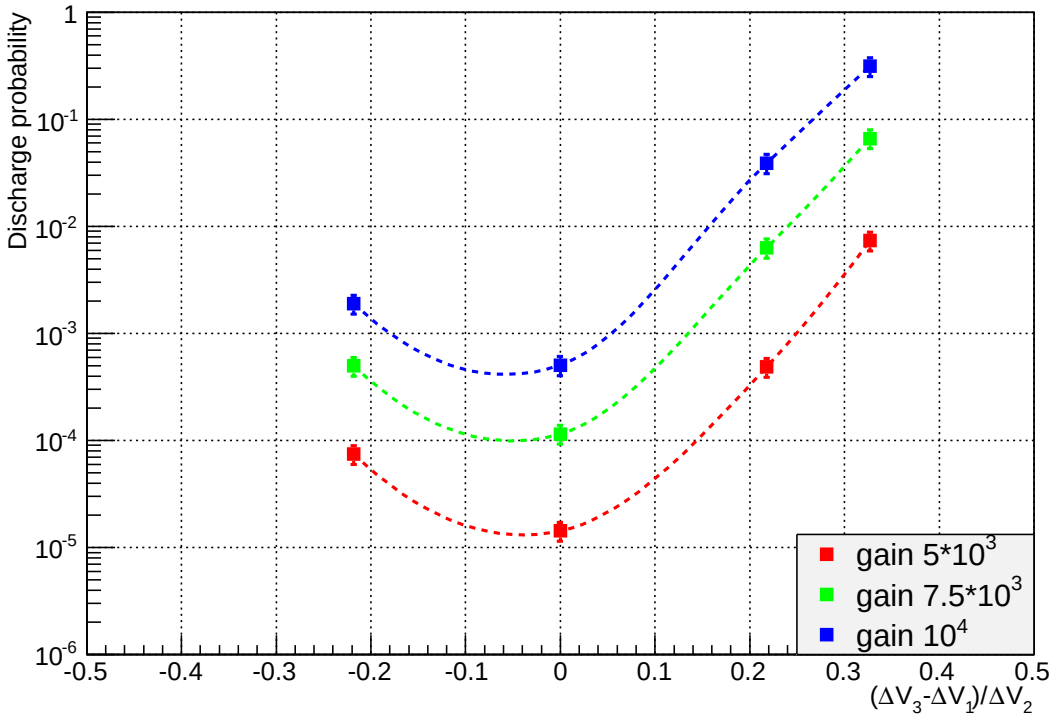

Fig. 6.14: Discharge probability at fixed gains for different amplification order among GEMs (see text). The first point on the left corresponds to "standard" HV settings, the last one on the right to "reversed" ones.

The most stable configuration that was found is the one with equal amplification among the three GEMs; it thus seems that the maximum ΔUGEM, which is the lowest in the latter case, does have an influence as well in discharge probability. As expected, on the contrary, there is a different increase in discharge probability according to the order of amplification, seen by the asymmetric shape of the curve of fig.6.14. In conclusion, the results show that the discharge probability, at a fixed primary charge density, strongly depends on the order of amplification and suggest that the maximum $\Delta UGEM$ in the GEM-stack may influence it as well.

6.5 GEM simulations

To understand the influence of the HV settings on the discharge probability, a detailed simulation of a GEM detector was performed. The electrostatic potentials in the GEM-holes were calculated with ANSYS [69] and using Garfield++ [70] the transport and the amplification of the electrons in the gas was simulated.

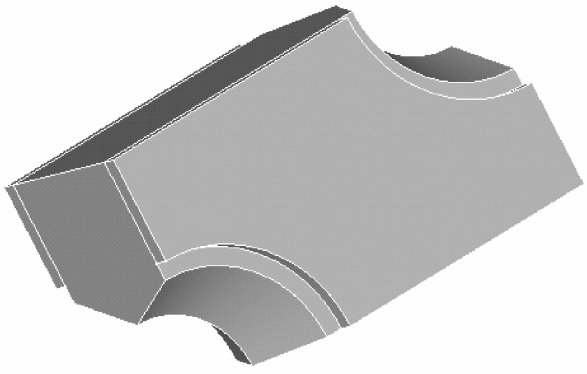

Fig. 6.15: Unit cell of a GEM-foil, used to calculate the electric potentials with ANSYS.

ASNYS is an engineering simulation software based on Finite Element Method (FEM). First, the geometry of the system (in our case, of a GEM-hole), is defined in a 3D Computer-aided design (CAD) system; to calculate the potential in the gas volume, the latter is divided into a grid of *elements*, defined by the position of the *nodes* at their edges. The FEM algorithm works in the following way: after having fixed the boundary conditions and the surfaces of the volume, it starts to calculate an approximate solution on the nodes of the external elements. The calculation is continued on the neighbouring elements, which share some nodes on which the solution is known, until the potential on every volume's node is computed. A comprehensive introduction to the topic can be found in [71]. The volume of the elements of the grid (*mesh*) is not fixed, but varies according to the expected gradient of the fields, to have a finer calculation where needed; the meshing procedure is automatically performed by ANSYS. Initial conditions at the surface boundaries (voltages of the different electrodes), as well as material proprieties, need to be set by hand. The potentials are then calculated on a *cell unit* of the form shown in fig.6.15, which is then mirrored by Garfield++ along an orthogonal $x-y$ basis to recreate the GEM-foil.

Garfield calculates the electric field at each node of the mesh, from the potential map provided by ANSYS. It then computes the electrons/ions tracks using Magboltz [67], to which is automatically interfaced. Magboltz is a computational algorithm, based on Monte-Carlo integration, to solve the Boltzmann transport equations of electrons

distribution $f(\vec{x}, \vec{v}, t)$ in gas mixtures:

$$\frac{\partial f}{\partial t} + \vec{v} \cdot \vec{\Delta} f + \frac{e\vec{E}}{m} \frac{\partial f}{\partial \vec{v}} = \left(\frac{\partial f}{\partial t} \right)_{\text{coll}} , \tag{6.12}$$

where q,m and $\vec{v}$ are respectively charge, mass and velocity of the electrons, while $\vec{E}$ is the electric field. The last term $(\partial f/\partial t)_{\text{coll}}$ takes into account the different possible collisions with the gas molecules and the relative cross-sections. With Magboltz one can then extract the gas proprieties which are crucial for gas detector simulations: diffusion, drift velocity, attachment. The values used in sec.6.3 have been calculated in a dedicated simulation; they are reported in tab.6.5.

gas mixture	$v_{\mathbf{d}}$ (mm/μs)	$D_{\mathbf{T}}$ (μm/$\sqrt{\text{cm}}$)	$D_{\mathbf{L}}$ (μm/$\sqrt{\text{cm}}$)
Ar/CO_2 (70/30)	9.31	135	137
Ar/CO_2 (90/10)	33.55	246	275
Ne/CO_2 (90/10)	25.32	215	214
$Ne/CO_2/N_2$ (90/10/5)	26.61	223	232

Table 6.5: Electron drift velocity, transverse and longitudinal diffusion of different gases, calculated with Magboltz.

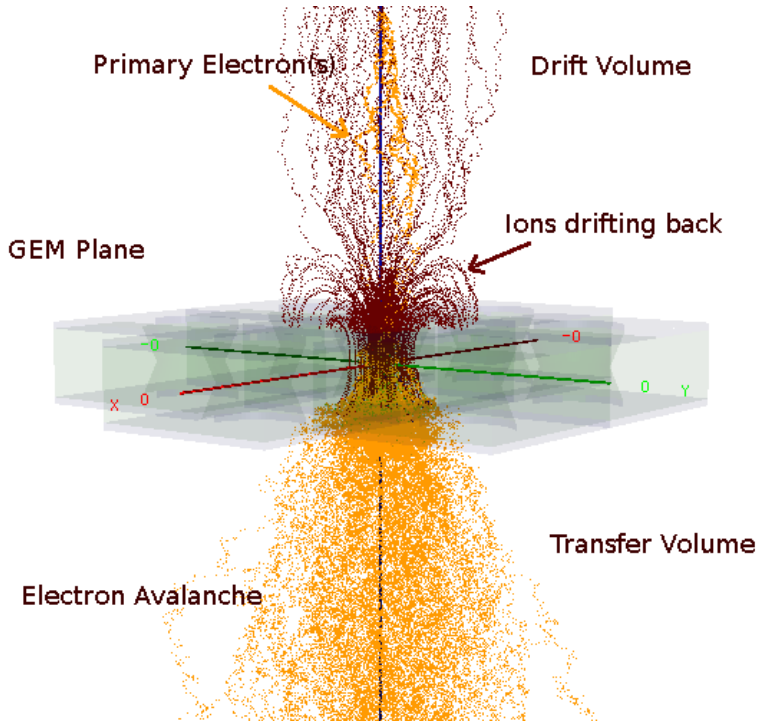

Fig. 6.16: Amplification a GEM-hole, as simulated by Garfield++.

An interface to ROOT (Garfroot) allows to store all the informations in a dedicated ROOT file. The amplification (gain) in the GEM-hole is calculated from the Townsend coefficients of the gas components and the fields applied, using again Magboltz. The final simulation of several events - incoming primary electron and subsequent amplification - is shown in fig.6.16.

The values of the gas proprieties used in the simulations of sec.6.3 were calculated with Magboltz assuming a drift field of 400 V/cm and no magnetic field; they are summarized in tab.6.5. The idea is then to study the dependency of some key proprieties of the GEMs (absolute gain, collection and extraction efficiency, charge sharing among different GEM-holes) on the HV settings and correlate this to the expected charge densities in the GEM-holes. However, due to the high computational requirements, only single GEMs were simulated. To connect the results of the simulations with the measurements some assumptions are needed:

- The crucial quantity connected to discharges is the GEM-hole charge density, in particular at the last amplification stage (GEM3), where the highest number of electrons is reached.
- Other mechanisms potentially responsible for discharges can be neglected - for instance, the extraction of secondary electrons from the copper layer where the ions are collected.
- It is possible to estimate the differences between HV settings simulating only the single stages in which they differ, not the full GEM-stack.

The first objective was to explain the influence that the low transfer field E_{t2} has on discharge probability. We thus compare HV settings with same order of amplification among GEMs, E_{t1} and E_{ind}. On GEM2, the low E_{t2} reduces the extraction efficiency, resulting in more electrons collected on the bottom electrode. This has to be compensated with higher absolute voltages $\Delta U\text{GEM}s$, thus higher gains, as it is experimentally observed. This was indeed confirmed by simulations: at a fixed ΔUGEM the extraction efficiency linearly drops with the electric field (fig.6.17), as well as the effective gain. The differences in the effective gain between argon- and neon-based mixtures come from the different Townsend coefficients. As it was observed in sec.6.4, the absolute voltages may play a role in terms of discharge probability: the higher ΔUGEMs needed already point towards the differences observed in the measurements.

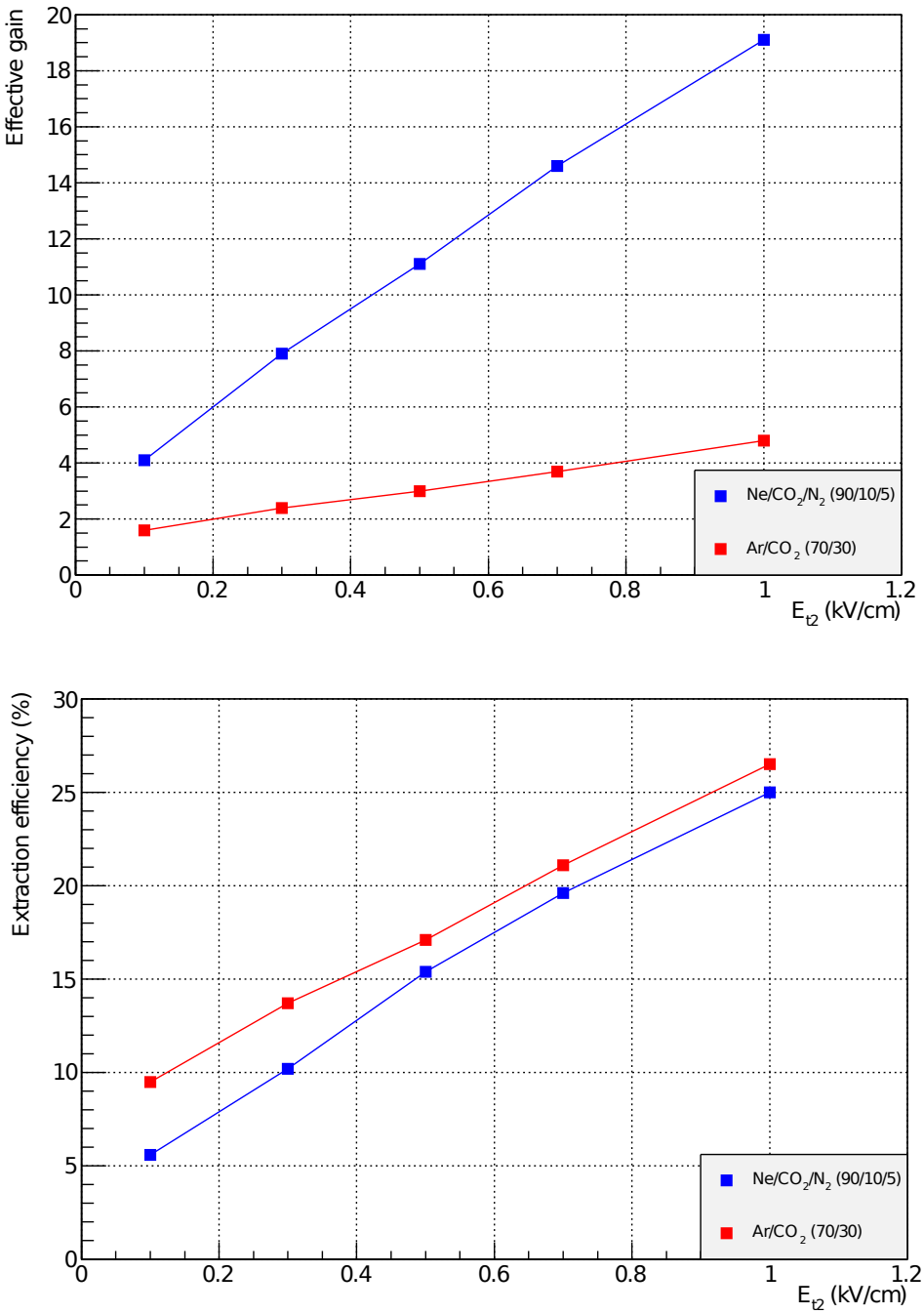

Fig. 6.17: Effective gain (up) and extraction efficiency (down) as a function of the electric field below the GEM (E_{t2}). Field above the GEM 3.0 kV/cm, ΔUGEM = 360 V. The differences in the effective gain between argon- and neon-based mixtures come from the different Townsend coefficients.

We have however assumed that the stage responsible for discharges is GEM3, where the highest charge densities are reached. At this stage, for a fixed effective gain, no major difference is expected in the total charge produced. The extraction efficiency is mainly set by the the induction field, below GEM3, which is constant. The low field above (E_{t2}) is expected to increase the collection efficiency, which partially compensate the loss on GEM2, together with the slightly higher ΔUGEM3.

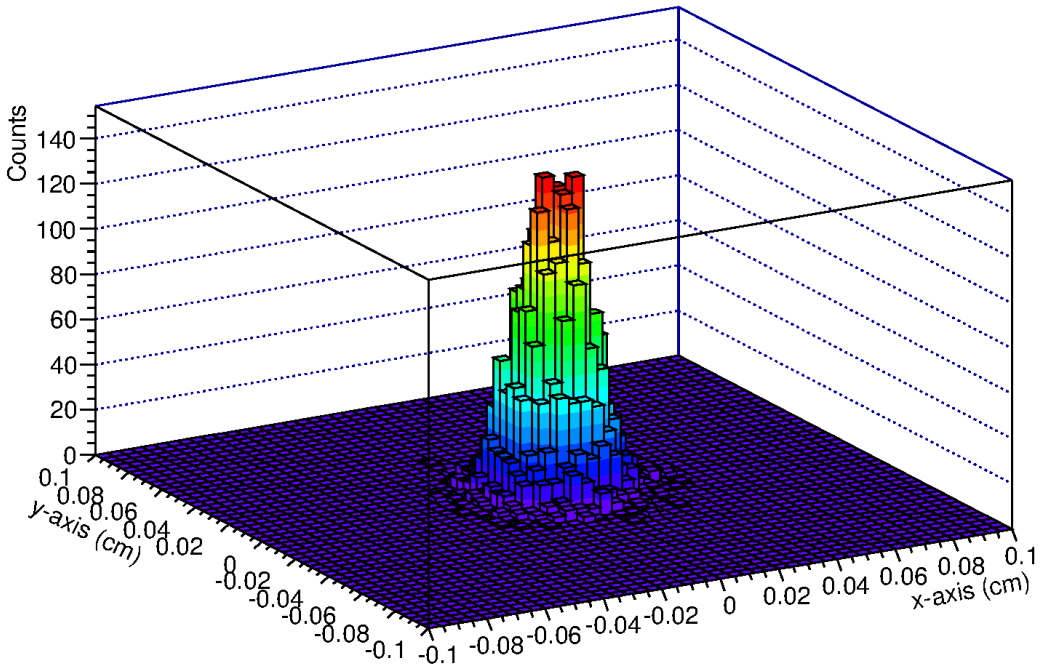

Fig. 6.18: Electrons position after $\Delta z = 1.8$ mm drift; the GEM-hole is centred in (x,y) = (0,0).

The differences in discharge probability can be explained in terms of the charge sharing among different GEM-holes on GEM3, which determines the maximum GEM-hole charge density for a fixed gain. In fact, what is also correlated with the low E_{t2} is the variation in the lateral distribution of the electrons $\rho(x, y)$ inside an avalanche produced on GEM2. Fig.6.18 shows the typical shape of such a distribution, after the $\Delta z = 1.8$ mm drift that separates two GEM-foils. There are two effects involved in the spreading of the electrons. From one side there's the transverse diffusion, which depends both on the gas and the transfer field. The electric field at the exit of the GEM-hole, on the other side, can be strong enough to pull the electrons and distribute them along the size of the pitch (140 μm). Simulations showed (fig.6.19) that these two mechanisms have actually an opposite dependence on the strength of the transfer field, in the range of interest for GEM applications (0.1-5 kV/cm): diffusion shows a minimum at $\sim$ 0.3 kV/cm, where the spreading effect of the electric field starts to appear, and then slowly

increases. The combination of the two results into a local minimum in the region of interest for ion back-flow suppression.

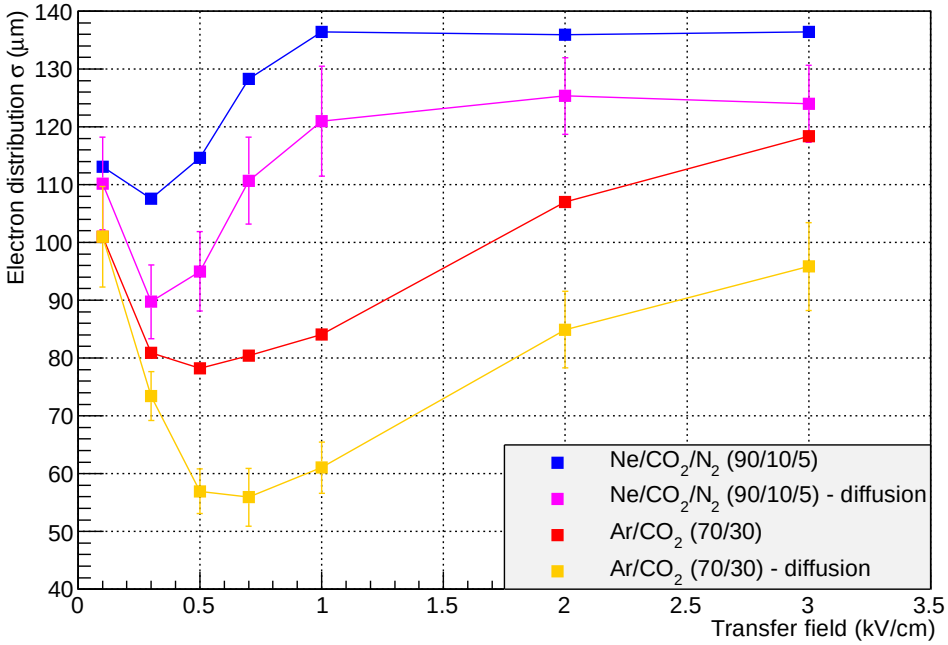

Fig. 6.19: Standard deviation σ of $\rho(x, y)$ after $\Delta z = 1.8$ mm drift, as a function of transfer field E_{t2}. The contribution of the diffusion is $D_T\sqrt{\Delta z}$. Field above the GEM 3.0 kV/cm, ΔUGEM = 360 V.

Following the line of reasoning exposed in sec.6.3, if the discharge probability scales with the charge density, and since it shows such a steep dependence on the gain, small differences in charge sharing among GEM-holes can lead to very different stability scenarios. For the sake of simplicity, let's assume a GEM-hole collects all the electrons on a circular area of radius $R = 70$ μm, the pitch being 140 μm; the maximum fraction of electron collected from an avalanche $Q_{\max}$, in case of perfect alignment of the upper and lower GEM-hole, is thus the integral of the electron distribution $\rho(x, y)$ over the area $\Sigma_{\text{hole}} \approx \pi R^2$:

$$Q_{\max} = \int\int_{\Sigma_{\text{hole}}} \rho(x, y)\, dx\, dy = \int\int_{\Sigma_{\text{hole}}} e^{-\frac{x^2+y^2}{2\sigma^2}} \,. \tag{6.13}$$

To simplify the calculation, it is possible to exploit the symmetry of the system: the 2-dim gaussian $\rho(x, y)$ is a *solid of revolution*, built from rotating one half of a 1-dim gaussian $z = \rho(x) = e^{-x^2/(2\sigma^2)}$ around the z-axis. Knowing the area of the disk contained

in the gaussian $A(x) = \pi(\rho^{-1}(z))^2 = \pi 2\sigma^2 |\log(x)|$, the integral reduces to:

$$Q_{\max} = \rho(R)\pi R^2 + \int_{\rho(R)}^{\rho(0)} \pi 2\sigma^2 |\log(x)| \, . \tag{6.14}$$

Since σ depends on $\mathrm{E_{t2}}$, it is possible to compute $Q_{\max}(E_{\mathrm{t2}})$. In the case of $\mathrm{Ne/CO_2/N_2}$ (90/10/5), a relative difference $Q_{\max}(3.0\mathrm{kV/cm})/Q_{\max}(0.1\mathrm{kV/cm}) \approx 60\%$ is expected. Assuming that the discharge probability scales with respect to the gain roughly as $Q_{\max}$, the expected difference in gain for a fixed discharge probability is ~ 1.7. Inversely, according to eq.6.1, assuming $b \approx 5$ (averaged among different HV settings), we expect up to a factor of ~ 13 in the difference of discharge probability for a fixed gain, which is roughly consistent with our measurements (fig.6.13). Nevertheless, this effect alone does not entirely explain the results: the differences in the slope of the $P_{\mathrm{d}}(g)$ curves, for instance, still need to be properly understood. The higher absolute voltages (ΔUGEMs) needed with low transfer fields, as previously observed, may as well be connected to the discharge probability.

The other effect observed varying the HV settings concerns the order of amplification, at constant transfer/induction fields. Since the electron avalanche lateral size was observed to be rather unaffected by the voltages across the GEM, the previous argument does not hold in this case. What does change is not the charge sharing among different GEM-holes, but the total charge produced in GEM3. At each amplification stage i, the effective gain g_i is set by the absolute gain G_i and the collection/extraction efficiencies $\epsilon_{\mathrm{c}i}/\epsilon_{\mathrm{t}i}$, according to eq.3.1. For n_{p} incoming electrons, the real number of electrons N_i produced inside the GEM-holes is:

$$N_i = n_{\mathrm{p}} \, G_i \, \epsilon_{\mathrm{c}i} \, . \tag{6.15}$$

The number of electrons at GEM3 is then:

$$N_3 = g_1 \times g_2 \times G_3 \, \epsilon_{\mathrm{c}3} = G_1 \, \epsilon_{\mathrm{c}1} \, \epsilon_{\mathrm{t}1} \times G_2 \, \epsilon_{\mathrm{c}2} \, \epsilon_{\mathrm{t}2} \times G_3 \, \epsilon_{\mathrm{c}3} \, . \tag{6.16}$$

The extraction and collection efficiency depend both on ΔUGEM and on the fields above (E^{up}) and below (E^{down}) the GEM.

$$\epsilon_{\mathrm{c,t}}(\Delta U_{\mathrm{GEM}}, E^{\mathrm{up}}, E^{\mathrm{down}}) \, . \tag{6.17}$$

Let's now consider two configurations with opposite order of amplification, at a same total effective gain g_{tot}. The voltage corresponding to the maximum amplification stage ($\Delta U_{\max}$) and the minimum ($\Delta U_{\min}$) will be inversely located on the uppermost (GEM1) and lowermost (GEM3) GEM. Let's also assume, as in the configuration used in the measurements, a drift field $E_{\mathrm{d}} = 0.4$ kV/cm and all transfer/induction fields $E_{\mathrm{t}} = 3.0$ kV/cm. The ratio of the total charge on GEM3 between the "standard"-like and "reversed"-like HV settings will then be:

$$\frac{N_3^{\mathrm{rev}}}{N_3^{\mathrm{sta}}} = \frac{\epsilon_{\mathrm{c}}(\Delta U_{\min}, E_{\mathrm{d}}, E_{\mathrm{t}}) \, \epsilon_{\mathrm{t}}(\Delta U_{\min}, E_{\mathrm{d}}, E_{\mathrm{t}}) \, \epsilon_{\mathrm{c}}(\Delta U_{\max}, E_{\mathrm{t}}, E_{\mathrm{t}})}{\epsilon_{\mathrm{c}}(\Delta U_{\max}, E_{\mathrm{d}}, E_{\mathrm{t}}) \, \epsilon_{\mathrm{t}}(\Delta U_{\max}, E_{\mathrm{d}}, E_{\mathrm{t}}) \, \epsilon_{\mathrm{c}}(\Delta U_{\min}, E_{\mathrm{t}}, E_{\mathrm{t}})} \, . \tag{6.18}$$

The collection efficiency as a function of the voltage across the GEM in $Ne/CO_2/N_2$ (90/10/5) is shown in fig.6.20, for the two cases of GEM1 ($E^{up} = E_d = 0.4$ kV/cm) and GEM3 ($E^{up} = E_t = 3.0$ kV/cm). Fig.6.21 shows the extraction efficiency as a function of ΔUGEM. In this case, as expected, no difference is observed varying E^{up}. With "standard" HV settings, at an effective gain of 5×10^4 in $Ne/CO_2/N_2$ (90/10/5) - around which the measurements were performed - the voltages correspond to $\Delta U_{max} = 360$ V and $\Delta U_{min} = 280$ V. Comparing these with the settings with inverse amplification order, the biggest differences are expected in the collection efficiencies on GEM3. Assuming that the discharge probability scales with respect to the gain roughly as N_3, the expected difference in gain for a fixed discharge probability is ~ 1.3. This translates, assuming as before $b \approx 5$, into a factor of ~ 4 in the difference of discharge probability for a fixed gain.

This effect can only partially explain our measurements (fig.6.14), but is still expected to play an important role. Moreover, since the extraction/collection efficiencies depend on ΔUGEMs, it is consistent with the explanation that the slope of the $P_d(g)$ curves varies because of the different scaling of the voltages in the resistor chain. To properly interpret the measurements, it seems also important to understand the effects that the absolute ΔUGEMs have in terms of discharge formation.

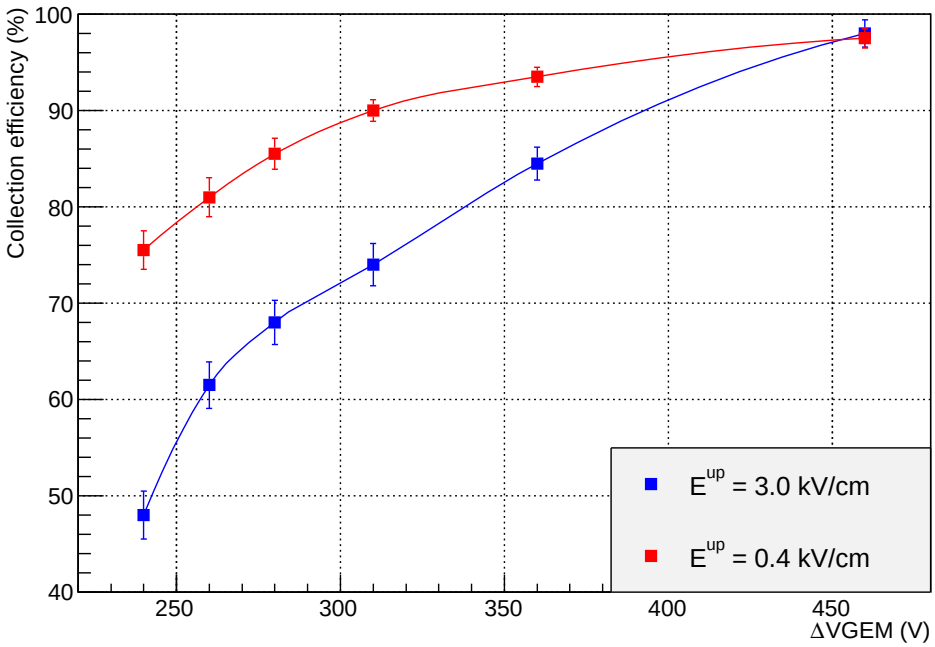

Fig. 6.20: Collection efficiency as a function of ΔUGEM. Field below the GEM 3.0 kV/cm.

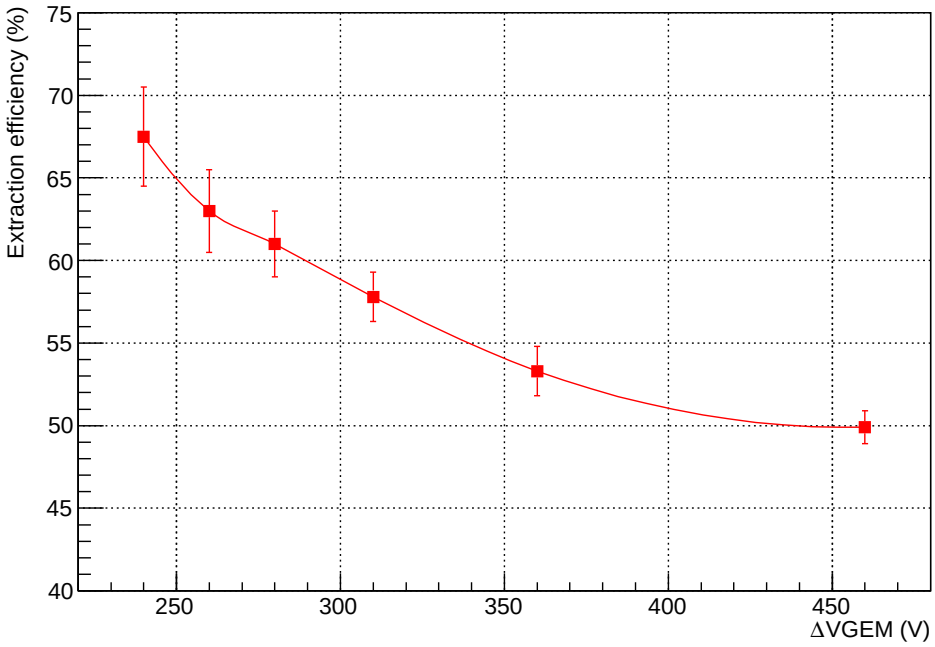

Fig. 6.21: Extraction efficiency as a function of ΔUGEM. Fields above and below the GEM 3.0 kV/cm.

Chapter 7

Conclusions & Outlook

This work presents the results of an extensive study on stability of triple-GEM detectors, carried out in the framework of the GEM upgrade of the ALICE TPC, foreseen for LHC RUN 3.

The formation of sparks is an important issue in GEM detectors, as they may lead to gain inefficiencies or even permanent failure of the GEM-foils. Because of the high-multiplicity environment of Pb-Pb collisions at LHC, which constitutes an extreme scenario of operation, a dedicated measurement of the detector's stability limits was required. A prototype of the ALICE TPC IROC has been successfully tested in a dedicated beam test with low energy protons, which allowed to set safety margins both in rate and particle rate for beam operations. Assuming that the crucial parameter responsible for discharges is the primary ionization density in the detector and, conversely, the current density flowing through the GEM-foils, the conditions foreseen for the LHC RUN 3 have been reproduced and overtaken, as shown by a detailed Geant4 simulation of the experiment. This work constituted an important step in the detector's development and gave confidence about the feasibility of the ALICE TPC GEM upgrade project. A dedicated test at the LHC will be anyway required to finally establish that the detector indeed satisfy the specific requirements of the experiment.

The problem of spark formation in GEM detectors, even if crucial in real applications, is still poorly understood. For this reason, a dedicated R&D project has been carried out, aimed to understand the effects of different detector's parameters on discharge formation and, eventually, optimize these latter in terms of stability. The gas choice was the first one to be studied. A strong dependence of the discharge probability was observed with respect to the quenching gases used in the mixture: small differences in their amounts can improve the performances of the detector by orders of magnitude. This result opens to the possibility to greatly improve GEM detectors stability already with a careful choice of the gas mixtures. Through a Geant4 simulation of the experiment, it was also possible to correlate the measurements with the primary ionization density in the detector, which is a crucial quantity concerning the formation of discharges. A new model is proposed, which is able to explain the discharge probability from the primary charge density distribution in the GEM-holes, computed by simulations. The overall agreement with the data suggests that this model can be successfully adopted to estimate the detector's stability also in different scenarios, including the LHC one.

This study also investigated the effects of the HV settings of the GEM-foils on spark

formation. The results showed that there is indeed a strong dependency both on the order of amplification across the GEM-stack and on the transfer fields between GEMs. In particular, the settings optimal for ion back-flow suppression have been observed to involve a consistent worsening of detector's stability. This in turn suggests that the proprieties of the amplification process across the GEM (absolute gain, collection and extraction efficiency, charge sharing among different GEM-holes) have a great influence on the detector's stability and need to be finely optimized. A full Garfield/Magboltz simulation of a GEM has been carried out to understand the effects of the HV settings. The dependency of different GEM proprieties on the voltages across the GEMs and the electric fields was studied. Concerning the discharge probability, different explanations are proposed, which point towards the experimental results, based again on the assumption that the charge densities in the GEM-holes is the main responsible for the occurrence of sparks.

There are still many possible causes of sparks which have not been investigated and are needed to be properly understood, to have a complete and exhaustive picture of the physics of discharges in GEM detectors. For instance, the interaction of the particles with the GEM-foils, that can lead to very high charge densities, or the effect of the absolute voltage across the GEM, which, as it was observed, might play a role. However, this work indicates different methods to measure, estimate and improve the stability against discharges and thus provides important observations for the future of GEM detectors development.

Acknowledgments

First of all, I would like to thank Piotr Gasik, for his constant support and advise. He truly constituted for me an example of scientific rigour and dedication to experimental research. Without him, I would have never been able to complete my work. I deeply thank also Laura Fabbietti, for her outstanding motivational spirit and the brilliant input she provided. I thank Markus Ball and Bernhard Ketzer, their vast knowledge of GEM detectors was of great help throughout all my work. I thank all the people who gave a hand for the IROC test at the MLL: Andreas Mathis, especially, Daniel Heuchel, Robert Münzer, Martin Berger, Christoph Bilko and all the others who took part in the long shifts. I thank all the people of the Excellence Cluster Universe, it was really a nice group to work with. I also thank the people from the E18, with which I worked in close quarters: Bernhard Hohlweger, who introduced me to Garfield and constantly supported me, Daniel Heuchel, Stefan Weber, Julia Bloemer, Sverre Dørheim and Felix Böhmer.

There is no need to thank the people I love, my friends, my family, Claudia. They give meaning to my life, but it's not through my work that I can show it to them.

Bibliography

[1] J. Alme et al. The alice tpc, a large 3-dimensional tracking device with fast readout for ultra-high multiplicity events. *Nucl. Inst. Meth. Phys. Res.*, 622:316, 2010.

[2] F. Sauli. Gem: A new concept for electron amplification in gas detectors. *Nucl. Instr. Meth. A*, 386:531–534, 1997.

[3] J.C. Collins and M.J. Perry. *Phys. Rev. Lett.*, 34:1353, 1975.

[4] J. Ellis. From Little Bangs to the Big Bang. *J. Phys. Conf. Ser.*, 50:8–21, 2006.

[5] S. Borsanyi et al. Is there still any tc mystery in lattice qcd? results with physical masses in the continuum limit iii. *J. H.E. Phys.*, 5, 2010.

[6] L. Cifarelli et al. The Quark-Gluon Plasma, a nearly perfect fluid. *Europhys. News*, 43(2):29–31, 2012.

[7] D. Teaney, J. Lauret, and E.V. Shuryak. A hydrodynamic description of heavy ion collisions at the SPS and RHIC. *nucl-th/0110037*.

[8] M.G. Alford et al. Color superconductivity in dense quark matter. *Rev. Mod. Phys.*, 80:1455–1515, 2008.

[9] C.R. Allton et al. *Nucl. Phys. Proc. Suppl.*, 141:186, 2005.

[10] ALICE collaboration. The ALICE experiment at the CERN LHC. *J. Inst.*, 3(08):S08002, 2008.

[11] H. Fritzsch, M. Gell-Mann, and H. Leutwyler. *Phys. Lett. B*, 47:365, 1973.

[12] L.F. Li T.P. Cheng. Gauge theory of elementary particle physics. *Oxford*, 1984.

[13] S. Borsanyi et al. The QCD equation of state with dynamical quarks. *J. H.E. Phys.*, 77, 2010.

[14] E.V. Shuryak. *Phys. Rep.*, 61:71–158, 1980.

[15] L.C. Mendez. Probing the QGP with ALICE at the LHC. *LNF General Seminar*, 18/04/2013.

[16] R. Snellings. Elliptic flow: a brief review. *New J. Phys.*, 13, 2011.

[17] M.L. Miller et al. Glauber Modeling in High Energy Nuclear Collisions. *Ann. Rev. Nucl. Part. Sci.*, 57:205–243, 2007.

[18] A. Bialas et al. *Nucl. Phys. B*, 111:461, 1976.

[19] ALICE collaboration. Upgrade of the ALICE Experiment Letter Of Intent. 2012.

[20] J. Aichelin, P. Gossiaux, and T. Gousset. Radiative and collisional energy loss of heavy quarks in deconfined matter. *invited talk at the Strange Quark Matter conference in Krakow, 18-24 September 2011.*

[21] S. Lee et al. λ_c enhancement from strongly coupled quark-gluon plasma. *Phys. Rev. Lett.*, 100, 2008.

[22] H. van Hees and R. Rapp. Dilepton radiation at the cern super proton synchrotron. *Nucl. Phys. A*, 806, 2008.

[23] X. Zhao and R. Rapp. Medium modifications and production of charmonia at lhc. *Nucl. Phys. A*, 859:114, 2011.

[24] R. Rapp, J. Wambach, and H. van Hees. The chiral restoration transition of qcd and low mass dileptons. 2009.

[25] The ALICE TPC Collaboration. The alice tpc, a large 3-dimensional tracking device with fast read-out for ultra-high multiplicity events. *Nucl. Instr. Meth. A*, 676, 2010.

[26] W. Blum et al. Particle detection with drift chambers. *Springer*, 2008.

[27] M. Ball et al. Technical design study for the panda time projection chamber. *e-Print: arXiv:1207.0013*, 2012.

[28] F.M. Penning. Uber ionisation durch metastabile atome. *Die Naturwissenschaften*, 1927.

[29] W.W.M. Allison and J.H. Cobb. Relativistic charged particle identification by energy loss. *Ann. Rev. Nucl. Sci.*, 30:253, 1980.

[30] A.H. Walenta et al. *Nucl. Inst. Meth.*, 161:45, 1979.

[31] H.J. Hilke. Time projection chambers. *Rep. Prog. Phys.*, 73:116–201, 2010.

[32] G.D. Alkhazov. Statistics of electron avalances and ultimate resolution of proportional counters. *Nucl. Instr. Meth.*, 89, 1970.

[33] T. Lohse and W. Witzeling. The advanced series on directions in high energy physics vol 9,. *Singapore: World Scientific*, 1992.

[34] S. Ramo. *Proc. IRE*, 27:584, 1939.

[35] H. Raether et al. Electron avalanches and breakdown in gases. *Butterworths London*, 1964.

[36] C.L. Wadhwa. High voltage engineering. *New Age International*, 2007.

[37] ALICE TPC collaboration. Technical design report of the alice tpc upgrade. 2013.

[38] M. Cormier et al. Alice experiment results at the end of lhc run-1. *ORNL Phys. Div. Sem.*, 2013.

[39] D. Mormann et al. Evaluation and reduction of ion back-flow in multi-gem detectors. *Nucl. Instr. Meth. A*, 516, 2004.

[40] P. Abbon et al. The compass experiment at cern. *Nucl. Instr. Meth. A*, 557:455–518, 2007.

[41] B. Ketzer et al. Performance of triple gem tracking detectors in the compass experiment. *Nucl. Instr. Meth. A*, 535:314–318, 2004.

[42] G. Bencivenni et al. A triple gem detector with pad readout for high rate charged particle triggering. *Nucl. Instr. Meth. A*, 488:493–502, 2002.

[43] Z. Fraenkel et al. A hadron blind detector for the phenix experiment at rhic. *Nucl. Instr. Meth. A*, 546:466–480, 2005.

[44] M.G. Bagliesi et al. The totem t2 telescope based on triple-gem chambers. *Nucl. Instr. Meth. A*, 617:134–137, 2010.

[45] D. Abbaneo et al. Characterization of gem detectors for application in the cms muon detection system. 2010.

[46] L. Fabbietti et al. The panda gem-based tpc prototype. *Nucl. Instr. Meth. A*, 628:204–208, 2011.

[47] C. Schwarz (for the PANDA collaboration). The panda experiment at fair. *J. Phys.: Conf. Ser.*, 374, 2012.

[48] F.V. Bohmer et al. Simulation of space-charge effects in an ungated gem-based tpc. *Nucl. Instr. Meth. A*, 719:101–108, 2013.

[49] S. Bachmann et al. Discharge studies and prevention in the gas electron multiplier (gem). *Nucl. Instr. Meth. A*, 479, 2002.

[50] G. Raffone. Cms trapezoidal gem foils structural analysis. *LNF-10/20 (Internal Report)*, 2010.

[51] P.P. Gadow. de/dx studies with π and e tracks of the alice gem iroc prototype. *Bachelor thesis, TU-Muenchen*, 2013.

[52] Maier-Leibnitz-Laboratorium. http://www.bl.physik.uni-muenchen.de.

[53] S. Agostinelli et al. Geant4 - a simulation toolkit. *Nucl. Instr. Meth. A*, 506, 2003.

[54] R. Barth et al. Gsi multi-branch system user manual. 2000.

[55] D. Kaiser. Slow daemon. *HISKP (Bonn).*

[56] P. Fonte V. Peskov. Research on discharges in micropattern and small gap gaseous detectors. 2009.

[57] A. Buzulutskov et al. Gem operation in helium and neon at low temperatures. *Nucl. Instr. Meth. A*, 548, 2005.

[58] A. Bondar et al. Study of ion feedback in multi-gem structures. *Int. Conference on Instr. for Coll. Beam Phys.*, 2002.

[59] M. Kobayashi et al. Coscmic ray tests of a gem-based tpc prototype operated in ar-cf4-isobutane gas mixtures. *Nucl. Instr. Meth. A*, 641, 2011.

[60] F.J. Iguaz et al. Characterization of microbulk detectors in argon- and neon-based mixtures. *J. Instr.*, 7, 2012.

[61] Y. Giomataris et al. Micromegas: a high-granularity position-sensitive gaseous detector for high particle-flux environments. *Nucl. Instr. Meth. A*, 376, 1996.

[62] T.L. van Vuure et al. Limits to proportionality in the double gem detector. *Nucl. Instr. Meth. A*, 477, 2002.

[63] B.M. Ovchinnikov et al. Gas electron multiplier detectors with high reliability and stability. *arXiv:1012.4716*, 2002.

[64] M. Alfonsi et al. Simulation of the dielectric charging-up effect in a gem detector. *Nucl. Instr. Meth. A*, 671, 2012.

[65] J.F. Ziegler. Srim-2003. *Nucl. Instr. Meth. B*, 220, 2004.

[66] M. Kase et al. Fano factor in pure argon. *Nucl. Instr. Meth. A*, 227, 1964.

[67] Magboltz homepage. http://consult.cern.ch/writeup/magboltz/.

[68] S. Procureur et al. A Geant4-based study on the origin of the sparks in a Micromegas detector and estimate of the spark probability with hadron beams. *Nucl. Instr. Meth. A*, 621, 2010.

[69] ANSYS homepage. http://www.ansys.com/.

[70] Garfield++ homepage. http://garfieldpp.web.cern.ch/garfield/.

[71] Wolfram Mathmatica. Finite element method - reference.wolfram.com/applications/structural/finiteelementmethod.html.